RIGOROUS MODEL AND SIMULATIONS OF THE KIRKENDALL EFFECT DIFFUSION IN SUBSTITUTIONAL BINARY ALLOYS

by

Hui-Chia Yu

A dissertation submitted in partial fulfillment
of the requirements for the degree of
Doctor of Philosophy
(Materials Science and Engineering)
in The University of Michigan
2009

Doctoral Committee:

Assistant Professor Katsuyo S. Thornton, Chairperson
Associate Professor Krishnakumar R. Garikipati
Associate Professor Joanna Mirecki-Millunchick
Assistant Professor Anton Van der Ven
Associate Professor Xiaofan Li, Illinois Institute of Technology

To My Family

ACKNOWLEDGEMENTS

I am sincerely grateful to my thesis advisor Prof. Katsuyo Thornton, who has given me great support and guidance through my whole thesis work. Without her support, I would not have completed my doctoral degree. During these years, I have learned much from working with her, especially the importance of striving for high standards in work.

I am deeply indebted to Prof. Anton Van der Ven, who has greatly inspired me with his strong and solid knowledge of diffusion. I thank Prof. Xiaofan Li for his very helpful suggestion to use an implicit scheme and other mathematical techniques. I also thank my other committee members Prof. Krishna Garikipati and Prof. Joanna Millunchick for reading this thesis and giving many useful comments on my work.

This thesis work was mainly supported by NSF under Grant No. 0511232. This financial support has been appreciated.

During these years, I have met many wonderful people here. I would like to thank my labmates: Dr. Dong-Hee Yeon, Chloe Funkhouser, Victor Chan, Hsun-Yi Chen, Nirand Pisutha-Arnond and Chal-Lan Park. To all friends I have made in Ann Arbor: thank you! I will always have fond memories.

I am very thankful for the unconditional support of my family. My parents, my wife Shin-Yi, and my daughter Amber have given me the warmth and encouragement when I faced the difficult times. Without them, I would not have been able to finish this journey.

TABLE OF CONTENTS

LIST OF FIGURES

Figure

LIST OF TABLES

Table

CHAPTER I

INTRODUCTION

1.1 General Background of the Kirkendall Effect

The Kirkendall effect refers to the inert marker motion caused by lattice shifts during a diffusion process and was first discovered by E. O. Kirkendall [1]. In his experiments, the embedded molybdenum wires, which are not involved in diffusion of zinc and copper, shift from their original positions in a brass-copper diffusion couple. According to his biography [2], Kirkendall strongly suspected that the shift was stemming from lattice reconstruction/destruction and was a form of material flow, which was in conflict with the existing theory of solid diffusion. In order to successfully complete his Ph.D., he proceeded to explain that the volume change caused by compositional evolution during the diffusion process was the origin of the shift [2]. After receiving his Ph.D. from the University of Michigan, Kirkendall became a faculty member in Wayne State University. There, he and his graduate student, A. D. Smigelskas, performed similar experiments with higher precision to confirm that the marker motion must result from lattice generation and destruction caused by unequal diffusion fluxes of zinc and copper in the diffusion couples [3, 4].

The concept of unbalanced diffusion was not immediately accepted when Kirkendall submitted his experimental results and theory for publication. The work [4] was finally published after an initial rejection and a six-month argument [2, 5], accompanied by reviewers opposing comments. Three years later, the validity of the

unbalanced diffusion and the Kirkendall effect were widely approved, along with the theoretical works of the vacancy-mediated mechanism [6] and the Darken's analysis [7] in a diffusion conference [8, 9]. Subsequently, the Kirkendall effect led to the revolutionary concept of the vacancy-mediated mechanism in solid diffusion and opened a new field in diffusion science referred to as the interdiffusion [10].

Diffusion in crystalline solids occurs through atomic migration along the lattice networks driven by chemical potential gradients. When the diffusing species have smaller atomic radii than the atoms forming the lattice structure, their diffusion tends to occur through the interstitial sites. On the other hand, diffusing species with similar atomic radii to those of the lattice atoms tend to migrate through the lattice sites in a process referred to as the substitutional diffusion. When one species has a larger successful atomic hop frequency (or rate) to the neighboring vacant lattice sites, the overall diffusion flux of this species will be larger than that of the counter-diffusing species. As a result, a net vacancy flux arises from the slow-diffuser side to the fast-diffuser side as vacancies exchange positions with the atomic species. (In diffusion science, the atomic species with a larger exchange rate of vacancies is referred to as the fast diffuser, while the other species is termed the slow diffuser.) During this process, vacancies are injected to (eliminated from) the solids at vacancy sources (sinks) to maintain the vacancy mole fraction at the thermodynamic equilibrium value. Consequently, lattice planes are created (destroyed), and the lattice shifts with respect to the source (sink) locations. This results in two phenomena: marker migration and pore formation. The former is a result of the lattice motion in the laboratory frame caused by vacancy injection and elimination at internal vacancy sources and sinks. The later involves surface evolution stemming from the vacancy injection and elimination at external vacancy sources and sinks at the void surfaces. This is also known as the Frenkel effect, which does not involve internal lattice shift. In this thesis, both phenomena are generally referred to as "the Kirkendall effect".

(We use the term, the Kirkendall effect, in a broad sense to include all phenomena involving nonreciprocal diffusion.) The Kirkendall effect has been widely reported in a variety of diffusion couples, such as copper-zinc [1, 3, 4], copper-tin [11, 12], gold-platinum [13, 14, 15], gold-silver [16, 17], and many other types of diffusion couples [9, 18, 19, 20, 21, 22, 23, 24, 25], as well as in many practical engineering components, such as solder joints [26, 27, 28], wire bonding [29, 30, 31], composite materials [32, 33], thin-film devices [34, 35, 36, 37], and heterogeneous alloys [38, 39, 40]. They are observed in the forms of pore formation [9, 41, 42, 43, 44, 32], deformation [45, 46] near interfaces [47, 48], internal stresses [49, 50], and material segregation [51, 52, 53, 54, 55]. Figure 1.1 shows examples of various phenomena related to the Kirkendall effect.

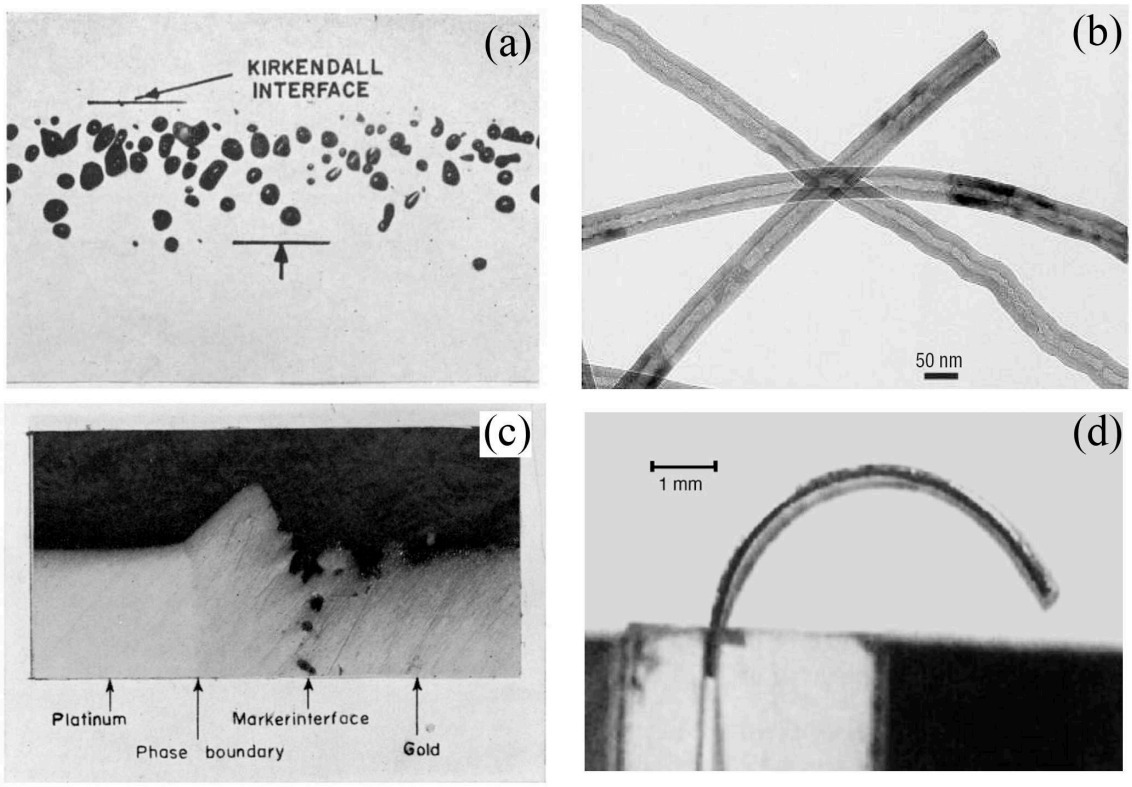

Figure 1.1: (a) Kirkendall voids form near diffusion interface in a Cu-Ni diffusion couple, from Ref. [42]. (b) Monocrystalline spinel nanotube fabricated by Kirkendall void formation, from Ref. [61]. (c) Surface deformation near diffusion interface in a Au-Pt diffusion couple, from Ref. [14]. (d) Kirkendall-effect-induced bending in a Ti-Zr sample, from Ref. [50].

Darken's analysis [7] was the first and most widely accepted model that explains the lattice shift caused by vacancy generation and annihilation due to unequal mobilities of the atomic diffusing species. When atomic species with unequal mobility diffuse, nonzero vacancy flux arises. When the vacancy flux is not constant, it can give rise to deviations in vacancy concentration. Darken's model assumes that crystalline solids contain a sufficient amount of vacancy sources and sinks such that vacancies can be generated or eliminated everywhere in a crystal to equilibrate vacancy mole fraction to its thermal equilibrium value. Under this assumption, all excess vacancies are consumed by internal vacancy sinks immediately after they are generated. As a result, vacancy concentration remains at equilibrium and is uniform throughout a solid.

Darken's theory explains the lattice motion that was observed by Kirkendall, and it was instrumental in the acceptance of Kirkendalls work on vacancy-mediated diffusion in substitutional alloys. However, experimental observations suggest that not all vacancies are annihilated by the internal vacancy sinks. In fact, without vacancy supersaturation, no void would form, contradicting experimental observations of void formation. Vacancy supersaturation does occur in mole fractions as high as $1 \sim 2$ % [44], and those vacancies coalesce to form voids during interdiffusion. The void surfaces then consume vacancies during the void growth stage. This phenomenon is called the Frenkel effect [10] and provides evidence that Darken's approximation may not always be applicable [56, 57, 58].

The Kirkendall porosity can cause engineering problems such as weakening in mechanical properties at the wire bonding on integrated circuit boards [29, 30, 31] or at the bond coat [59, 60] between the thermal barrier coating and the base metal in turbine blades. Thus, the Kirkendall porosity has been long considered as an undesirable phenomenon. Recently, there has been renewed interest in utilizing the Kirkendall effect to fabricate micro/nano hollow objects, such as hollow rods [61, 62]

and hollow particles [63, 64, 65, 66]. These hollow objects possess potential for applications such as drug delivery [67], wave guides [68] and light-emitting devices [69]. A core-shell-type diffusion couple is constructed by coating a layer of a slow diffuser on a fast-diffuser core. As diffusion occurs, the fast diffuser atoms diffuse to the outer region by exchanging their lattice positions with vacancies. Voids form from the supersaturated vacancies and then grow within the diffusion couple, resulting in a hollow object. (See Fig. 1.1(b) for an example of nanotubes fabricated by Kirkendall void formation.) This process cannot be described by Darken's model of the Kirkendall effect. Some theoretical works have been performed to model the hollow object formation by excluding the internal vacancy sources and sinks in the diffusion couples [70, 71] so that vacancy concentration can vary from the equilibrium value. These models assume a quasi-steady-state diffusion of vacancies and atomic diffusers in the compound layer between fast-diffuser-rich and slow-diffuser-rich regions, and can only be used to predict the thickness of the compound layer. However, Kirkendall-effect-induced hollow particle formation was also reported in micro-scale solid-solution alloy particles decades ago [72]. This indicates that the Frenkel effect itself (not the solid-state reaction in the compound layer) should be the key element of void growth within such crystalline solid objects.

The Kirkendall effect was also observed along free surfaces [73, 74, 75] and grain boundaries [36, 76, 77] that can simultaneously serve as fast paths for diffusion and as primary vacancy sources and sinks due to the loose lattice structure. This enhanced interdiffusion results not only in inert marker motion but also in surface evolution and void growth along grain boundaries. Moreover, the Kirkendall effect has recently been proposed to be responsible for the whisker growth phenomenon in lead-free solder. The whisker growth process is thought to involve two factors [78]. One is the compressive stress built in the film layer. The other is the grain boundary diffusion along the columnar grain surfaces. A whisker grain grows in order to relieve

compressive stresses in the film layer. This compressive stress can originate from several possible sources, such as oxide formation and unequal thermal expansion rates between the film and the substrate. Recently, the Kirkendall effect is suggested to be one of the stress sources [78]. While stress relaxation provides the energetics for whisker growth, grain boundary diffusion provides the kinetic path that enables creep flow along the columnar grain boundaries. However, theoretical investigations on the subject of Kirkendall-effect-induced stress and Kirkendall-effect-enhanced grain boundary diffusion have only recently begun (see, e.g., Refs. [79, 80, 81, 82]).

1.2 Diffuse Interface Method

To investigate the phenomena resulting from the Kirkendall effect, a numerical method capable of tracking shape change and void growth is necessary. Although the conventional sharp interface model and the diffuse interface model are both able to solve moving interface problems, these pose computational challenges when the geometry is complex. Therefore, we developed a diffuse interface method for numerical simulations of the Kirkendall effect in higher dimensions (two or three dimensions). For one-dimensional problems, we employ a sharp interface description, which is adequate and straightforward to implement with simple geometries and is more computationally efficient.

A diffuse interface model can be traced back to as early as van der Waal's calculation of capillary energy across an interface with spatially varying density [83]. Half a century later, Cahn and Hilliard developed a free energy functional to describe the total energy of a system containing two phases by using a single order parameter [84]. This order parameter has different values in each phase but is continuously transitioning from the value in one phase to that in the other phase. The free energy of the bulk in a phase is calculated by assuming a uniformly distributed order parameter in that phase. On the other hand, the gradient of the order parameter across

the two phases, as well as the energy barrier between the two phases, gives rise to the interfacial energy. The morphology of the phase boundaries is therefore naturally tracked according to the order parameter redistribution during free energy dissipation processes. This method is referred to as the phase field method. The evolution of the system is described by the Cahn-Hilliard equation for conserved order parameters such as density. Analogously, for non-conserved order parameters such as magnetism or the structural order parameter, Ginzburg et al. [85] and Allen et al. [86] developed a model, which is described by the so-called time-dependent Ginzburg-Landau equation or Allen-Cahn equation. In practice, the equations mentioned above can be employed for conserved or non-conserved order parameters alone or for coupling these two types of order parameters to form a family of phase field models.

The most significant advantage of a phase field model is that an explicit tracking of the interface is unnecessary. As order parameter profiles evolve, the system determines the phase distribution and the interfaces automatically. The same equation (or set of equations) is solved in the entire computational domain containing different phases represented by the order parameter(s). Conversely, a conventional sharp interface model requires solving differential equations within each domain of different phases and matching the boundary conditions at the interfaces. In a free-boundary problem where interfaces can migrate, a re-meshing process is required in a conventional sharp interface model and can be computationally intensive. Furthermore, topological changes such as coalescence and breakup of domains are difficult to handle in such methods. Phase field models are also very flexible in modeling a wide variety of physical systems by allowing the coupling of multiple physical fields that enter into the energy expressions. For example, the Allen-Cahn equation can be coupled with a temperature field to simulate dendritic growth during solidification process [87, 88, 89], and the Cahn-Hilliard equation can be coupled with fluid flow (Navier-Stokes equation) to model two-phase flow dynamics [90, 91]. These

advantages make phase field models well suited for moving boundary problems in computational materials science.

Despite these advantages, phase field models are not widely employed in simulations that involve *explicit* boundary conditions along interfaces. There are only a few well-recognized cases where phase field models were used in simulations with explicit boundary conditions at interfaces. For example, in solidification problems, equilibrium conditions such as equilibrium temperature or concentration [92, 93] are imposed at the solid-liquid interfaces where the order parameter field and the temperature field are coupled via a latent heat term. Except for this type of phase field model, directly applying boundary conditions at interfaces is rarely used. Despite the fact that Cahn [94] had suggested a technique to apply boundary conditions at interfaces by including an extra energy term in the energy functional three decades ago, practical works adopting such a concept have only recently been published, e.g., by Warren et al. [95, 96], who demonstrated the ability of a phase field model to allow explicit boundary conditions at interfaces. In addition to Warren's work, Bueno-Orovio [97, 98] proposed a different technique to impose no-flux boundary conditions at interfaces in a general static diffuse interface model, i.e., numerically assigning internal boundary conditions within a computational domain on boundaries defined by a static, phase-field-like function. We further advance this method to include more general boundary conditions, such as Neumann, Dirichlet, and mixed boundary conditions. By allowing the coupling between the order parameter and the concentration field, this method is applied to simulate moving interface problems induced by the Kirkendall effect, such as surface shape change, void growth, and deformation during diffusion.

1.3 Research Objectives

There are many observations of the phenomena stemming from the Kirkendall effect, including formations of voids, deformation, and internal stress. These experimental

observations and measurements provided firsthand evidence and understanding of interdiffusion. However, it is difficult to predict diffusion phenomena involving more complicated geometries based on experimental observations involving simpler geometries (for example, thin films) alone. Therefore, a reliable model and a numerical method will be important tools for verification of theories and quantitative predictions. In this dissertation, we propose a new, more rigorous model of the Kirkendall effect. We consider explicit and localized sources and sinks of vacancies, where vacancies can be supplied or eliminated. We assume that free surfaces and grain boundaries are more efficient vacancy sources and sinks, and the role of dislocations as a vacancy source or sink in the bulk of a grain is ignored. This assumption is different from the current standard model based on Darken's analysis, where vacancy sources and sinks are assumed to exist everywhere within a solid. As with Darken's model, we assume that sources and sinks act ideally; i.e., any supersaturation or undersaturation is immediately accommodated at these locations.

The overarching objective of this research is to enhance the understanding of interdiffusion by developing and applying a rigorous formulation of substitutional diffusion that would properly describe systems without continuous and uniform vacancy sources. This would involve two main tasks. One is to formulate the theory and mathematical models, and the other is to develop flexible numerical methods that allow simulation of physically realistic systems. Crystalline solids contain explicit vacancy sources and sinks, such as surfaces, grain boundaries, and dislocations. Diffusion in the lattice regions other than vacancy sources and sinks should occur through regular atomic jumps to neighboring vacant sites. The diffusion coefficients of a crystalline solid with a well-defined lattice structure have been theoretically calculated considering atomic hops through the lattice structure in the past decades. For example, analytical derivations were obtained for ideally mixing random alloys [99, 100], and kinetic Monte Carlo simulations were performed for non-ideal alloys [101]. To apply

these diffusion coefficients to predict diffusion behavior, a model of concentration evolutions at the continuous scale is required. However, these diffusion coefficients are for diffusion in lattice structures in the absence of defects serving as vacancy sources and thus are inappropriate to be employed within the standard Darken's model, which cannot distinguish vacancy sources from regular lattice regions. In addition, since Darken's equations implicitly include vacancy injection and elimination, the diffusion coefficients calculated by applying Darken's equations to experimental measurements of concentration profiles could be incorrect [102]. Therefore, our model, where the diffusion process and vacancy injection are treated separately, is expected to provide a link between the theoretically predicted diffusion coefficients and the macroscopic diffusion phenomena. This model will be used as a tool to identify important physics that are not revealed using the traditional model and also to provide proper comparisons between theoretical predictions and experimental measurements at the macroscopic scale.

To implement the simulations for our model in higher dimensions (two or three dimensions), we developed a new numerical approach that employs a diffuse interface description that does not require explicit tracking of boundaries between two domains. This method is promising as an efficient solver for general partial differential equations with the flexibility of applying boundary conditions with a complicated geometry within a computational domain. We expect that the simulations of the Kirkendall-effect-induced surface evolution, void growth, and deformation will provide an excellent opportunity for examining and verifying the capabilities of this new method.

1.4 Thesis Outline

This dissertation contains seven chapters: (1) Introduction, (2) Diffusion in Binary Substitutional Crystalline Solids, (3) One-Dimensional Sharp Interface Simulations,

(4) Kirkendall-Effect-Induced Grain Boundary Diffusion, (5) Diffuse Interface Approach for Conventional Modeling, (6) Diffuse Interface Approach for Rigorous Modeling, and (7) Summary, Conclusions, and Future Work.

A brief historical and background review is given in Chapter One, followed by the research objectives and thesis outline.

In Chapter Two, the flux and diffusion equations governing interdiffusion in binary alloys are derived from the phenomenological laws for substitutional alloys. The Darken's equations are derived by approximating the vacancy concentration to be uniform and at the thermodynamic equilibrium value, while the rigorous model is derived without such approximation.

Chapter Three consists of the simulation results of the rigorous model in one-dimensional sharp interface descriptions in planar and cylindrical symmetries. We observe the surface and grain boundary motion due to vacancy injection and elimination at surfaces and grain boundaries, and the results reveal two competing factors (the Kirkendall effect and the Gibbs-Thomson effect) in void growth dynamics. The results also show that the Darken's model is one limiting case in the rigorous model, and demonstrate the importance of a vacancy source-sink pair in diffusion involving the Kirkendall effect.

Chapter Four demonstrates a new mechanism of enhanced grain boundary diffusion based on the rigorous model results. Two diffusion modes, unbalanced diffusion mode and intermixing diffusion mode, are identified during interdiffusion. The Darken's model reflects only an unbalanced diffusion mode and excludes the intermixing diffusion mode.

In Chapter Five, a smooth boundary method for the standard Darken's model with a no-flux boundary condition on the solid-air interface is developed. It provides an efficient numerical method for simulating the diffusion-induced deformation phenomena.

Chapter Six contains simulations of our rigorous model in two dimensions, where equilibrium vacancy concentration remains only along free surfaces and grain boundaries. Preliminary results are presented.

Chapter Seven summarizes the work presented in this thesis and describes the direction of future work.

CHAPTER II

DIFFUSION IN BINARY SUBSTITUTIONAL CRYSTALLINE SOLIDS

2.1 General Flux Expression

Our starting point is a rigorous description of vacancy-mediated substitutional diffusion in a binary crystalline solid. While two atomic species form such an alloy, three species in fact exist in an A-B binary system: atomic species A and B, and vacancies V. Throughout this thesis, we take A as the slow diffuser and B as the fast diffuser. Irreversible thermodynamics stipulates that the driving forces for diffusion are the existence of gradients in chemical potentials [103]:

$$J_A = -L_{AA}\nabla\mu_A - L_{AB}\nabla\mu_B - L_{AV}\nabla\mu_V, \tag{2.1a}$$

$$J_B = -L_{BA}\nabla\mu_A - L_{BB}\nabla\mu_B - L_{BV}\nabla\mu_V, \tag{2.1b}$$

$$J_V = -L_{VA}\nabla\mu_A - L_{VB}\nabla\mu_B - L_{VV}\nabla\mu_V, \tag{2.1c}$$

where J_i is the flux vector of the i-th species, whose magnitude is given by the number of atoms or vacancies crossing a unit area per unit time in the direction of the flow, L_{ij} is the kinetic transport coefficient, and μ_i is the chemical potential. According to Onsager's reciprocity theorem [104, 105], the kinetic transport coefficients form a symmetric matrix:

$$L_{AB} = L_{BA} \quad \text{and} \quad L_{AV} = L_{VA} \quad \text{and} \quad L_{VB} = L_{BV}. \tag{2.2}$$

In a perfect lattice region (containing only dilute vacant lattice sites, and devoid of dislocations, grain boundaries, and surfaces), the lattice sites are conserved and, therefore, the net flux must be zero:

$$J_A + J_B + J_V = 0. \tag{2.3}$$

This imposes a constraint,

$$L_{AV} = -\left(L_{AA} + L_{AB}\right) \quad \text{and} \quad L_{BV} = -\left(L_{AB} + L_{BB}\right), \tag{2.4}$$

such that two of the three flux equations are sufficient to completely describe the system:

$$J_A = -L_{AA}\nabla\left(\mu_A - \mu_V\right) - L_{AB}\nabla\left(\mu_B - \mu_V\right) = -L_{AA}\nabla\tilde{\mu}_A - L_{AB}\nabla\tilde{\mu}_B, \tag{2.5a}$$

$$J_B = -L_{AB}\nabla\left(\mu_A - \mu_V\right) - L_{BB}\nabla\left(\mu_B - \mu_V\right) = -L_{AB}\nabla\tilde{\mu}_A - L_{BB}\nabla\tilde{\mu}_B, \tag{2.5b}$$

where $\tilde{\mu}_i = \mu_i - \mu_V$ is the chemical potential measured relative to that of vacancies (i= A or B). As indicated in Ref. [106], a driving force of this form reflects the fact that substitutional diffusion of an atom within a perfect lattice structure occurs via positional exchange with a neighboring vacant site. This driving force can be expressed as

$$\tilde{\mu}_i = \frac{\partial G}{\partial X_i}, \tag{2.6}$$

where G is the Gibbs free energy per crystal site of the alloy and X_i is the mole fraction of the *i-th* species, with $X_A + X_B + X_V = 1$.

While a linear relationship between the fluxes and their driving forces, Eq. (2.5), can be employed to describe concentration evolution, it is more convenient to relate a flux in terms of experimentally measurable quantities, i.e., concentrations. Invoking

the chain rule of differentiation, Eq. (2.5) can be rewritten as

$$\begin{aligned} J_A =& - L_{AA}\left(\frac{\partial\tilde{\mu}_A}{\partial C_A}\nabla C_A + \frac{\partial\tilde{\mu}_A}{\partial C_B}\nabla C_B\right) - L_{AB}\left(\frac{\partial\tilde{\mu}_B}{\partial C_A}\nabla C_A + \frac{\partial\tilde{\mu}_B}{\partial C_B}\nabla C_B\right) \\ =& - \left(L_{AA}\frac{\partial\tilde{\mu}_A}{\partial C_A} + L_{AB}\frac{\partial\tilde{\mu}_B}{\partial C_A}\right)\nabla C_A - \left(L_{AA}\frac{\partial\tilde{\mu}_A}{\partial C_B} + L_{AB}\frac{\partial\tilde{\mu}_B}{\partial C_B}\right)\nabla C_B, \end{aligned} \tag{2.7a}$$

$$\begin{aligned} J_B =& - L_{AB}\left(\frac{\partial\tilde{\mu}_A}{\partial C_A}\nabla C_A + \frac{\partial\tilde{\mu}_A}{\partial C_B}\nabla C_B\right) - L_{BB}\left(\frac{\partial\tilde{\mu}_B}{\partial C_A}\nabla C_A + \frac{\partial\tilde{\mu}_B}{\partial C_B}\nabla C_B\right) \\ =& - \left(L_{AB}\frac{\partial\tilde{\mu}_A}{\partial C_A} + L_{BB}\frac{\partial\tilde{\mu}_B}{\partial C_A}\right)\nabla C_A - \left(L_{AB}\frac{\partial\tilde{\mu}_A}{\partial C_B} + L_{BB}\frac{\partial\tilde{\mu}_B}{\partial C_B}\right)\nabla C_B. \end{aligned} \tag{2.7b}$$

By absorbing the thermodynamic factors and the kinetic coefficients in the diffusion coefficients, one obtains the following:

$$J_A = -D_{AA}\nabla C_A - D_{AB}\nabla C_B, \tag{2.8a}$$

$$J_B = -D_{BA}\nabla C_A - D_{BB}\nabla C_B, \tag{2.8b}$$

where C_i is the concentration of the *i-th* species and is defined as the number of atoms per unit volume. These are known as the generalized Fick's equations for substitutional diffusion in a perfect crystal. Since each lattice site is occupied by an atom or a vacancy, the mole fraction (or lattice site fraction) is related to the concentration by $C_i = \rho X_i$, where ρ is the lattice site density, having the same units as concentration. In a perfect lattice, the number of lattice sites is conserved: $C_A + C_B + C_V = \rho$. This provides a constraint on the concentration gradients, such that

$$\nabla C_A + \nabla C_B + \nabla C_V = 0. \tag{2.9}$$

Comparing Eqs. (2.7) and (2.8), the diffusion coefficient D_{ij} is related to the kinetic transport coefficients L_{ij} according to

$$\begin{pmatrix} D_{AA} & D_{AB} \\ D_{BA} & D_{BB} \end{pmatrix} = \begin{pmatrix} L_{AA} & L_{AB} \\ L_{BA} & L_{BB} \end{pmatrix} \begin{pmatrix} \partial\tilde{\mu}_A/\partial C_A & \partial\tilde{\mu}_A/\partial C_B \\ \partial\tilde{\mu}_B/\partial C_A & \partial\tilde{\mu}_B/\partial C_B \end{pmatrix}. \tag{2.10}$$

A calculation of the diffusion coefficients requires not only the kinetic transport co-

efficients, but also the partial derivatives of the chemical potentials − the so-called thermodynamic factors.

When considering diffusion in a binary alloy, evolution of the concentration of A and B is important. Practically, however, it is more convenient to describe the system with the concentrations of vacancies and the fast diffuser. (Numerically, it is essential to track the vacancy concentration, which is orders of magnitude smaller than the concentrations of the atomic species.) Using Eqs. (2.3) and (2.9), one can reformulate Eq. (2.8) to obtain:

$$J_V = -D_{VV}\nabla C_V - D_{VB}\nabla C_B, \tag{2.11a}$$

$$J_B = -D_{BV}\nabla C_V - D^V_{BB}\nabla C_B, \tag{2.11b}$$

where the diffusion coefficients are given by $D_{VV} = D_{AA}+D_{BA}$, $D_{VB} = D_{AA}-D_{AB}+D_{BA}-D_{BB}$, $D_{BV} = -D_{BA}$ and $D^V_{BB} = D_{BB} - D_{BA}$.

2.2 Darken's Equations

Darken [7] proposed the first analysis relating marker motion to the difference between the two atomic fluxes in an A-B binary alloy system. Darken postulated that each atomic species diffuses independently of the other. Thus, each atomic diffuser has its own diffusion coefficient, and diffusion of each atomic species is driven only by the gradient of its own concentration. In this case, a binary alloy is assumed to consist of only two diffusing species, but the fluxes can differ from each other. In this analysis, two reference frames of the coordinate are introduced in the binary crystalline solid. One reference frame is fixed with the observer outside the crystal, and is referred to as the laboratory frame. The other is fixed with the lattice planes, and is referred to as the lattice frame. The model predicts that the lattice frame moves with a velocity, v, during diffusion. Therefore, when the lattice frame is labeled with fiducial markers in a diffusion couple, the motion of the lattice frame can be observed. In this analysis,

neither the vacancy-mediated diffusion mechanism, nor the origin of marker motion and its relation to vacancy generation and elimination were explicitly considered.

In a one-dimensional Cartesian coordinate system, diffusion fluxes in the lattice frame inside an A-B binary alloy are governed by Fick's First Law as:

$$J_A = -D_A \frac{\partial C_A}{\partial x}, \tag{2.12a}$$

$$J_B = -D_B \frac{\partial C_B}{\partial x}, \tag{2.12b}$$

where D_i is the diffusion coefficient, which can be different for each species. Since each of the atomic species possesses its own independent diffusion coefficient, these coefficients are commonly referred to as the intrinsic diffusion coefficients or self-diffusion coefficients. From the view of an observer fixed in the laboratory frame, the diffusion fluxes are advected by the moving lattice frame. Thus, the fluxes are given by

$$\tilde{J}_A = J_A + vC_A = -D_A \frac{\partial C_A}{\partial x} + vC_A, \tag{2.13a}$$

$$\tilde{J}_B = J_B + vC_B = -D_B \frac{\partial C_B}{\partial x} + vC_B. \tag{2.13b}$$

The rates of concentration change of the diffusers are given by the divergences of the fluxes according to Fick's Second Law:

$$\frac{\partial C_A}{\partial t} = -\frac{\partial}{\partial x}\tilde{J}_A = \frac{\partial}{\partial x}\left(D_A \frac{\partial C_A}{\partial x} - vC_A\right), \tag{2.14a}$$

$$\frac{\partial C_B}{\partial t} = -\frac{\partial}{\partial x}\tilde{J}_B = \frac{\partial}{\partial x}\left(D_B \frac{\partial C_B}{\partial x} - vC_B\right). \tag{2.14b}$$

Here, there is no distinction between spatial derivatives in the two reference frames because the local region in the lattice frame is assumed to be a rigid translation of the laboratory frame, traveling at a velocity, v. The summation of Eq. (2.14a) and Eq. (2.14b) gives the rate of change of the sum of the atomic concentrations:

$$\frac{\partial}{\partial t}\left(C_A + C_B\right) = \frac{\partial}{\partial x}\left[D_A \frac{\partial C_A}{\partial x} + D_B \frac{\partial C_B}{\partial x} - v\left(C_A + C_B\right)\right]. \tag{2.15}$$

In Darken's analysis, all lattice sites are assumed to be occupied by either A or B atoms: $C_A + C_B = \rho$. If the lattice density is assumed to remain constant, one obtains the following relation:

$$\frac{\partial C_A}{\partial t} + \frac{\partial C_B}{\partial t} = 0 \quad \text{and} \quad \frac{\partial C_A}{\partial x} + \frac{\partial C_B}{\partial x} = 0. \tag{2.16}$$

Substituting Eq. (2.16) into (2.15) gives:

$$\frac{\partial}{\partial x}\left[(D_A - D_B)\frac{\partial C_A}{\partial x} - v\rho\right] = 0. \tag{2.17}$$

Integrating this expression from the left end of the diffusion couple to an arbitrary point, x, in the diffusion zone, one obtains

$$(D_A - D_B)\frac{\partial C_A}{\partial x}\bigg|_{-\infty}^{x} - v\rho\bigg|_{-\infty}^{x} = I, \tag{2.18}$$

where I is an integration constant. Since the concentration is uniform outside the diffusion zone, and diffusion only takes place within the diffusion zone,

$$\frac{\partial C_A}{\partial x}\bigg|_{-\infty} = 0 \quad \text{and} \quad v\bigg|_{-\infty} = 0. \tag{2.19}$$

This relation provides the boundary conditions for Eq. (2.18), which subsequently yields $I = 0$. Equation (2.18) therefore provides the lattice velocity at an arbitrary point x as:

$$v(x) = \frac{1}{\rho}(D_A - D_B)\frac{\partial C_A(x)}{\partial x} = \frac{1}{\rho}(D_B - D_A)\frac{\partial C_B(x)}{\partial x} = -\frac{1}{\rho}(J_A + J_B). \tag{2.20}$$

Eq. (2.20) indicates that the lattice density of a strictly defined binary alloy remains constant from an observer's view only if the local lattice planes in the diffusion zone shift at a velocity that is proportional to the difference between the two intrinsic diffusion coefficients, or, more precisely, to the difference between the two diffusion fluxes. This relation is commonly known as Darken's First equation.

With this expression of lattice velocity, the rates of concentration evolution within

the diffusion zone from an observer's view, Eq. (2.14), are then reformulated as

$$\frac{\partial C_A}{\partial t} = \frac{\partial}{\partial x}\left[\left(X_B D_A + X_A D_B\right)\frac{\partial C_A}{\partial x}\right] = \frac{\partial}{\partial x}\left(\tilde{D}\frac{\partial C_A}{\partial x}\right), \tag{2.21a}$$

$$\frac{\partial C_B}{\partial t} = \frac{\partial}{\partial x}\left[\left(X_A D_B + X_B D_A\right)\frac{\partial C_B}{\partial x}\right] = \frac{\partial}{\partial x}\left(\tilde{D}\frac{\partial C_B}{\partial x}\right). \tag{2.21b}$$

Each of these expressions for the rate of concentration evolution now depends only on its concentration gradient and a diffusion coefficient. These expressions have a form identical to that of Fick's Second Law. The coefficient $\tilde{D}$ is a combination of the two intrinsic diffusion coefficients. This factor reflects the fact that, from the observer's standpoint, the process of concentration homogenization depends on diffusion of both species. Therefore, $\tilde{D}$ is referred to as the interdiffusion coefficient, and the relation $\tilde{D} = X_A D_B + X_B D_A$ is known as Darken's second equation. Equation (2.21) can be solved to predict the evolution of the concentration profiles.

The result of Darken's analysis described above has been widely employed to experimentally determine intrinsic diffusion coefficients. This analysis is considered to be the standard model describing marker motion resulting from interdiffusion in systems with two components having unequal mobilities. By measuring the concentration variation along the diffusion axis as a function of time and by comparing it to the prediction based on Eq.(2.21), $\tilde{D}$ can be extracted. Marker velocities can also be measured by determining the marker position as a function of time. Therefore, the difference between the two intrinsic diffusion coefficients can be obtained according to Eq. (2.20). By using the measured interdiffusion coefficient and the difference between intrinsic diffusion coefficients, the intrinsic diffusion coefficients of the binary-alloy components can be determined.

While Darken's analysis starts from Fick's First Law for fluxes, Eq. (2.12), these fluxes must be consistent with the generalized flux expressions, Eq. (2.5). If there are no vacancies and no interstitial diffusion is possible, diffusion can only take place via direct exchange of atoms located next to each other or by a ring-rotation mechanism

that involves simultaneous motion of more than two atoms. Thus, the total flux of the diffusers must be zero relative to the lattice planes: $J_A + J_B = 0$. However, according to Darken's analysis of this case, there would be no lattice shift, as pointed out by Bardeen [107].

To resolve this apparent conflict, Bardeen performed the following analysis [107]. In a crystalline solid containing A atoms, B atoms, and vacancies, the Gibbs-Duhem relation is given by $X_A d\mu_A + X_B d\mu_B + X_V d\mu_V = 0$. This relation can be reduced to $X_A d\mu_A + X_B d\mu_B = 0$ if one makes the additional assumption that $d\mu_V = 0$. Thermodynamically, this means that adding or removing vacancies to or from lattice sites does not change the chemical potential for vacancies, i.e., μ_V is constant. This condition could be achieved by assuming there is a sufficient concentration of very efficient vacancy sources and sinks that maintain the vacancy concentration at its equilibrium value instantaneously. In this case, terms proportional to the $\nabla\mu_V$ can be dropped, and one constraint relating $\nabla\mu_A$ to $\nabla\mu_B$ by the mole fractions emerges. Equation (2.5) can then be simplified to

$$J_A = \left(\frac{L_{AA}}{X_A} - \frac{L_{AB}}{X_B}\right) X_A \nabla\mu_A = -D_A \nabla C_A, \tag{2.22a}$$

$$J_B = \left(\frac{L_{BB}}{X_B} - \frac{L_{AB}}{X_A}\right) X_B \nabla\mu_B = -D_B \nabla C_B, \tag{2.22b}$$

where the intrinsic diffusion coefficients D_i can now be linked to the kinetic transport coefficients and thermodynamic factors by

$$D_A = \left(\frac{L_{AA}}{X_A} - \frac{L_{AB}}{X_B}\right) X_A \frac{\partial\mu_A}{\partial C_A}, \tag{2.23a}$$

$$D_B = \left(\frac{L_{BB}}{X_B} - \frac{L_{AB}}{X_A}\right) X_B \frac{\partial\mu_B}{\partial C_B}. \tag{2.23b}$$

These results link the fundamental flux expressions, Eq. (2.5), to the phenomenological Ficks First Law, Eq. (2.12). These results also reveal that, in multicomponent systems, the cross terms of the kinetic coefficients play a significant role in the deter-

mination of the intrinsic diffusivities. Furthermore, these relations show that Darken's equations only hold true when the vacancy concentration remains at its equilibrium value throughout a crystal via the action of vacancy sources and sinks.

2.3 Rigorous Model

When separations between vacancy sources and sinks are larger than a typical vacancy migration distance over the diffusion time scale, vacancies can no longer be assumed to generate or vanish throughout the crystalline solid. Instead, vacancies are injected or eliminated only at discrete sources and sinks. In this case, the assumptions that the vacancy chemical potential is constant and that the vacancy concentration is at equilibrium are no longer valid. The vacancy concentration can deviate from its equilibrium value according to the governing diffusion mechanisms. In this case, the models must explicitly consider the kinetic process of vacancy diffusion in the lattice network.

In the present treatment, we will assume that vacancy sources and sinks are ideal. An ideal vacancy source or sink will instantaneously accommodate any supersaturation of vacancies in its immediate vicinity so that the local vacancy concentration always equals the equilibrium vacancy concentration. Regions where the vacancy mole fraction is specified can act as sources, where vacancies are created, or as sinks (negative sources), where vacancies are annihilated. Vacancy generation will lead to an expansion of the local volume by adding new lattice planes to the adjacent crystal, while vacancy annihilation at sinks will lead to a contraction of the local volume resulting from the elimination of lattice planes. In reality, dislocations and grain boundaries may not act as ideal vacancy sources and sinks. Some degree of vacancy supersaturation may be needed before these features can generate or annihilate vacancies.

The vacancy concentration in a crystalline solid containing vacancy sources and

sinks is defined as the number of vacancies per unit volume:

$$C_V = \frac{N_V}{U}, \tag{2.24}$$

where N_V is the number of vacancies and U is an arbitrary control volume element. The control volume element is taken at an arbitrary point in the lattice frame. Thus, the velocity relative to the laboratory frame is not included in the flux expressions. The rate of change in the vacancy concentration is obtained by taking the time derivative of Eq.(2.24):

$$\frac{\partial C_V}{\partial t} = \frac{\partial}{\partial t}\left(\frac{N_V}{U}\right) = \frac{1}{U}\frac{\partial N_V}{\partial t} - \frac{N_V}{U^2}\frac{\partial U}{\partial t}. \tag{2.25}$$

Here, the second term in Eq. (2.25) will not vanish because the volume of the arbitrary control volume element can change due to vacancy generation or annihilation. The rate of change in the number of vacancies is due to two factors. One factor accounts for the difference between incoming and outgoing vacancy fluxes, and is given by the divergence of the vacancy flux. The other factor accounts for the vacancies produced by the vacancy sources within the control volume:

$$\frac{\partial N_V}{\partial t} = \left(-\nabla \cdot J_V + g\right) U, \tag{2.26}$$

where g is the vacancy generation rate per unit volume. Similarly, the rate of change of the total number of all three species is expressed by

$$\frac{\partial}{\partial t}\left(N_V + N_A + N_B\right) = \left(-\nabla \cdot J_V + g - \nabla \cdot J_A - \nabla \cdot J_B\right) U. \tag{2.27}$$

Lattice site conservation, Eq. (2.3), is assumed on all faces of the control volume. Thus, the cumulative divergence of the fluxes is zero ($\nabla \cdot J_A + \nabla \cdot J_B + \nabla \cdot J_V = 0$). The total number of all species is related to the volume by $N_V + N_A + N_B = \rho U$. Since substitutional diffusion tends to take place when the diffusers have similar atomic sizes and the vacancy mole fraction is very small compared to the mole fractions of the atomic species, it is suitable to assume that the lattice density remains constant. Eq.

(2.27) is thus rewritten as

$$\frac{\partial U}{\partial t} = \frac{g}{\rho} U. \tag{2.28}$$

Substituting Eqs. (2.26) and (2.28) into (2.25), one obtains

$$\frac{\partial C_V}{\partial t} = -\nabla \cdot J_V + \left(1 - \frac{C_V}{\rho}\right) g, \tag{2.29}$$

where $C_V/\rho = X_V$. Following a similar procedure as in the derivation of Eq. (2.29), the rate of change of the B concentration is expressed by

$$\frac{\partial C_B}{\partial t} = \frac{\partial}{\partial t}\left(\frac{N_B}{U}\right) = \frac{1}{U}\frac{\partial N_B}{\partial t} - \frac{N_B}{U^2}\frac{\partial U}{\partial t} = -\nabla \cdot J_B - \frac{C_B}{\rho} g, \tag{2.30}$$

where $C_B/\rho = X_B$. Within a perfect lattice region with no vacancy sources or sinks, the vacancy generation rate is zero ($g = 0$). In this case, Eqs. (2.29) and (2.30) simplify to the standard diffusion equations for vacancy and B concentrations, respectively:

$$\frac{\partial C_V}{\partial t} = -\nabla \cdot J_V \quad \text{and} \quad \frac{\partial C_B}{\partial t} = -\nabla \cdot J_B. \tag{2.31}$$

Bulk diffusion within the perfect lattice regions between explicit vacancy sources and sinks will then be governed by Fick's Second Law, Eq. (2.31).

In the derivations of Eqs. (2.29) and (2.30), we do not specify the properties of the vacancy sources and sinks. These expressions should be valid for both ideal and non-ideal vacancy sources and sinks in the bulk (dislocations) or at boundaries (surfaces and grain boundaries). A typical non-ideal source or sink can be modeled by having the generation rate be proportional to $(C_V^{eq} - C_V)/\tau_V$, where τ_V is the lifetime of a vacancy, as proposed in Ref. [58]. In a macroscopic view, the vacancy lifetime in the bulk can be related to the ratio between the average vacancy source-sink distance and the vacancy drift velocity, defined as the flux divided by the concentration. Since our aim is to investigate vacancy diffusion in the presence of discretely distributed sources and sinks, we will defer the consideration of non-ideal sources and sinks to future work. Moreover, the above derivations are developed under the assumption

that the lattice density remains constant, which stems from two implicit assumptions. First, it is assumed that the molar volumes of all species in perfect lattice regions are equal. Analogous derivations that incorporate molar volume variations and interstitial fluxes are also available [108, 109, 110]. Second, the solid is assumed to be completely incompressible; that is, any increase or decrease in lattice sites immediately results in volume changes without elastic deformation. This assumption is acceptable when the geometry of the diffusion couple is thin and planar, such that a rigid shift can naturally take place. With more complex geometries, however, elastic deformation of the lattice structure can occur. Such deformation can result in an elastic stress, which can alter diffusion phenomena in some material systems that can sustain a large strain. Here, we ignore these factors for simplicity, which is acceptable with simple, small objects or for systems that easily deform plastically. This assumption has been made widely in the modeling of Kirkendall-effect-induced deformation [81].

At vacancy sources, g can be positive or negative depending on whether vacancies are injected into or eliminated from the crystal. For an ideal vacancy source or sink, the vacancy concentration at the source/sink position remains at the constant equilibrium value; thus, the time derivative goes to zero in Eq. (2.29). The vacancy generation rate is obtained by

$$g(\boldsymbol{r}_s) = \frac{\nabla \cdot J_V(\boldsymbol{r}_s)}{1 - X_V^{eq}}, \tag{2.32}$$

where $\boldsymbol{r}_s$ is the position vector of the vacancy source or sink, and X_V^{eq} is the vacancy mole fraction at thermodynamic equilibrium. By substituting Eq. (2.32) into (2.30), the rate of change of the B concentration at vacancy sources and sinks can be obtained:

$$\frac{\partial C_B}{\partial t} = -\nabla \cdot J_B - X_B \frac{\nabla \cdot J_V}{1 - X_V^{eq}}. \tag{2.33}$$

Equation (2.33) can be reformulated by applying lattice conservation, $X_A + X_B +$

$X_V^{eq} = 1$, to obtain

$$\frac{\partial C_B}{\partial t} = -\frac{1}{1 - X_V^{eq}} \nabla \cdot (X_A J_B - X_B J_A) \,, \tag{2.34}$$

which is similar to the equation obtained by directly substituting Eq. (2.20) into (2.14b), $\partial C_B / \partial t = -\nabla \cdot (X_A J_B - X_B J_A)$, except for the factor $1/(1 - X_V^{eq})$, which accounts for the nonzero vacancy mole fraction. When $X_V^{eq} = 0$, the above two equations become identical. Thus, the analysis again shows that Darken's model is only valid when there are uniformly distributed ideal sources/sinks in the solid. Here, the divergence operator should be considered to be a change in flux over a characteristic thickness of the source or sink region (which is of the lattice parameter scale). If vacancy sources and sinks are located at a surface or grain boundary, this value should be divided by the thickness of that region.

Now let us consider the local volume change in the immediate vicinity of a vacancy source or sink due to vacancy generation or annihilation. When lattice sites are created or annihilated, the rate of the fractional dilatational volume change is given by the vacancy generation rate according to Eq. (2.28):

$$\dot{\varepsilon}_\Omega = \frac{1}{U} \frac{\Delta U}{\Delta t} = \frac{g}{\rho}. \tag{2.35}$$

At an arbitrary point inside a solid, this expression applies to the three principal axes in a tensorial form: $\dot{\varepsilon}_\Omega \delta_{ij}$, where δ_{ij} is the Kronecker delta ($\delta_{ij} = 1$ for $i = j$, and $\delta_{ij} = 0$ for $i \neq j$). To maintain a constant lattice site density, this volume expansion/contraction will result in a lattice flow that moves fiducial markers in the laboratory frame.

At a free surface, lattice planes are generated or eliminated layer by layer parallel to the surface. The velocity of the surface is obtained by dividing the overall volume

change per unit time of an arbitrary cubic region by its cross-sectional area:

$$v_n = \frac{\Delta U}{S\Delta t} = \frac{gU}{\rho S} = \frac{g}{\rho} l_b, \tag{2.36}$$

where S is the cross-sectional area of the control volume element (parallel to the free surface), and l_b is the length of the control volume element perpendicular to the free surface (taken to be small). In a vector form, this expression is given by $\boldsymbol{v}_n = \boldsymbol{n}\dot{\varepsilon}_\Omega l_b$, where $\boldsymbol{n}$ is the unit normal vector of the surface. In a simpler case where no tangential diffusion is allowed, Eq. (2.36) can be written as

$$v_n = \frac{1}{(1 - X_V^{eq})\rho} \frac{\partial J_V}{\partial n} l_b. \tag{2.37}$$

The product of $\partial J_V / \partial n$ and l_b reflects that the velocity of a surface is, in fact, proportional to a jump in flux across the subsurface layer, as is commonly recognized. Therefore, we obtain:

$$v_n = \frac{1}{(1 - X_V^{eq})\rho} [J_V]_-^+, \tag{2.38}$$

where $[\ ]_-^+$ denotes the jump (change) of the flux across the surface region in the direction perpendicular to the surface. For convenience in numerical solutions, we solve Eq. (2.37), where a finite value of l_b is used. Physically, the value of l_b can be arbitrary as long as it is smaller than the characteristic thickness of the surface region acting as a source/sink. In practice, l_b can be taken to be larger than this limit, as long as the bulk changes of concentration fields over l_b are small enough, which should hold when l_b is much smaller than the typical diffusion length of the system.

For a grain boundary, the velocity of the grain boundary with respect to the grain into which vacancies are injected (or from which they are eliminated) can be similarly obtained. Since a grain boundary adjoins two grains, there are two velocities, v_α and v_β, associated with each grain, defined relative to the corresponding grains. The net

velocity of the second grain with respect to the first grain is thus

$$v_{\beta-\alpha} = v_\beta - v_\alpha. \tag{2.39}$$

When calculating the evolution of a planar system containing grain boundaries, the velocities of all grains with respect to one grain assumed to be fixed to the reference frame can be calculated from the individual values of relative velocities [111]. Alternatively, plastic deformation can be calculated based on the assumption of incompressible viscous flow for more general cases.

2.4 Kinetic Transport Coefficient

In a substitutional crystalline solid, atoms are located in a well-defined lattice network with small thermal fluctuations. Occasionally, atoms change their positions by moving to vacant neighboring positions. These quantized motions are referred to as diffusive hops, and take place through substitutional lattice networks. When averaged over time, the mean-square atomic hop distances of their trajectory can serve as an indication of their kinetic transport coefficients as in, for example, the Einstein formulation [112] for a random-walk process. The probability of a successful diffusive hop depends on the energy of local states and the frequency of thermal vibrations, and can be described from a statistical point of view [113]: $\Gamma = \nu \exp\left(-\Delta E_b / k_B T\right)$, where ν is the vibration prefactor with units of Hz, ΔE_b is the activation barrier, k_B is the Boltzmann constant, and T is the absolute temperature. Since atoms only exchange positions with neighboring vacant sites, the next hop is related to the previous hop. Thus, the hop trajectories will not follow a true random walk process, and the mean-square displacement for a general sequence of hops needs to be modified by a correlation factor.

In this dissertation, we select a thermodynamically ideal random alloy system where the interactions between A, B, and V are assumed to be identical for simplic-

ity without the loss of important physics. Analytical expressions of the correlation factors for a thermodynamically ideal random binary substitutional alloy have been derived by Manning [99] based on the vacancy-mediated mechanism for atomic hops. An equivalent expression has also been analytically derived by Moleko [100], using a self-consistent formalism. The kinetic transport coefficients for such a system are expressed in terms of the atomic hop frequencies of the diffusing species, the composition of the alloy, and parameters that depend on the lattice structure:

$$L_{AA} = \frac{\lambda a^2}{\Omega k_B T} X_V X_A \Gamma_A \left(1 - \frac{2X_B\Gamma_A}{\Lambda}\right), \tag{2.40a}$$

$$L_{BB} = \frac{\lambda a^2}{\Omega k_B T} X_V X_B \Gamma_B \left(1 - \frac{2X_A\Gamma_B}{\Lambda}\right), \tag{2.40b}$$

$$L_{AB} = L_{BA} = \frac{2\lambda a^2}{\Omega k_B T} X_V \frac{X_A X_B \Gamma_A \Gamma_B}{\Lambda}, \tag{2.40c}$$

where λ is the geometric factor that depends on the structure of the lattice, a is the atomic hop distance, $\Omega = 1/\rho$ is the atomic volume, Γ_i is the hop frequency of the *i-th* diffusing species,

$$\begin{aligned}\Lambda =& \frac{1}{2}(F+2)(X_A\Gamma_A + X_B\Gamma_B) - \Gamma_A - \Gamma_B + 2(X_A\Gamma_B + X_B\Gamma_A) + \\ & \sqrt{\left[\frac{1}{2}(F+2)(X_A\Gamma_A + X_B\Gamma_B) - \Gamma_A - \Gamma_B\right]^2 + 2F\Gamma_A\Gamma_B},\end{aligned} \tag{2.41}$$

and $F = 2f_0/(1-f_0)$, where f_0 is the geometric correlation factor. The factor $(\lambda a^2 X_V X_i \Gamma_i)/\Omega k_B T$, in Eq. (2.40) is the uncorrelated kinetic coefficient in a cubic system. For a single component face-centered-cubic (fcc) crystal, $\lambda = 1/6$ and $f_0 = 0.7815$.

In a thermodynamically non-ideal alloy where atoms may develop a short- or long-range order, the kinetic transport coefficient needs to be statistically evaluated by averaging the atomic hopping trajectories in a form analogous to the well-known

Einstein equation [114]:

$$L_{ij} = \frac{\left\langle \left(\sum_p \Delta \vec{R}_p^i \left(t \right) \right) \cdot \left(\sum_q \Delta \vec{R}_q^j \left(t \right) \right) \right\rangle}{2dtM\Omega k_B T}, \tag{2.42}$$

where $\Delta \vec{R}_p^i$ is the vector linking the end points of the trajectory of atom p of species i after time t, d is the dimensionality of the lattice network, and M is the total number of lattice sites. The angle brackets denote an ensemble average for the system at equilibrium. For a thermodynamically ideal binary alloy, the kinetic transport coefficients predicted by Eq. (2.42) have been shown to be in excellent agreement [115, 106] with that predicted by analytical theory, Eq. (2.40). Figure 2.1 shows an example of the kinetic transport coefficients for an ideal random binary alloy predicted by kinetic Monte Carlo simulations and the analytical formulae in cases where the fast-to-slow atomic hop frequency ratio varies from 1 to 100. The results from the two different approaches match very well. When the two atomic diffusing species have equal hop frequency (i.e., $\Gamma_A = \Gamma_B$), the kinetic transport coefficient matrix is symmetric and their values are also symmetric across $X_B = 0.5$. The diagonal terms (L_{AA} and L_{BB}) are roughly one order of magnitude larger than the off-diagonal term ($L_{AB} = L_{BA}$), in agreement with Ref. [107]. When the fast-to-slow atomic hop frequency ratio increases, this symmetry is broken. Figure 2.1 clearly shows that the kinetic transport coefficient of the fast diffuser increases as its hop frequency, Γ_B, is increased.

While the kinetic transport coefficients can describe diffusion when the chemical driving force is known, a diffusivity that takes into account thermodynamic factors is required when the fluxes are expressed in terms of the concentration gradients. In an ideal, random alloy, only the configurational entropy is significant in the Gibbs free energy. According to the ideal mixing condition, the free energy per lattice site of an

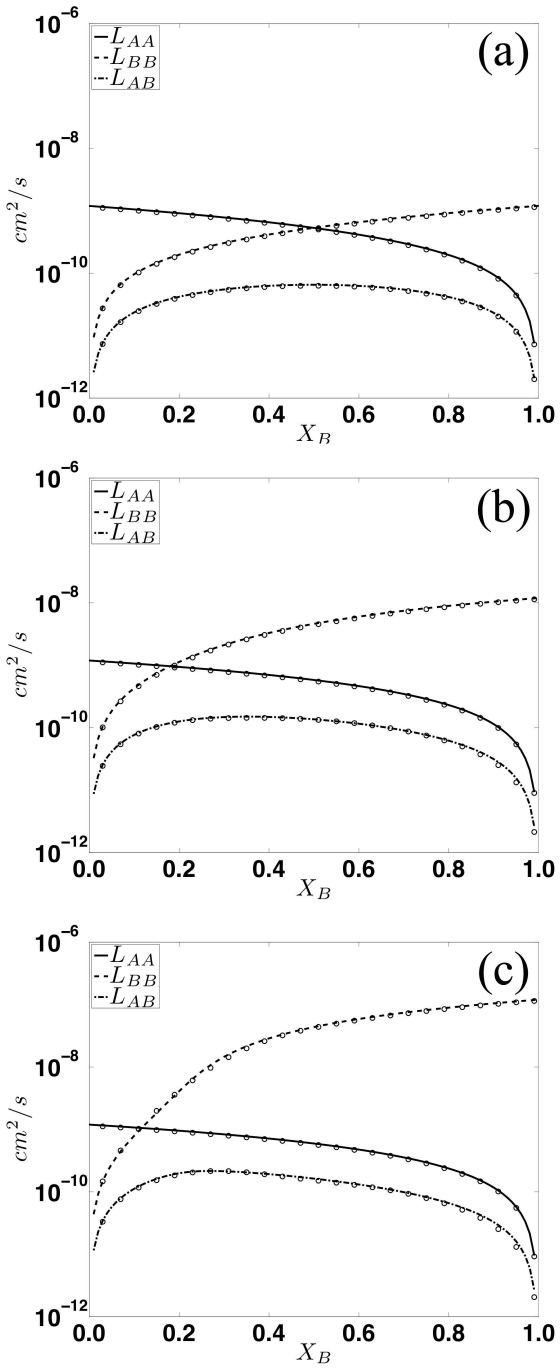

Figure 2.1: The kinetic transport coefficients evaluated for a thermodynamically ideal binary random alloy: (a) $\Gamma_B = \Gamma_A$, (b) $\Gamma_B = 10\Gamma_A$, and (c) $\Gamma_B = 100\Gamma_A$. The analytically evaluated values are depicted in solid lines. The circular markers depict the values obtained by curve fitting results of Kinetic Monte Carlo simulations provided by Prof. Anton Van der Ven (Ref. [106]). The vacancy mole fraction used in the calculation is 0.002.

A-B alloy containing vacancies is given by

$$G\left(X_A, X_B\right) = k_B T\left[X_A \ln(X_A) + X_B \ln(X_B) + X_V \ln(X_V)\right]. \tag{2.43}$$

By substituting Eq. (2.43) into (2.6) and (2.10), the diffusion coefficients appearing in Eqs. (2.8) and (2.11) can be obtained. Figure 2.2 shows the diffusion coefficients in a perfect lattice region for a thermodynamically ideal, random alloy analytically calculated using the above-mentioned procedure. The parameters used to calculate the diffusion coefficients are listed in Table 3.1. As can be seen in Figs. 2.2(a) and (c), the diffusion coefficients accompanying vacancy concentration gradients (D_{VV} and D_{BV}) are highly dependent upon the mole fraction X_B, indicating that vacancies are more mobile when they are more likely to have neighboring fast diffuser atoms. On the other hand, for a dilute vacancy concentration ($X_V < 10^{-4}$), the dependence of D_{VV} and D_{BV} on the vacancy mole fraction is negligible, showing that vacancies rarely interact with each other at this limit. The diffusion coefficients associated with the fast diffuser mole fraction, D_{VB} and D_{BB}^{V}, are almost linearly proportional to X_V. This result reflects the fact that the fast diffuser is more mobile when it has a higher chance of exchanging with vacancies. Although D_{VB} and D_{BB}^{V} clearly increase as X_B increases, slow increases are observed in both the low and high X_B regimes. This phenomenon is more pronounced in Fig. 2.2(d). In the low X_B region, vacancies can only exchange with the slow diffuser; thus, D_{BB}^{V} is low. The rapid increase of D_{BB}^{V} in the intermediate region of X_B concentration reflects a percolation transition of the lattice network as the concentration changes. Once the structure is percolated by B atoms, D_{BB}^{V} again increases relatively slowly.

2.5 Vacancy Sources and Sinks

It is well known that expansion and marker motion are larger in a polycrystalline diffusion couple than they are in a single crystal diffusion couple made of the same

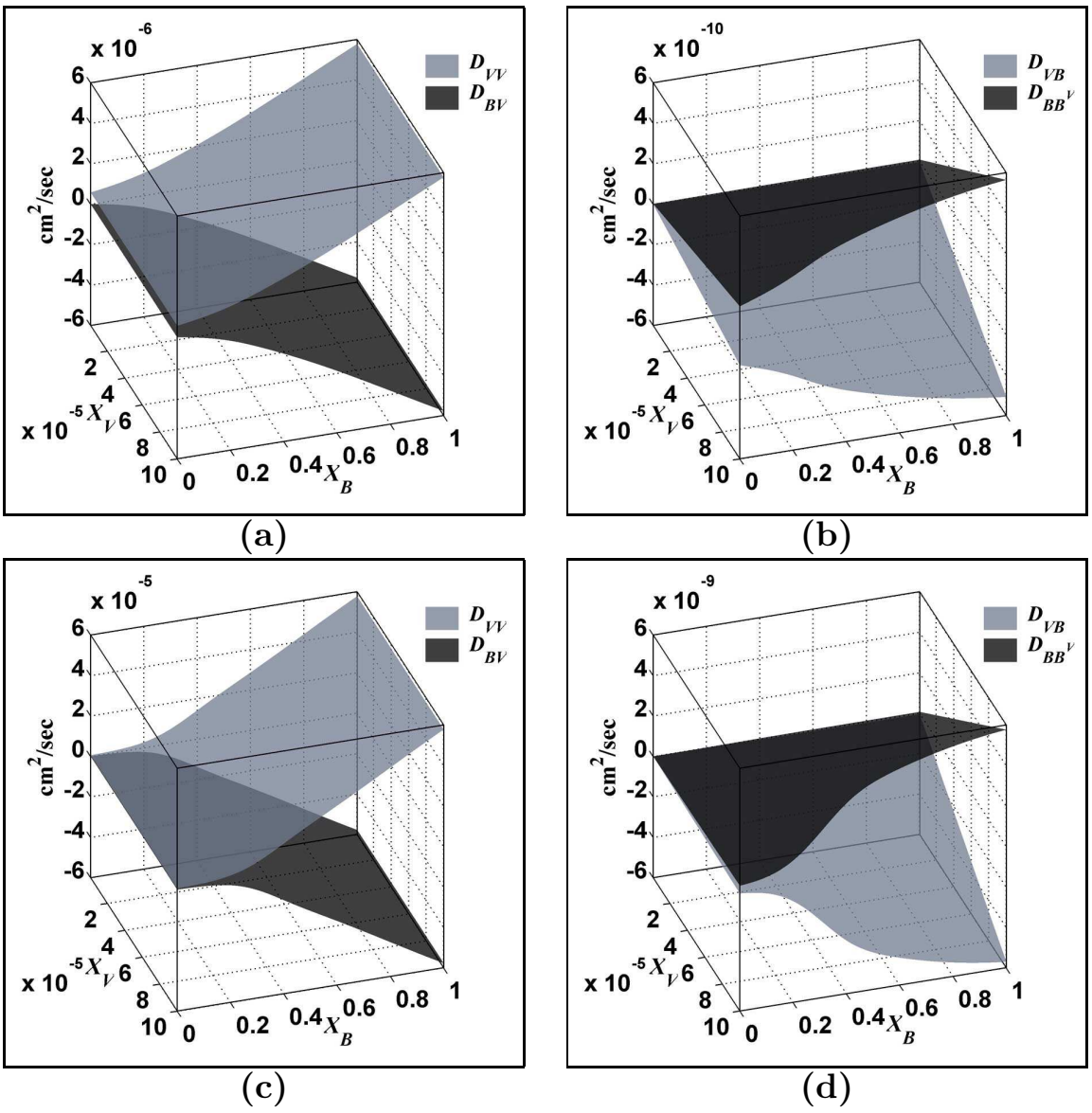

Figure 2.2: Diffusion coefficients determined by self-consistent phenomenological kinetic coefficients for a perfect binary crystal: (a) and (b) $\Gamma_B = 10\Gamma_A$; (c) and (d) $\Gamma_B = 100\Gamma_A$. The physical parameters used for the calculation are listed in Table 3.1.

material [116, 43, 14]. These increases are not believed to originate from grain boundary diffusion because grain boundary diffusion was not significantly enhanced in these systems. Moreover, a marked reduction in porosity was also reported for polycrystalline specimens during diffusion [43, 117], especially in regions within tens of microns of grain sizes. These results demonstrate that grain boundaries are important sources and sinks of vacancies in diffusion involving the Kirkendall effect, as indicated by Balluffi's work [43].

It is commonly accepted that both grain boundaries and dislocations serve as sources and sinks of vacancies that mediate substitutional diffusion. In pure metals with a low stacking fault energy, such as pure gold, dislocations are highly efficient vacancy sources/sinks due to the high dislocation density ($\sim 2.5 \times 10^7$ cm^{-2}) and the relatively low energy barrier for dislocation climb [118]. However, the efficiency of dislocations as vacancy sources/sinks decreases dramatically in alloys. For example, experimental data have shown that the dislocation's source/sink efficiency decreases by a factor of thousands in a Au 0.1 at.% Ag alloy compared to pure gold, mainly because of the large energy barrier for dislocation climb [119]. Moreover, in metals with a large stacking fault energy, such as aluminum, the dislocation density is low ($\sim 2.5 \times 10^5$ cm^{-2}), which makes grain boundaries more important as vacancy sources/sinks. Here, we perform a simple analysis to determine when grain boundaries dominate dislocations as vacancy sources/sinks in aluminum alloys.

A void-free or staking fault-free zone usually forms in the vicinity of grain boundaries in quenched metals [120, 121, 122, 123], implying that grain boundaries are usually more efficient than dislocations at generating and eliminating vacancies. In spite of this observation, we assume dislocations and grain boundaries to be equally efficient vacancy sources/sinks in this analysis. A parameter, ϖ, is defined as the number of vacancies accommodated by vacancy sources and sinks per unit area, such that the total number of vacancies accommodated by a grain boundary in a charac-

teristic time is given by

$$Q_{gb} = \varpi_{gb} A_{gb} \frac{t_c}{\tau_{gb}}, \tag{2.44}$$

where the subscript 'gb' denotes quantities at grain boundaries, t_c is a characteristic time, and τ_{gb} is the average diffusion time of vacancies within a grain to a grain boundary. If R is the radius of a representative grain, the grain boundary area is $A_{gb} = 4\pi R^2$ when approximating the grain as a sphere. The diffusion time is related to the effective diffusivity by $\tau_{gb} = R^2/D_{eff}$. Analogously, we can describe the total number of vacancies accommodated by dislocations in a characteristic time as

$$Q_d = \zeta_d l_d \frac{t_c}{\tau_d}, \tag{2.45}$$

where the subscript 'd' denotes quantities at dislocations, ζ_d is the number of vacancies accommodated by dislocations per unit length, l_d is the total length of dislocations in the volume considered, and τ_d is the vacancy diffusion time over a typical distance between a vacancy and a dislocation. The product of the dislocation length and the Burger's vector can be considered to be the effective area of the dislocations. Thus, Eq. (2.45) can be rewritten to resemble Eq. (2.44):

$$Q_d = \frac{\zeta_d}{b} l_d b \frac{t_c}{\tau_d} = \varpi_d l_d b \frac{t_c}{\tau_d}, \tag{2.46}$$

where b is the Burger's vector. For a spherical grain, $l_d = (4\pi R^3/3)\rho_d$, where ρ_d is the dislocation density. The typical distance between a vacancy and a dislocation is approximated by $r_d = \sqrt{1/\pi\rho_d}$. Therefore, the typical diffusion time for vacancies to diffuse to a dislocation is obtained by $\tau_d = r_d^2/D_{eff} = 1/\pi\rho_d D_{eff}$. Dividing Eq. (2.44) by (2.46) and substituting these quantities, we obtain

$$\frac{Q_{gb}}{Q_d} = \frac{3\varpi_{gb}}{\pi\varpi_d R^3 \rho_d^2 b}. \tag{2.47}$$

Since we assume that grain boundaries and dislocations have equal efficiencies ($\varpi_{gb} = \varpi_d$), using $\rho_d = 2.5 \times 10^5$ cm^{-2} and $b = 2.9 \times 10^{-8}$ cm typical for aluminum alloys,

Eq. (2.47) gives the ratio of the number of vacancies accommodated by the grain boundary to that accommodated by dislocations:

$$\frac{Q_{gb}}{Q_d} = \frac{5.3 \times 10^{-4} \text{ cm}^3}{R^3}. \tag{2.48}$$

Therefore, when R is smaller than 0.081 cm (810 μm), grain boundaries accommodate more vacancies than dislocations. This relation also shows that, as the average grain radius decreases, the ability of grain boundaries to accommodate vacancies increases as the cube of the radius; thus, the importance of grain boundaries increases as the size of the grain decreases. If the dislocation density is small or the ratio of grain boundary efficiency to dislocation efficiency is large, the average grain size at which more vacancies will be accommodated by grain boundaries is even larger. Moreover, since dislocations are less efficient vacancy sources and sinks in alloys, the assumption that grain boundaries are the dominant vacancy sources and sinks should be valid in a wide range of metallic alloys with grain size on a micron scale. For metals having 1000 times higher dislocation density ($\rho_d = 2.5 \times 10^8$ cm^3), R is reduced to 8.1 μm, which is still a realistic grain size, though much smaller than the prediction for a typical alloy. This analysis also shows that a rigorous treatment of the Kirkendall effect is essential for submicron-scale objects.

CHAPTER III

ONE-DIMENSIONAL SHARP INTERFACE SIMULATIONS

A model was examined on the continuum level for effectively one-dimensional (1D) diffusion couples that consist of a slow diffuser (A), a fast diffuser (B), and vacancies (V). For the 1D planar case, the fast diffuser initially occupies the left half of the diffusion couple, while the slow diffuser occupies the right half. For the cylindrical case, the fast diffuser is initially located in the center region, while the slow diffuser is located in the outer region. The vacancy concentration is initially assumed to be at equilibrium value throughout the diffusion couple. We model a thermodynamically ideal alloy with complete solubility for all diffusion species such that no inter-metallic compound, precipitate, or void will form during diffusion. For perfect lattice regions, the Gibbs free energy is given by Eq. (2.43). The physical parameters of this arbitrary alloy used in the simulations are listed in Tables 3.1 and 3.2. These quantities are used to evaluate the diffusion coefficients for the alloy, which are shown in Fig. 2.2. The evolution of the concentration is simulated for cases with two different ratios between hop frequencies of B and A: $\Gamma_B = 10\Gamma_A$ and $\Gamma_B = 100\Gamma_A$. In an effective 1D calculation, the divergence operator is givens as

$$\nabla \cdot D\nabla C = \frac{1}{r^p}\frac{d}{dr}\left(r^p D\frac{dC}{dr}\right), \tag{3.1}$$

where r is the coordinate variable. In the planar case, r is the coordinate variable along the x axis. In the cylindrical case, r is the coordinate variable along the radial

direction. The exponent p is given by 0 and 1 for planar and cylindrical geometries, respectively. (For spherical symmetry, $p = 2$.) In order to characterize the system with respect to its final equilibrium state during the diffusion process, we define a parameter

$$\Xi = 1 - \theta = 1 - \frac{\sqrt{\int_{r_i(t)}^{r_o(t)} \left[C_B(r,t) - C_B^{eq}\right] r^p dr}}{\sqrt{\int_{r_i(0)}^{r_o(t)} \left[C_B(r,0) - C_B^{eq}\right] r^p dr}}, \tag{3.2}$$

where θ is the deviation parameter, r_i is the left end of the domain, r_o is the right end of the domain, and C_B^{eq} is the average concentration over the entire diffusion couple (which is the final equilibrium B concentration):

$$C_B^{eq} = \frac{\int_{r_i(0)}^{r_o(0)} C_B(r,0) r^p dr}{\int_{r_i(0)}^{r_o(0)} r^p dr}. \tag{3.3}$$

In a cylindrical geometry, r_i and r_o will be the inner and outer radii, respectively. Therefore, $\Xi = 0$ for the initial state, and $\Xi = 1$ for the final equilibrium state.

3.1 One-Dimensional Planar System

In the one-dimensional planar simulations, the fast diffuser initially occupies the left half of the diffusion couple, while the slow diffuser occupies the right half. Equation (2.31) can be non-dimensionalized by scaling with a reference diffusion coefficient D_0 and the lattice density ρ, and defining a time scale τ for a given length scale l as $\tau = l^2/D_0$:

$$\begin{aligned} \frac{\partial \rho X_V}{\partial \tau \hat{t}} =& \frac{\partial}{\partial l\hat{x}} \left(\hat{D}_{VV} D_0 \frac{\partial \rho X_V}{\partial l\hat{x}} \right) + \frac{\partial}{\partial l\hat{x}} \left(\hat{D}_{VB} D_0 \frac{\partial \rho X_B}{\partial l\hat{x}} \right) \\ \implies \frac{D_0 \rho}{l^2} \left(\frac{\partial X_V}{\partial \hat{t}} \right) =& \frac{D_0 \rho}{l^2} \left[\frac{\partial}{\partial \hat{x}} \left(\hat{D}_{VV} \frac{\partial X_V}{\partial \hat{x}} \right) + \frac{\partial}{\partial \hat{x}} \left(\hat{D}_{VB} \frac{\partial X_B}{\partial \hat{x}} \right) \right] \\ \implies \frac{\partial X_V}{\partial \hat{t}} =& \frac{\partial}{\partial \hat{x}} \left(\hat{D}_{VV} \frac{\partial X_V}{\partial \hat{x}} \right) + \frac{\partial}{\partial \hat{x}} \left(\hat{D}_{VB} \frac{\partial X_B}{\partial \hat{x}} \right), \end{aligned} \tag{3.4a}$$

$$
\begin{aligned}
\frac{\partial \rho X_B}{\partial \tau \hat{t}} =& \frac{\partial}{\partial l\hat{x}}\left(\hat{D}_{BV} D_0 \frac{\partial \rho X_V}{\partial l\hat{x}}\right) + \frac{\partial}{\partial l\hat{x}}\left(\hat{D}^V_{BB} D_0 \frac{\partial \rho X_B}{\partial l\hat{x}}\right) \\
\implies \frac{D_0\rho}{l^2}\left(\frac{\partial X_B}{\partial \hat{t}}\right) =& \frac{D_0\rho}{l^2}\left[\frac{\partial}{\partial \hat{x}}\left(\hat{D}_{BV}\frac{\partial X_V}{\partial \hat{x}}\right) + \frac{\partial}{\partial \hat{x}}\left(\hat{D}^V_{BB}\frac{\partial X_B}{\partial \hat{x}}\right)\right] \\
\implies \frac{\partial X_B}{\partial \hat{t}} =& \frac{\partial}{\partial \hat{x}}\left(\hat{D}_{BV}\frac{\partial X_V}{\partial \hat{x}}\right) + \frac{\partial}{\partial \hat{x}}\left(\hat{D}^V_{BB}\frac{\partial X_B}{\partial \hat{x}}\right),
\end{aligned}
\tag{3.4b}
$$

where $\hat{t} = t/\tau$, $\hat{x} = x/l$, $X_i = C_i/\rho$, and $\hat{D}_{ij} = D_{ij}/D_0$ are the non-dimensionalized quantities for time, space, concentration, and diffusion coefficients, respectively. Here, we choose $l = 1$ μm, $D_0 = 1.0 \times 10^{-10}$ cm^{2}s^{-1} and thus $\tau = 1.0 \times 10^2$ s to demonstrate the concentration evolution on realistic length and time scales. The diffusion coefficients are calculated using the physical parameters listed in Table 3.1. These equations are numerically solved for the mole fraction evolution in the bulk regions between vacancy sources and sinks by using the central finite difference scheme in space and the explicit Euler scheme in time. At the locations of vacancy sources and sinks, the B mole fraction is calculated semi-implicitly by

$$
X_B(\hat{t} + \Delta\hat{t}) = \frac{(1 - X_V^{eq})[X_B(t) - \partial \hat{J}_B(\hat{t})/\partial\hat{x}\Delta\hat{t}]}{(1 - X_V^{eq}) + \partial \hat{J}_V/\partial\hat{x}\Delta\hat{t}},
\tag{3.5}
$$

where $\hat{J}_V = -\hat{D}_{VV}\partial X_V/\partial\hat{x} - \hat{D}_{VB}\partial X_B/\partial\hat{x}$ and $\hat{J}_B = -\hat{D}_{BV}\partial X_V/\partial\hat{x} - \hat{D}^V_{BB}\partial X_B/\partial\hat{x}$ are the non-dimensionalized fluxes. Equation (3.5) is obtained from Eq. (2.33) by taking B concentration appearing on the right-hand side at $t + \Delta t$, while calculating other quantities at t (to be consistent with the derivation in Appendix A). Vacancy mole fraction is kept at its equilibrium value at the vacancy sources and sinks, which, along with the B mole fraction calculated from Eq. (3.5), serves as the boundary conditions for solving Eq. (3.4) in the bulk regions. During simulations, spacings of grid points containing sources and sinks of vacancy evolve due to the creation and elimination of vacancies. The grid spacing is updated in time according to Eq. (2.36):

$$
\hat{u}(\hat{t} + \Delta\hat{t}) = \hat{u}(\hat{t})[1 + \hat{g}(\hat{t})\Delta\hat{t}] = \hat{u}(\hat{t})\left[1 + \frac{\partial \hat{J}_V(\hat{t})/\partial\hat{x}}{1 - X_V^{eq}}\Delta\hat{t}\right],
\tag{3.6}
$$

where $\hat{g} = g/(\rho\tau)$ is the non-dimensionalized vacancy generation rate. Since these above equations are calculated in the local lattice frame, it is necessary to set a global reference frame in order to describe the volume changes in the system. Because the choice of the reference frame only presents a rigid translation of the system (not altering the physics), we set it at the center of the initial computation domain. The diffusion couple is assumed to be a completely incompressible material. The displacement of each grid point is calculated by summing all displacements due to local volume changes occurring between the grid point and the reference frame: $\hat{x}(\hat{t} + \Delta\hat{t}) = \hat{x}(\hat{t}) + \sum_k \Delta\hat{u}_k(\hat{t})$, where the index k denotes the k-th vacancy source or sink between the grid point and the reference point. To ensure accuracy, we insert an additional grid point when the grid size becomes 1.5 times the initial grid spacing and eliminate a grid point when the size becomes less than one half of the initial grid spacing. The changes in grid spacing occur only at the points of the sources and sinks; thus, the spacings of grid points without vacancy sources or sinks remain at their initial size. Throughout the simulations, the elastic effects caused by volume changes and interactions between defects are excluded for simplicity; we only consider purely diffusional processes. Furthermore, since the equations are solved in a moving coordinate system, explicit advection is not required.

Lattice Constant (a_l)	4.05 Å
Atomic Volume per Lattice Site (Ω)	1.661×10^{-23} cm^3
Lattice Site Density (ρ)	6.021×10^{22} cm^{-3}
Equilibrium Vacancy mole fraction (X_V^{eq})	4.6×10^{-6}
Hopping Frequency of Slow diffuser (Γ_A)	5.8×10^{7} Hz

Table 3.1: Material properties used in the computer simulations. The lattice size is similar to that of aluminum.

3.1.1 Isolated Single Crystal

In the first simulation, the crystalline alloy is assumed to contain no vacancy sources, such as grain boundaries or dislocations. Therefore, no lattice sites are created or

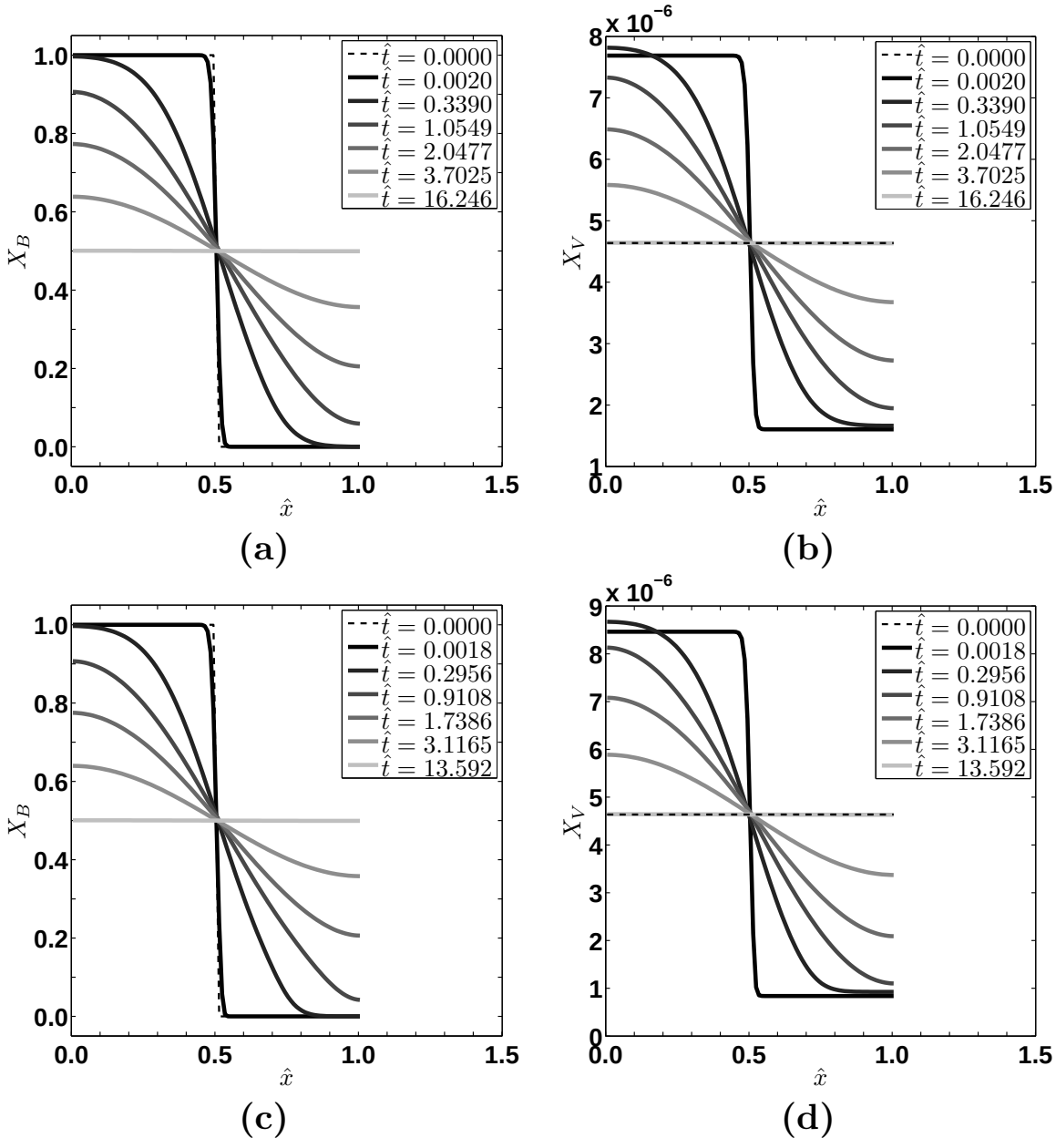

Figure 3.1: Mole fraction profiles, in an isolated single-crystal solid, of (a) B atoms and (b) vacancies for $\Gamma_B = 10\Gamma_A$; (c) B atoms and (d) vacancies for $\Gamma_B = 100\Gamma_A$. The concentration profiles at various times correspond to $\Xi = 0$, 0.01, 0.2, 0.4, 0.6, 0.8, and 0.999, which is defined in Eq. (3.2). For the vacancy concentration profiles, the initial vacancy concentration profile coincides with the final vacancy concentration profile.

eliminated during substitutional diffusion; thus, no volume changes are allowed. Furthermore, the injection or ejection of vacancies at the free surfaces from the environment is also precluded; that is, the crystal is assumed to be isolated from its environment. Figure 3.1 shows the mole fraction evolution of the fast diffuser and the vacancy for the thermodynamically ideal model alloys having $\Gamma_B = 10\Gamma_A$ and $\Gamma_B = 100\Gamma_A$. In the early stage, the vacancies diffuse from the A-rich region to the B-rich region in the same direction as the slow diffuser (A). This is a manifestation of the Kirkendall effect in the absence of local sources and sinks, which would allow equilibration of the vacancy concentration. The vacancies are much more likely to exchange with the fast diffuser. Thus, vacancies accumulate in the B-rich region within a short time, diffusing up a vacancy concentration gradient. Simultaneously, the fast diffuser (B) diffuses in the opposite direction. When B atoms diffuse and reach the A-rich region, the rapid accumulation of vacancies ends and is followed by a spreading of vacancies over the entire crystal. The system eventually reaches equilibrium with the concentrations of all three species uniformly distributed throughout the domain.

3.1.2 Single Crystal Solid

In the second simulation, the free surfaces are now assumed to be vacancy sources and sinks at which the vacancy mole fraction is maintained at its equilibrium value, X_V^{eq}. As before, we still assume that the crystal contains no vacancy sources inside the solid. Figure 3.2 shows the mole fraction evolution in this case. Initially, the fast diffuser, B, diffuses toward the A-rich region, reducing the vacancy concentration in the A-rich region and enhancing it in the B-rich region. Nonetheless, vacancies are injected at the free surface on the A-rich side in order to maintain X_V^{eq} at the free surface. These newly created vacancies flow into the crystal and result in the creation of lattice sites. As a result, the region near the A-side free surface undergoes an expansion. On the other hand, the region near the B-side free surface contracts due

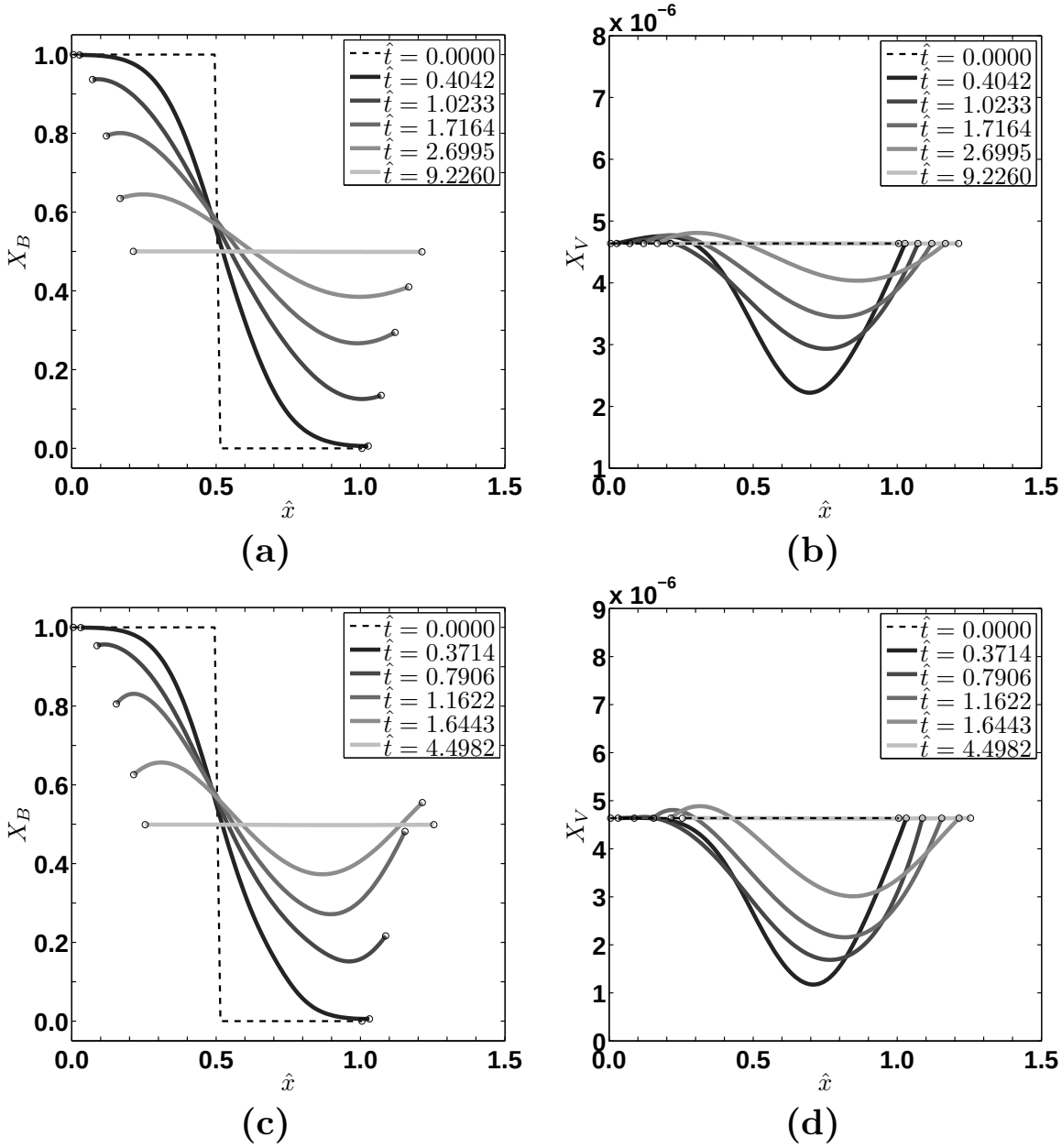

Figure 3.2: Mole fraction profiles, in a single crystal solid with two free surfaces, of (a) B atoms and (b) vacancies for $\Gamma_B = 10\Gamma_A$; (c) B atoms and (d) vacancies for $\Gamma_B = 100\Gamma_A$. The concentration profiles at various times correspond to $\Xi = 0$, 0.2, 0.4, 0.6, 0.8, and 0.999. The circular markers denote the vacancy sources.

to lattice site annihilation by ejection of vacancies. Therefore, the center of mass of the crystal shifts in space toward the A-rich side.

In the early stage, the evolution is more rapid in the B-rich side; thus, the volume contraction near the vacancy sink (negative source) is greater than the expansion near the source on the A-rich side. Consequently, the crystal initially shrinks. The rate of expansion at the vacancy source on the A-rich side increases as the region becomes enriched by B. Eventually, the vacancy mole fraction becomes uniform, attaining its equilibrium value; thus, the crystal recovers its original length, as it should, since the initial vacancy concentration and final vacancy concentration are the same.

The results also show segregation of B near the free surfaces on the A-rich side and depletion of B on the B-rich free surface. The effect is more pronounced in the $\Gamma_B = 100\Gamma_A$ case in Fig. 3.2(c). The segregation on the right-hand side can be explained as follows. Since substitutional diffusion occurs by exchange of sites between atoms and vacancies, it results in compensating fluxes; i.e., $J_B + J_A = -J_V$. Since A atoms are the slow diffuser, $J_A < J_B$. Near and at the free surface, J_V is negative and nonzero. Thus, J_B is positive near the surface, except for at the surface, where J_B is zero, since B atoms cannot leave the solid. This results in an accumulation of B atoms. The uphill diffusion of B is due to the large vacancy flux that must be predominantly compensated by the B flux. The depletion of B on the left-hand-side boundary is understood in a similar manner, where the vacancy flux is due to the presence of a vacancy sink. Depletion of the fast diffuser implies enhancement of the slow diffuser at the dilute vacancy limit. This phenomenon is also observed in irradiated materials, where segregation of a slow diffuser at grain boundaries occurs due to the so-called inverse Kirkendall effect [51, 52, 53].

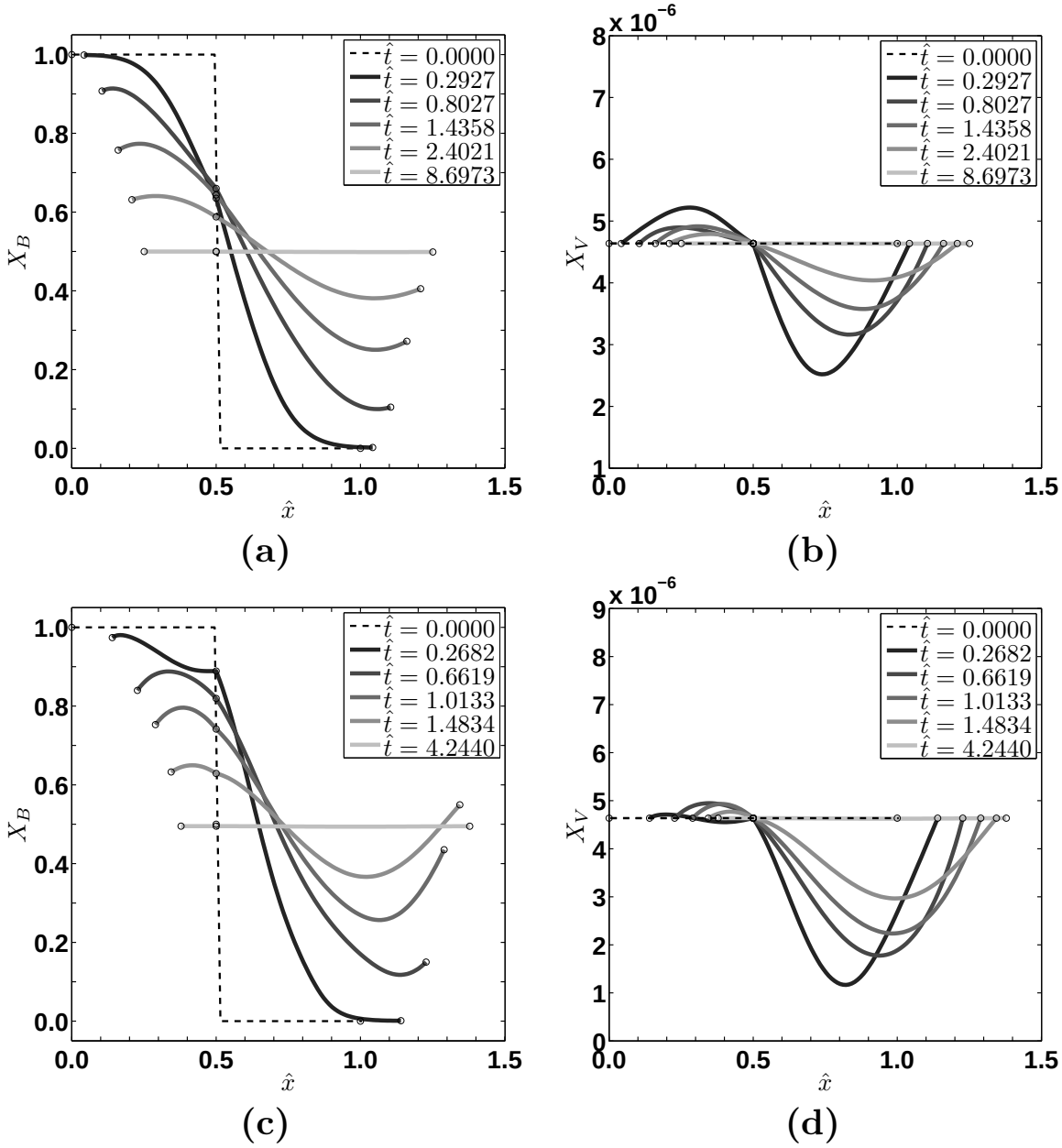

Figure 3.3: Mole fraction profiles, in a bicrystal solid with two free surfaces, of (a) B atoms and (b) vacancies for $\Gamma_B = 10\Gamma_A$; (c) B atoms and (d) vacancies for $\Gamma_B = 100\Gamma_A$. The concentration profiles at various times correspond to $\Xi = 0$, 0.2, 0.4, 0.6, 0.8, and 0.999. The circular markers denote the vacancy sources.

3.1.3 Bicrystal Solid

In the next simulation, one grain boundary is placed in the middle of the solid with two free surfaces; that is, the solid is a bicrystal. Figure 3.3 shows the concentration evolution for this case. During the initial stage of diffusion, the grain boundary immediately provides vacancies required for the diffusion of the fast diffuser, B, near the grain boundary. As a result, segregation of B near the central grain boundary occurs in a similar manner to that observed in the single crystal case on the free surface. At the internal source, a "kink" in the concentration profile of B forms. This phenomenon is more apparent in the $\Gamma_B = 100\Gamma_A$ case [see X_B profile for $\Gamma_B = 100\Gamma_A$ case at $\hat{t} = 0.2682$ in Fig 3.3(c)]. In the middle to late stage of diffusion ($\Xi \geq 0.4$), the fluxes abate as the concentration distributions become more uniform. The kinks in the concentration profiles also disappear. The vacancies created at the central grain boundary and the A-side free surface pass through the left grain and are ejected at the left free surface. Since more vacancies are annihilated at the left free surface than are produced at the central grain boundary, the originally B-rich left grain shrinks. On the other hand, the originally A-rich grain elongates due to the injection of vacancies at the right free surface and at the central grain boundary. Therefore, the imbalance in vacancy exchange rates between the fast and slow diffusers causes an effective grain coarsening even in the absence of the Gibbs-Thomson effect. This is a manifestation of a Kirkendall-effect-induced grain coarsening.

3.1.4 Tricrystal Solid

We also simulated a tricrystal solid that initially contains three equal-sized grains. Figure 3.4 shows the concentration evolution when two grain boundaries and two free surfaces act as vacancy sources and sinks. The grain boundary between the right and central grains acts as a strong vacancy source; this causes segregation of B and a kink in the B concentration profile in the early to middle stage of diffusion [see

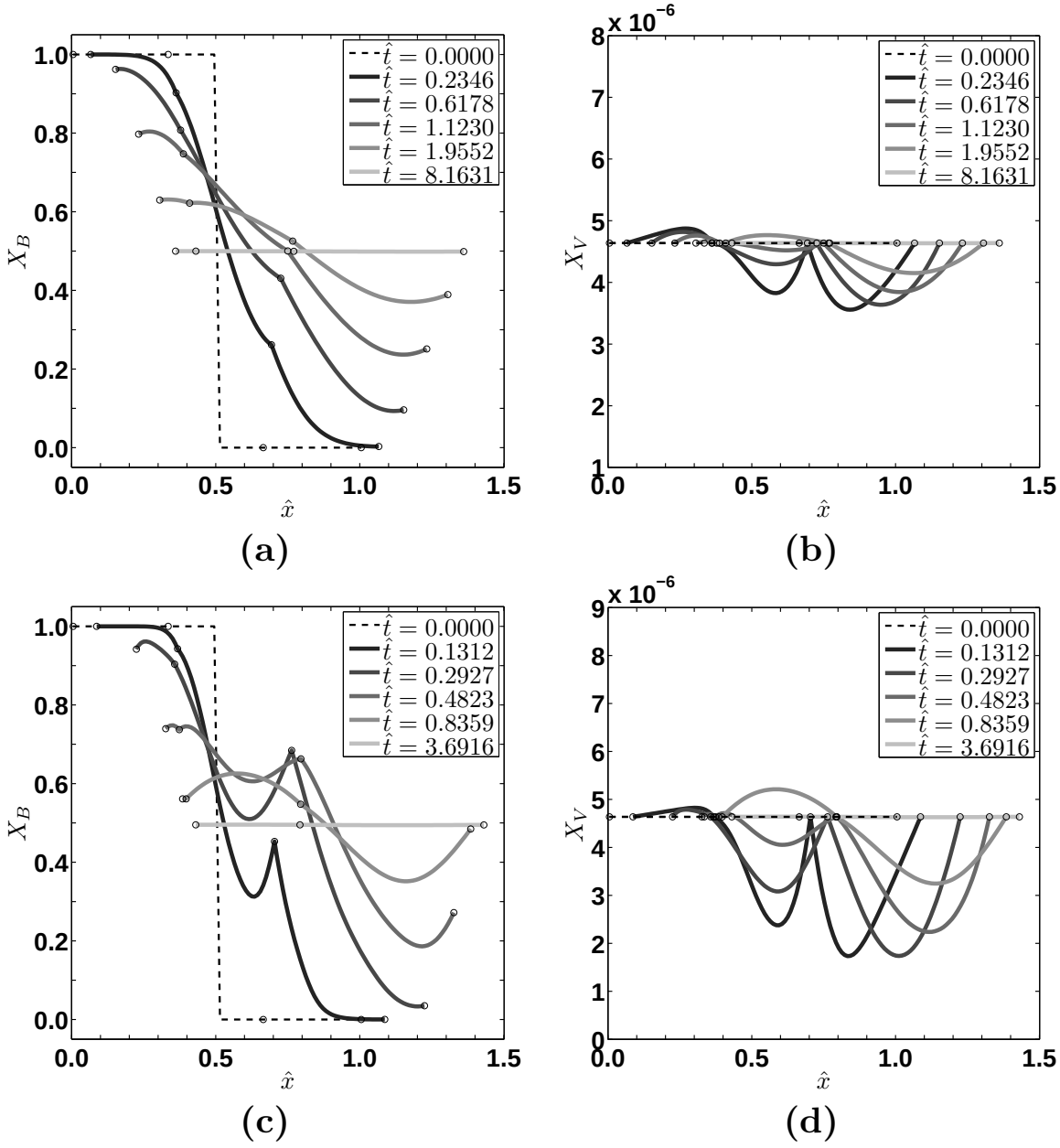

Figure 3.4: Mole fraction profiles, in a tricrystal solid with two free surfaces, of (a) B atoms and (b) vacancies for $\Gamma_B = 10\Gamma_A$; (c) B atoms and (d) vacancies for $\Gamma_B = 100\Gamma_A$. The concentration profiles at various times correspond to $\Xi = 0$, 0.2, 0.4, 0.6, 0.8, and 0.999. The circular markers denote the vacancy sources.

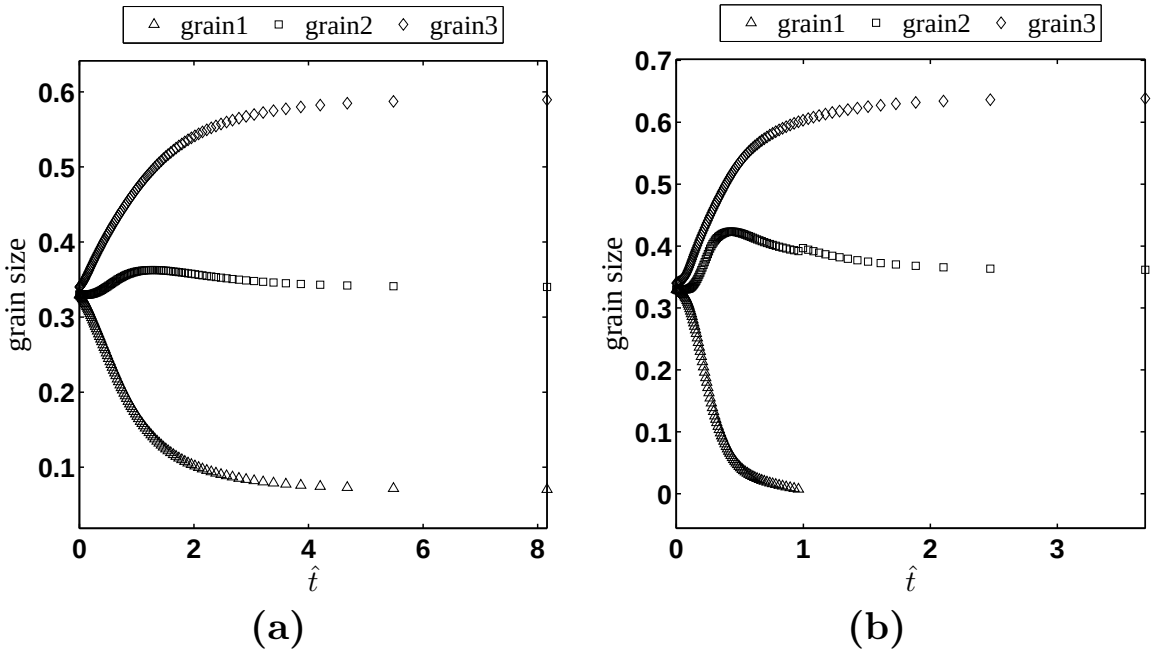

Figure 3.5: Grain size vs. time in a tricrystal solid for (a) $\Gamma_B = 10\Gamma_A$, and (b) $\Gamma_B = 100\Gamma_A$. Grain 1 is the leftmost and initially richest in B, thus rapidly decreasing in size. Grains 2 and 3 are initially the central and rightmost grains, respectively. The figures represent Kirkendall-effect-induced coarsening.

Fig. 3.4(c)]. Due to the annihilation of vacancies at both sides (the left free surface and the grain boundary between the left and central grains), the left grain shrinks. On the other hand, the right grain grows due to the incorporation of vacancies into its lattice from both ends. Figure 3.5 shows the size of each grain as a function of time. Due to the combination of contraction and expansion, the center of mass of the entire crystal shifts to the right. It is evident that the size change of each grain is dictated by the vacancy creation and annihilation at the nearest sources. This implies that each grain has a different amount of Kirkendall shift. In the $\Gamma_B = 100\Gamma_A$ case, the left grain disappears in the late stage, and the initial tricrystal reduces to a bicrystal, which provides clear evidence of grain coarsening induced by Kirkendall diffusion.

3.1.5 Case with High Vacancy Source Density

We also compare our model with the conventional treatment of substitutional diffusion by assuming that every grid point in the domain is a vacancy source. This reflects the case in which the separations between vacancy sources are sufficiently small in comparison to the vacancy diffusion length and also gives the condition that the vacancy mole fraction remains at its equilibrium value at every grid point. The mole fraction of the fast diffuser, B, is thus calculated by Eq. (3.5) at every grid point. In this case, all grid spacings change with time according to Eq. (3.6). To reduce errors caused by varying grid spacing, a higher resolution of 1001 grid points initially evenly distributed in the 1D calculation domain is used for this case. In Fig. 3.6, the mole fraction evolution is compared with that obtained from Eq. (2.21b), which was derived by the conventional treatment of substitutional diffusion within the uniform-vacancy-source approximation. The creation or elimination of extra lattice planes occurs to maintain the equilibrium value at every grid point and results in local volume changes and a global domain shift. Figure 3.6 shows that the results for the concentration distributions from our model and the conventional uniform-vacancy-source treatment are identical within numerical error after translation along the x direction. The main difference is in the choice of coordinate reference frame. The shift caused by the volume change in our model represents the Kirkendall shift of the lattice frame, while the conventional treatment is solved within the laboratory frame. In addition, there is a small difference in the dynamics between the conventional treatment and our model with sources at every grid point, which appears in the second term of Eq. (2.29).

The local fractional-length-change rates at different times are plotted in Fig. 3.7, which reflects the local vacancy generation rate and is expressed by $\dot{\varepsilon}_x = \hat{g}$ according to Eq. (2.36). The results show that the vacancy generation occurs in the A-rich region and that absorption occurs in the B-rich region. A high vacancy generation rate appears at the location where the divergence of vacancy flux has maximum in

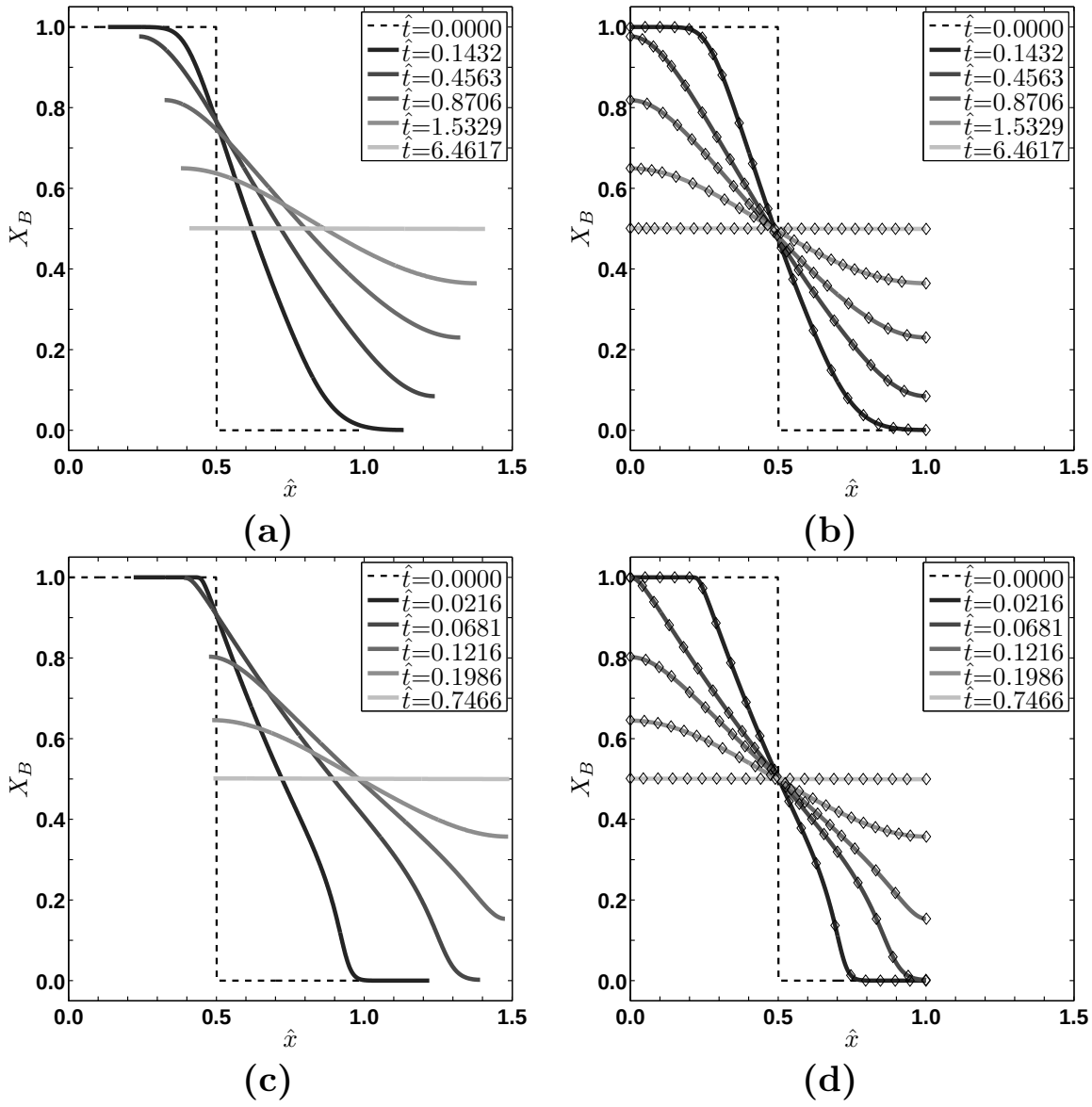

Figure 3.6: Mole fraction profiles of a solid with high vacancy source density for: (a) $\Gamma_B = 10\Gamma_A$ in the rigorous model; (b) $\Gamma_B = 10\Gamma_A$ in the conventional model; (c) $\Gamma_B = 100\Gamma_A$ in the rigorous model; (d) $\Gamma_B = 100\Gamma_A$ in the conventional model. The diamond markers in (b) and (d) are the results from the rigorous model after translating along x axis. The concentration profiles are taken at times when Ξ =0, 0.2, 0.4, 0.6, 0.8, 0.999.

the A-rich region. On the other hand, a high vacancy annihilation rate is observed at the location where the divergence of vacancy flux has its minimum. This region occurs where the second derivative of X_B has a large magnitude if the diffusivities are constant, but it may shift away from these points due to the concentration dependence of diffusivities. As diffusion proceeds, the mole fraction gradient of B decreases. Therefore, the magnitude of vacancy generation and annihilation rate decreases, and the location at the maximum rate gradually moves toward the two ends of the solid.

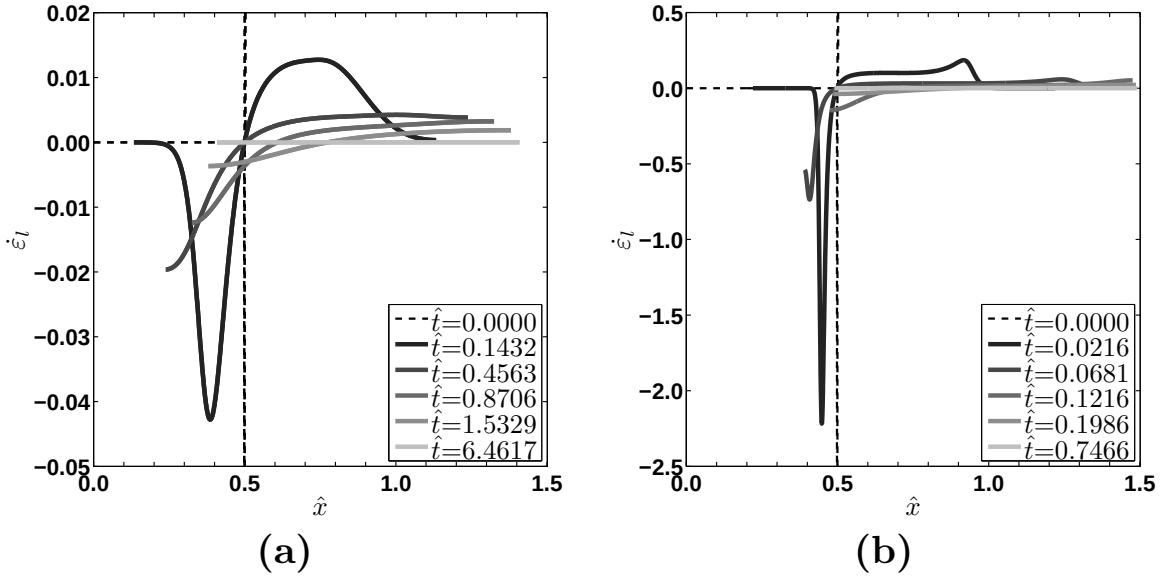

Figure 3.7: Local fractional length change rate for: (a) $\Gamma_B = 10\Gamma_A$; (b) $\Gamma_B = 100\Gamma_A$. The quantity is proportional to the local vacancy generation/elimination rate and is strongly dependent on time and position. Note the strong asymmetry in this quantity stemming from the asymmetry in diffusion-coefficient matrix.

The asymmetry of the vacancy generation rate due to composition-dependent diffusion coefficients is evident from the results in Fig. 3.7. In both $\Gamma_B = 10\Gamma_A$ and $\Gamma_B = 100\Gamma_A$ cases, the asymmetry of vacancy generation rates is qualitatively similar. The results show that vacancies are generated more uniformly in a wider region in the A-rich region but eliminated in a narrow region at a high rate in the B-rich region. This is most evident in the $\Gamma_B = 100\Gamma_A$ case, Fig. 3.7(b), where a sharper valley and a wider plateau of vacancy generation rate are observed. The vacancy

generation rate (or fractional-volume-change rate) can be related to the probability of Kirkendall void formation. A negative value of vacancy generation rate, equivalent to local volume shrinkage, indicates how fast the vacancies are eliminated at a sink in order to locally maintain the equilibrium vacancy fraction. Physically, there can be a situation when the sinks are not strong enough to annihilate vacancies at a sufficient rate. Hence, supersaturation of vacancies can occur in the regions where vacancies must be eliminated at a rapid rate, which may result in void nucleation. A consideration of void nucleation mechanism is beyond the scope of this paper and is thus ignored in our current model.

3.1.6 Conclusion for One-Dimensional Planar Simulations

In this section, we have investigated substitutional diffusion, explicitly accounting for vacancy sources and sinks. Regions between sources and sinks were treated as perfect crystals containing A atoms, B atoms, and a dilute concentration of vacancies. Diffusion within the perfect crystalline regions was described at a continuum level with realistic sets of analytically calculated diffusion coefficients for thermodynamically ideal alloy systems. The grain boundaries were modeled as ideal vacancy sources and sinks, which maintain the vacancy mole fraction at the equilibrium value.

The simulations of diffusion couples consisting of grain boundaries that act as vacancy sources and sinks indicate the existence of a Kirkendall-effect-induced coarsening phenomenon even in the absence of curvature effect on grain boundaries. During diffusion, the growth and shrinkage of perfect lattice regions between vacancy sources and sinks are specifically dependent on the vacancy generation and annihilation rate at grain boundaries. The inter-source-sink spacing decreases with time in the B-rich (fast diffuser) side and increases in the A-rich (slow diffuser) side, since the grain boundaries act as vacancy sinks in the B-rich side and as sources in the A-rich side.

The simulations also indicate that the shift of the crystal frame of reference due to

the Kirkendall effect depends on the density of vacancy sources and sinks. From the final states in Figs. 3.1, 3.2, 3.3, 3.4, and 3.6, the Kirkendall displacements increase as the vacancy source and sink density increases. The Kirkendall displacements are defined as the total shifts of the solid that have occurred when equilibrium has been established, with the reference frame taken at the center of the initial solid. The time required to reach equilibrium decreases as the vacancy source density increases. The existence of vacancy sources and sinks apparently accelerates and magnifies the Kirkendall shift by providing and eliminating vacancies that mediate the diffusion process. Conversely, the Kirkendall effect is suppressed in regions of crystal devoid of sources. The results clearly show how diffusion of vacancies as a ternary component may result in qualitative and quantitative differences in both concentration evolution and possible void formation when compared to the standard treatment of substitutional diffusion, which assumes a dense and uniform distribution of vacancy sources that allows vacancy concentration to maintain its equilibrium value throughout the solid.

The results of this work provide insight into systems subjected to strong energy input, e.g., radiation, where a significant number of Frenkel pairs are formed within the crystals that need to be annihilated at grain boundaries to maintain a local equilibrium vacancy fraction. The vacancies will diffuse toward grain boundaries through the lattice by exchanging positions mainly with the fast diffusers. In this case, depletion of the fast diffuser (or segregation of the slow diffuser) would be expected near the grain boundaries. Such a phenomenon is referred to as radiation-induced segregation. Our results suggest similar phenomena, whereby the fast diffusers are depleted near free surfaces or grain boundaries that act as vacancy sinks, indicating that the present treatment is capable of predicting inverse Kirkendall diffusion in irradiated materials.

3.2 One-Dimensional Cylindrical System

The Kirkendall void formation has recently drawn researchers' attention as a new fabrication method for nanoscale hollow objects such as nanotubes and nano hollow spheres [61, 62, 63, 64, 65, 66] from a core-shell-type diffusion couple. During diffusion, the fast diffuser diffuses to the outer regions by exchanging with vacancies. Voids form from condensation of supersaturated vacancies in the core region and then grow by consuming vacancies at the void surfaces, resulting in a hollow object. This phenomenon is not only seen at the nanoscale; a similar method was also applied to fabricate micron-size hollow alloy particles decades earlier [72]. However, void nucleation cannot be modeled by Darken's analysis, since vacancy concentration is treated to be at equilibrium value everywhere within the diffusion couple. In addition, when a void forms within a solid, the vacancy concentration on the void surface will be enhanced due to the nonzero curvature according to the Gibbs-Thomson effect. This will violate the assumption in the traditional model that vacancy concentration remains at the equilibrium value uniformly in a solid, including the void surface. Furthermore, since the motions of the lattice planes in the conventional treatment are relative to the remote ends where no diffusion occurs, the lattice motion in the laboratory frame cannot be evaluated in a solid having voids (discontinuity) where the void surface motion is unknown.

In this section, we extend our one-dimensional model to a cylindrical diffusion couple, where the fast diffuser initially occupies the core region, while the slow diffuser occupies the outer region. Free surfaces and grain boundaries are assumed to be ideal vacancy sources and sinks. On a free surface that separates the solid from its environment, the equilibrium vacancy mole fraction is given by the Gibbs-Thomson relationship:

$$X_V^{eq}(r_{surf}) = X_{V0}^{eq} \exp\left[\frac{-\Omega\gamma(\kappa_1+\kappa_2)}{k_B T}\right], \tag{3.7}$$

where r_{surf} is the radius of free surface, X_{V0}^{eq} is the equilibrium vacancy mole fraction on a flat surface, and γ is the surface free energy. The two principal curvatures of the free surfaces, κ_1 and κ_2, are given by $\kappa_1 = 1/r$ and $\kappa_2 = 0$ for a cylinder (for a sphere, $\kappa_1 = \kappa_2 = 1/r$). We assume the concentrations of vacancies and B atoms are continuous across grain boundaries and that the equilibrium vacancy mole fraction at grain boundaries is the same as that on a flat free surface. (In reality, the vacancy concentration at a grain boundary is likely lower than that at a free surface.) The fast diffuser concentration (C_B) at the vacancy sources is obtained semi-implicitly, similar to Eq. (3.5):

$$C_B(r_s, t + \Delta t) = \frac{\rho\left[1 - X_V^{eq}(r_s, t)\right]\left[C_B(r_s, t) - \nabla \cdot J_B(r_s, t)\Delta t\right]}{\rho\left[1 - X_V^{eq}(r_s, t)\right] + \nabla \cdot J_V(r_s, t)\Delta t}, \tag{3.8}$$

where r_s is the location of the vacancy sources or sinks (including free surfaces and grain boundaries). Due to the geometric symmetry, the fast diffusion path along the free surfaces and grain boundaries vanishes; i.e., diffusion takes place only along the radial direction. In addition, since our focus is to investigate the effect of vacancy sources on the Kirkendall diffusion, the grain boundary migration due to the Gibbs-Thomson effect is ignored.

This model distinguishes a solid into two different regions: the perfect lattice zone within a grain and the free surfaces or grain boundaries that act as vacancy sources. In the bulk region, the standard Fickian equations are solved to track the concentration evolution. The diffusion coefficients are analytically calculated following the procedure presented in Section 2.4 with the parameters listed in Table 3.2. For the explicit Euler scheme used in section 3.1, the time step that stabilizes both the evolutions of C_B and C_V is restricted by the maximum value of the four diffusivities (usually D_{VV}, see Fig. 2.2 for an example), which tends to be too small for examining the evolution of the fast diffuser concentration (C_B). We therefore implement an

implicit time scheme to solve the coupled diffusion equations as follows.

$$\frac{C_V^{(n+1)} - C_V^{(n)}}{\Delta t} - \chi \bar{D}_{VV}^{(n)} \nabla^2 C_V^{(n+1)} - \chi \bar{D}_{VB}^{(n)} \nabla^2 C_B^{(n+1)} = \nabla \cdot \left[\left(D_{VV}^{(n)} - \chi \bar{D}_{VV}^{(n)} \right) \nabla C_V^{(n)} \right] + \nabla \cdot \left[\left(D_{VB}^{(n)} - \chi \bar{D}_{VB}^{(n)} \right) \nabla C_B^{(n)} \right], \tag{3.9a}$$

$$\frac{C_B^{(n+1)} - C_B^{(n)}}{\Delta t} - \chi \bar{D}_{BV}^{(n)} \nabla^2 C_V^{(n+1)} - \chi \bar{D}_{BB}^{V(n)} \nabla^2 C_B^{(n+1)} = \nabla \cdot \left[\left(D_{BV}^{(n)} - \chi \bar{D}_{BV}^{(n)} \right) \nabla C_V^{(n)} \right] + \nabla \cdot \left[\left(D_{BB}^{V(n)} - \chi \bar{D}_{BB}^{V(n)} \right) \nabla C_B^{(n)} \right], \tag{3.9b}$$

where the superscript n denotes the n-th time step, $\bar{D}_{ij}$ is the mean diffusivity, and χ is a weighting factor that can be optimized to increase the numerical stability. The mean diffusivity is the average diffusivity over the diffusion couple: $\bar{D}_{ij} = \int_{\boldsymbol{r}} D_{ij}(\boldsymbol{r}) d\boldsymbol{r} / \int_{\boldsymbol{r}} d\boldsymbol{r}$. The divergence operator is given by Eq. (3.1), which in a central finite difference scheme is expressed by

$$\frac{1}{r^p} \frac{d}{dr} \left(r^p D \frac{dC}{dr} \right)_m = (p+1) \frac{r_{m+1/2}^p J_{m+1/2} - r_{m-1/2}^p J_{m-1/2}}{r_{i+1/2}^{p+1} - r_{m-1/2}^{p+1}}, \tag{3.10}$$

where m is the index of the grid points, $J_{m+1/2} = D_{m+1/2}(C_{m+1} - C_m)/(r_{m+1} - r_m)$ is the flux at the middle point between the m-th and $(m+1)$-th grid points, and $J_{m-1/2} = D_{m-1/2}(C_m - C_{m-1})/(r_m - r_{m-1})$ is the flux at the middle point between the m-th and $(m-1)$-th grid points. Equation (3.9) can be discretized to a matrix equation with a sparse matrix. Specifically, Eq. (3.9b) is used to eliminate $C_B^{(n+1)}$ in Eq. (3.9a), which can then be solved using a sparse matrix solver. Again, local volume changes due to vacancy generation and elimination at surfaces, and grain boundaries are calculated by Eqs. (2.36) and (2.39). Because the local volume change only provides the relative displacements of vacancy sources to their adjacent grains, a reference frame is necessary for describing the overall shifts of the free surfaces, the grain boundaries, and the bulk. In a cylindrical object, we take the reference point to be at the center of the cylinder, which is also the origin of the coordinate system. Under the assumption that the solid is incompressible (and conservation of volume),

the overall shift at a point is then calculated by taking all the local volume changes occurring due to the internal vacancy generation/annihilation between that point and the reference point into account. The volume changes on the external surfaces do not contribute to the shift since the volume changes simply move the surface without deforming the bulk. Thus, the radial position of an arbitrary point is updated by

$$r(t+\Delta t) = r(t) + \frac{\sum_k \Delta l_k(t) r_k^p(t)}{r^p(t)}, \tag{3.11}$$

where $\Delta l_k = v_k \Delta t$ is the local displacement resulting from vacancy injection or elimination at internal vacancy sources (grain boundaries), v_k is obtained by Eq. (2.39), and the index k denotes the k-th grain boundary. The diffusion equations can be non-dimensionalized by the same procedure as in the derivation of Eq. (3.4). The initial outer radius of the cylinder is taken to be 1 μm. The radial domain is initially discretized into 201 grid points. By solving Eq. (3.9) while updating boundary conditions, Eqs. (3.7) and (3.8), and the locations of grid points, Eq. (3.11), we determine the dynamics of the system until it reaches the state with nearly uniform distribution of concentration. Since the equations are solved in the moving grid system, explicit advection is not required.

Lattice Constant (a_l)	4.05 Å
Atomic Volume per Lattice Site (Ω)	1.661×10^{-23} cm^3
Lattice Site Density (ρ)	6.021×10^{22} cm^{-3}
Equilibrium Vacancy mole fraction (X_{V0}^{eq})	1.6×10^{-6}
Hopping Frequency of Slow diffuser (Γ_A)	9.125×10^{7} Hz
Surface Energy (γ)	1.2 J/m^2
Temperature (T)	600 K

Table 3.2: Material properties used in the computer simulations. The material properties are similar to those of Aluminum at 600 K.

3.2.1 Single-Crystal Cylinder Without an Initial Void

In the first set of simulations, we assume that the cylinder contains no initial void and that no void nucleation occurs during the diffusion process. In this case, the inner

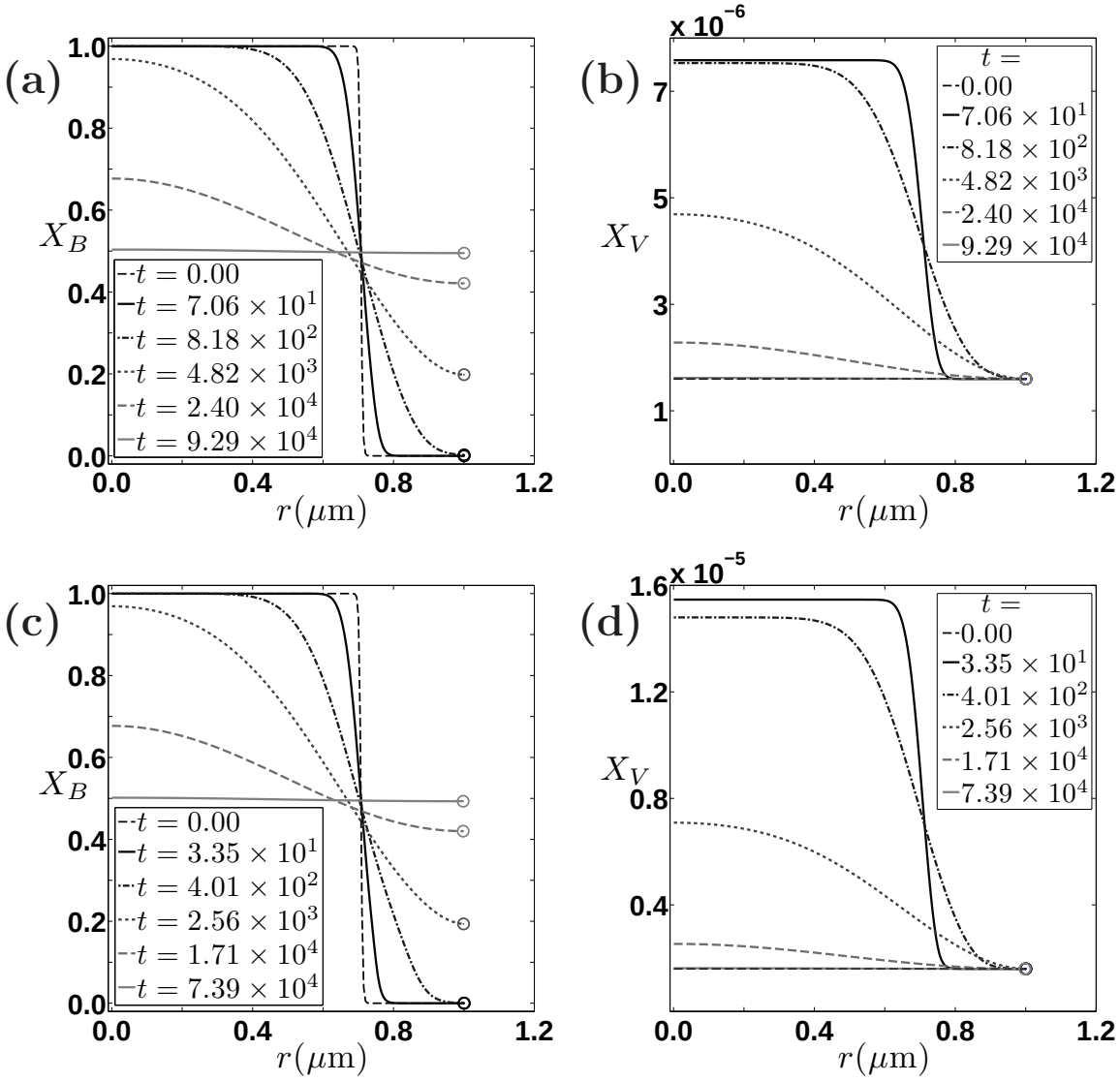

Figure 3.8: Normalized concentration profiles of (a) B atoms and (b) vacancies for $\Gamma_B = 10\Gamma_A$; (c) B atoms and (d) vacancies for $\Gamma_B = 100\Gamma_A$ in a cylindrical diffusion couple without an internal void. The curves are taken at various times (sec), corresponding to $\Xi = 0$, 0.05, 0.2, 0.5, 0.85, and 0.995. The circular markers denote free surfaces, and the time unit is sec.

boundary is fixed at $r = \epsilon$, to which a no-gradient boundary condition is applied. A very small numerical parameter, $\epsilon = 6.8 \times 10^{-4}$ is used to avoid a singularity at $r = 0$. The volume fraction of the fast diffuser, ϕ_B, is taken to be 0.5 (in this work, $\phi_B = X_B$ because the three diffusers' radii are assumed to be identical). The atomic hop frequency of the fast diffuser is assumed to be 10 and 100 times of that of the slow diffuser ($\Gamma_B = 10\Gamma_A$ and $\Gamma_B = 100\Gamma_A$). Figure 3.8 shows the evolution of the normalized concentrations of the fast diffuser and vacancies, X_B and X_V, respectively. The evolution of the vacancy concentration at the very early stage is also shown in Fig. 3.9. During the diffusion process, the fast diffuser, B, diffuses from the initially B-rich core to the initially A-rich outer region. The interdiffusion mechanism can be distinguished into two different modes. One is the intermixing diffusion mode. The other involves a nonzero net vacancy flux due to the difference in the hop frequencies of A and B, which we refer to as the unbalanced diffusion mode. In the very early stage ($\Xi < 10^{-3}$), the unbalanced diffusion mode dominates, and the outward B flux results in a compensating inward vacancy flux. Since there is no vacancy sink capable of eliminating excess vacancies in the cylinder, these inward-diffusing vacancies accumulate, diffusing up the vacancy concentration gradient, and form a plateau with nearly uniform, high vacancy concentration in the B-rich core [Figs. 3.9(a) and 3.9(b)]. During this period, the B atoms mainly exchange positions with vacancies, while the majority of the A atoms remain at their initial lattice positions: $J_B \approx -J_V$ and $J_A \approx 0$. After the vacancy concentration in the core region reaches the maximum value for the process, the vacancies begin to diffuse back to the A-rich outer region [Fig. 3.8(b) and 3.8(d)]. This phase is dominated by the intermixing diffusion mode; thus, the net vacancy flux is small ($J_V \approx 0$). The A flux is nearly equal but opposite to the B flux ($J_B \approx -J_A$) during this period. At the atomic scale, this process arises from the stochastic migration of vacancies, which through a succession of hops mediates the net exchange of A and B atoms. By comparing

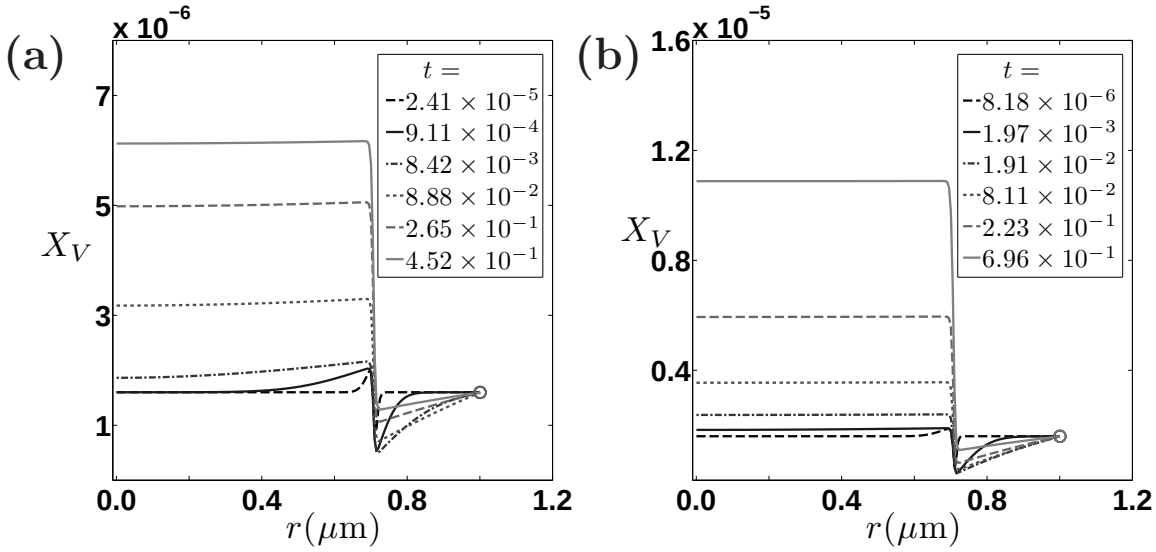

Figure 3.9: Normalized concentration profiles of vacancies at an early stage for (a) $\Gamma_B = 10\Gamma_A$; (b) $\Gamma_B = 100\Gamma_A$ in a single-crystal cylindrical diffusion couple without an internal void. The circular markers denote free surfaces, and the time unit is sec.

Fig. 3.8(a) with 3.8(c), one can observe that the time scale of evolution is nearly the same (to a factor of a few, rather than a factor of 10 as expected from the ratio of hop frequency differences) because of the general lack of vacancy sources in the diffusion couple, indicating that the Kirkendall effect is very limited in this phase and in the overall evolution of such diffusion couples. (Here, we use the term, the Kirkendall effect, in a broad sense to include nonreciprocal diffusion and all phenomena resulting from nonreciprocal diffusion.) Furthermore, although the outer free surface serves as a vacancy source during the unbalanced diffusion stage and as a vacancy sink during the intermixing stage, the overall motion of the outer free surface is nearly zero due to the lack of vacancy sink at the core of the cylinder. In addition, since this diffusion couple has only one source, the evolution of the concentrations is essentially governed by ternary substitutional diffusion in a nearly fixed frame (due to the fact that one side must remain at a fixed location). This result demonstrates the importance of a vacancy *source-sink pair* on activating the unbalanced diffusion mode that leads to the Kirkendall effect [82].

3.2.2 Void Growth in a Single-Crystal Cylinder

Dynamics of Concentration Evolution

Since we do not model nucleation of voids, we initially place a small hole at the center of the cylinder to model the evolution of a diffusion couple with an internal void. In reality, voids do not necessarily form at the center of the cylinder. However, a concentric-void configuration is commonly employed to simulate Kikrendall-effect diffusion in cylindrical objects [70, 71, 124, 125]. These models with simple geometries can provide valuable insights into the dynamics and nearly stationary states resulting from interdiffusion, and therefore we make the same assumption. At the radius of the hole, the boundary conditions corresponding to those of free surface described earlier are applied. The radius of the initial void is chosen to be 5 nm. We also set a threshold radius (r_{th}), below which a void is assumed to vanish, to be 6.85 Å (6.85×10^{-4} in dimensionless units), which is equivalent to a few atoms in the diameter. Subsequently, the boundary condition at the inner surface is changed to no-gradient. A series of simulations is performed to track the concentration evolution and the void growth during the diffusion process. Figure 3.10 shows the normalized B atom concentration and the normalized vacancy concentration for six different times. During the diffusion process, the fast diffuser (B) diffuses to the A-rich outer region mainly by exchanging with vacancies. This process reduces the vacancy concentration in the A-rich outer region while enhancing it in the B-rich core. In order to maintain the equilibrium vacancy mole fraction at the outer cylinder surface, vacancies are injected into the cylinder at the outer surface, creating new lattice sites and enlarging the outer radius of the cylinder. On the other hand, the accumulated vacancies in the B-rich core are eliminated from the void surface to maintain the equilibrium vacancy mole fraction there. This results in lattice site elimination at the void surface, and the void grows. Through the combination of the outer radius expansion and the inner radius growth, the original solid cylinder transforms into a hollow tube.

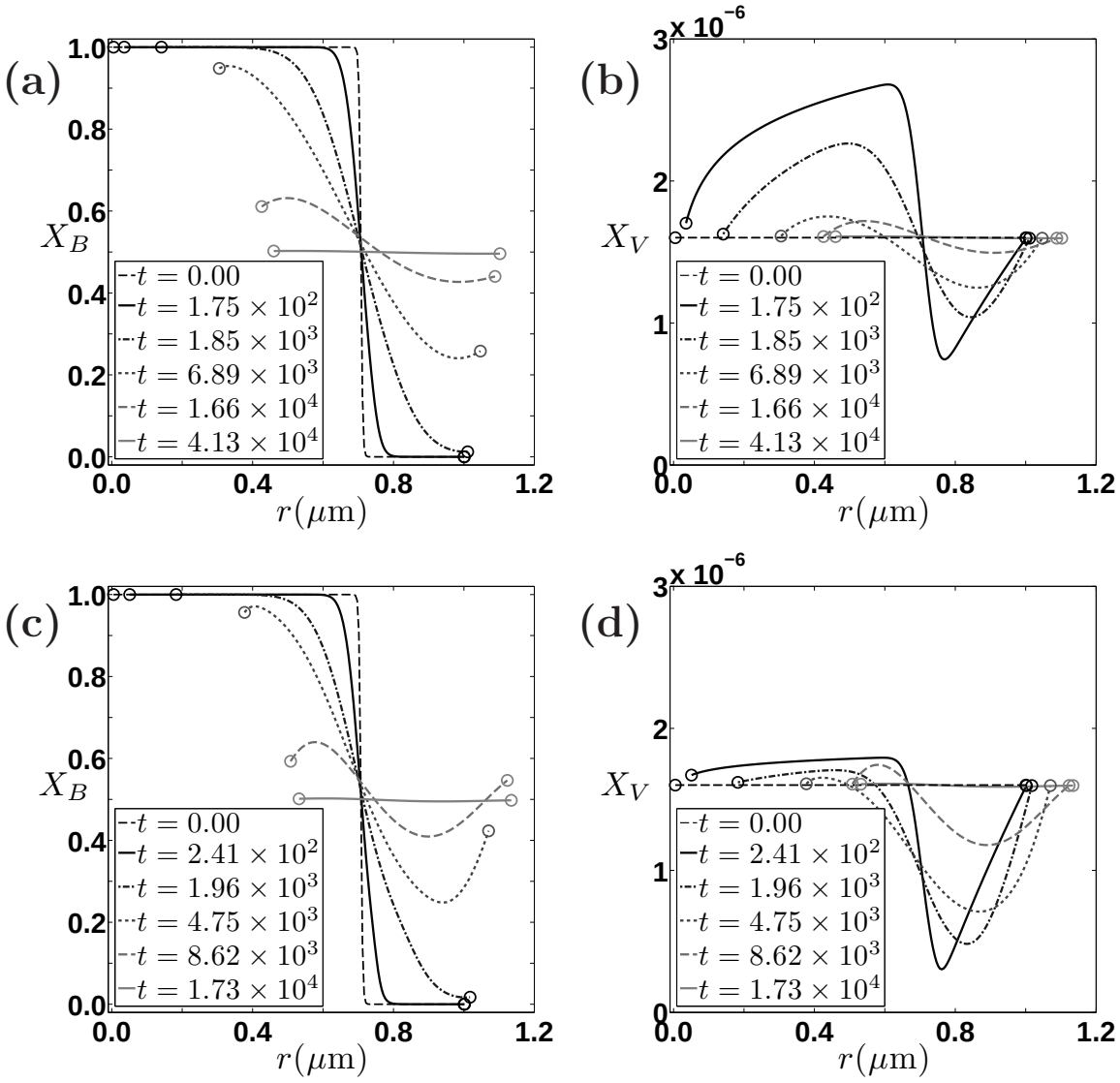

Figure 3.10: Normalized concentration profiles of (a) B atoms and (b) vacancies for $\Gamma_B = 10\Gamma_A$; (c) B atoms and (d) vacancies for $\Gamma_B = 100\Gamma_A$ in a single-crystal cylindrical diffusion couple with an initial central void having a 5-nm radius. The curves are taken at the same Ξ values as in Fig. 3.8. The circular markers denote free surfaces, and the time unit is sec.

An enhancement and a depletion of the B concentration (compared to their immediate neighborhood) at the outer and inner surfaces, respectively, are observed in the intermediate stage. This effect is more pronounced in the case where $\Gamma_B/\Gamma_A = 100$ [Fig. 3.10(c)]. When vacancies are injected at the outer surface to maintain the equilibrium vacancy mole fraction, a large substitutional B flux toward the outer surface occurs. Since B atoms cannot leave the solid, an accumulation of B atoms occurs at the outer surface in the form of uphill diffusion even though the B concentration gradient is positive there. Similarly, the vacancy elimination at the void surface gives rise to a large substitutional B flux outward, leading to depletion of B at the void surface. Fast diffuser depletion (or equivalently slow diffuser segregation) near vacancy sinks stemming from the same mechanism has been observed in irradiated materials and is referred to as the inverse Kirkendall effect [52]. The uphill diffusion near vacancy sources/sinks indicates that ternary diffusion (involving atomic and vacancy species) is essential to such phenomena because an uphill diffusion is impossible in a purely binary diffusion process.

Figures 3.10(b) and 3.10(d) illustrate the vacancy concentration evolution. As B atoms diffuse outward, vacancies diffuse inward and result in vacancy depletion and enhancement in the A-rich outer region and the B-rich core, respectively. The vacancy accumulation in the B-rich core for $\Gamma_B/\Gamma_A = 100$ is less than that for the $\Gamma_B/\Gamma_A = 10$ case, while the vacancy depletion in the A-rich outer region for $\Gamma_B/\Gamma_A = 100$ is greater than that for the $\Gamma_B/\Gamma_A = 10$ case. This difference can be understood as follows. Due to the enhanced mobility of B atoms (and thus of the vacancies exchanging with B atoms) by the higher Γ_B/Γ_A ratio, vacancy transport to the void surface is more rapid in the B-rich core. Therefore, for a high Γ_B/Γ_A ratio, the vacancy concentration takes a uniform, low concentration distribution in the core region. Meanwhile, the rapid inward vacancy flow depletes the vacancy concentration in the outer region, where the effective vacancy mobility is not enhanced. As a result, the outer-region vacancy

depletion is greater, while the inner-region vacancy enhancement is diminished.

Early Dynamics of Void Growth

When the initial central void has a radius larger than the threshold value ($r_{th} = 6.85$ Å), the void surface can serve as a vacancy source that injects or annihilates vacancies, which results in void shrinkage/growth. We examine the initial velocity (v_{in}) of the void for different initial void radii (r_{in}). The velocity and initial void radius are in the units of nm/sec and nm, respectively. Figure 3.11(a) shows v_{in}, measured at $\Xi = 10^{-5}$, as a function of r_{in} for seven values of ϕ_B with $\Gamma_B = 10\Gamma_A$. As can be seen, v_{in} is in general negative, indicating that the void initially shrinks. For a given ϕ_B value, the magnitudes of the initial velocity increase as the initial void radius decreases. This is because the vacancy mole fraction at the surface of a small void is high due to the Gibbs-Thomson effect, which causes a large outward vacancy flux at the void surface and results in void shrinkage. For a given r_{in}, the void shrinks slower as ϕ_B decreases. This is because the Kirkendall effect that results in an inward vacancy flux counteracts the Gibbs-Thomson effect when the diffusion front (where the gradient of B concentration is large) is closer to the void.

Figure 3.11(b) shows the comparison of the initial velocity of the void surface as a function of the initial void radius at $\phi_B = 0.625$ for different Γ_B/Γ_A ratios. The curves generally have the same appearance, which can be divided into two different regions: a very steep region at smaller r_{in} and a smooth asymptotic increase at the larger r_{in}. For a small r_{in}, the void shrinks very rapidly due to the Gibbs-Thomson effect before the inward vacancy flux due to the Kirkendall effect affects the vacancy injection at the inner free surface. The magnitude of the velocity is greater when the Γ_B/Γ_A ratio is large because the effective vacancy mobility is large. For a large r_{in}, the Gibbs-Thomson effect is weaker; thus, the velocity is small and can even be positive if the Kirkendall effect becomes dominant. When the Γ_B/Γ_A ratio is large, the void growth (with positive velocity) occurs faster because of the enhancement of

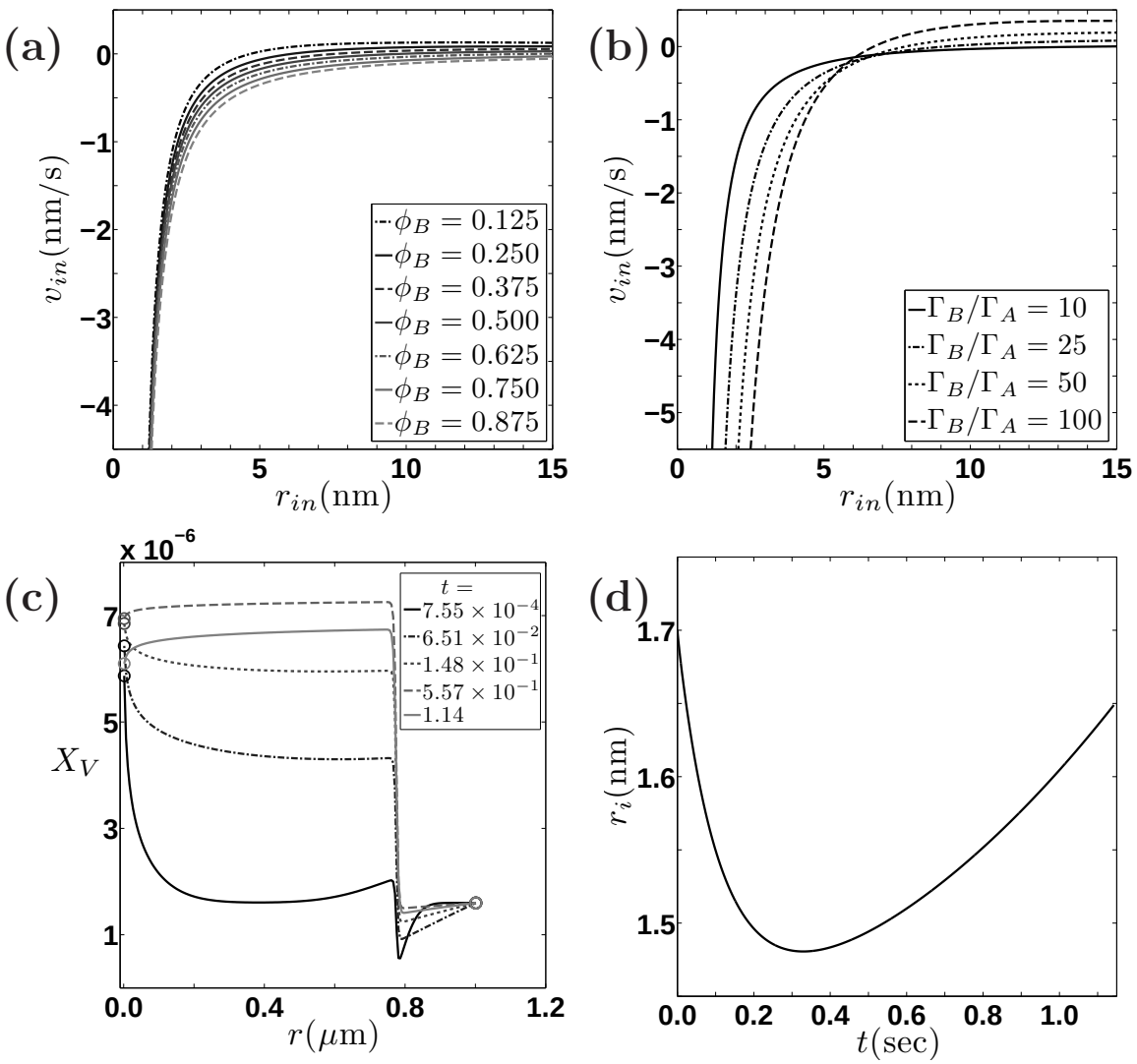

Figure 3.11: The initial velocity of the central void surface as a function of the initial void radius in a single-crystal cylindrical diffusion couple for (a) different B volume fractions at $\Gamma_B = 10\Gamma_A$ and (b) different Γ_B/Γ_A ratios with a B volume fraction of 0.5. (c) The vacancy mole fraction evolution at early stage for $\Gamma_B = 10\Gamma_A$, $\phi_B = 0.6$, and $r_{in} = 1.7$ nm. (d) The central void radius as a function of time corresponding to Fig. 3.11(c).

the Kirkendall effect.

These observations can be understood in more detail by examining the vacancy concentration evolution. Figure 3.11(c) shows the vacancy concentration evolution in the very early stage of diffusion ($\Xi \leq 10^{-6}$) for $\phi_B = 0.6$, $\Gamma_B/\Gamma_A = 10$ and $r_{in} = 1.7$ nm. In this case, the void initially shrinks due to the Gibbs-Thomson effect, but it grows when the Kirkendall effect becomes dominant. The vacancy flux at the void surface in the absence of A species in the nearby region can be determined according to the vacancy concentration gradient because $X_B + X_V = 1$. In the very early stage, the vacancy concentration profile possesses a negative gradient at the void surface, which causes vacancy injection and void shrinkage. As the diffusion process continues, the inward vacancy flux due to the Kirkendall effect leads to a vacancy accumulation in the core region, and the vacancy concentration forms a positive gradient at the void surface. At this stage, the void grows. Figure 3.11(d) illustrates the void radius as a function of time. The void shrinks until $t = 0.32$ sec and then begins to grow.

Depending on the simulation parameters, the void can either shrink then grow or shrink until it collapses. The critical initial radius, r_c, is defined as the initial radius above which a void eventually grows. Figure 3.12(a) illustrates r_c as a function of ϕ_B for $\Gamma_B/\Gamma_A = 10$. This curve can be divided into two regions: at a lower ϕ_B, r_c increases with increasing ϕ_B, and at a higher ϕ_B, it decreases with ϕ_B. In the first part, the increase is due to the larger distance between the void surface and the diffusion front, which leads to a reduced vacancy flux due to the Kirkendall effect near the void surface. In this case, the critical radius is the radius of the void at which the vacancy flux due to the Kirkendall effect exactly cancels the vacancy flux due to the Gibbs-Thomson effect. In contrast, at a higher ϕ_B, the diffusion front is sufficiently far away from the void surface such that many vacancies do not diffuse rapidly enough to reach and annihilate at the void surface. Vacancies therefore accumulate in the B-rich core region and increase the chemical potential in the region between the void

surface and the diffusion front. Since the vacancy concentration (and the chemical potential) is fixed at equilibrium at the void surface, this gives rise to a sharp positive gradient of the vacancy concentration. As a result, the void will grow, and r_c decreases as ϕ_B increases. In this case, r_c is the radius at which the Kirkendall-effect-induced vacancy chemical potential gradient nullifies that stemming from the Gibb-Thomson effect.

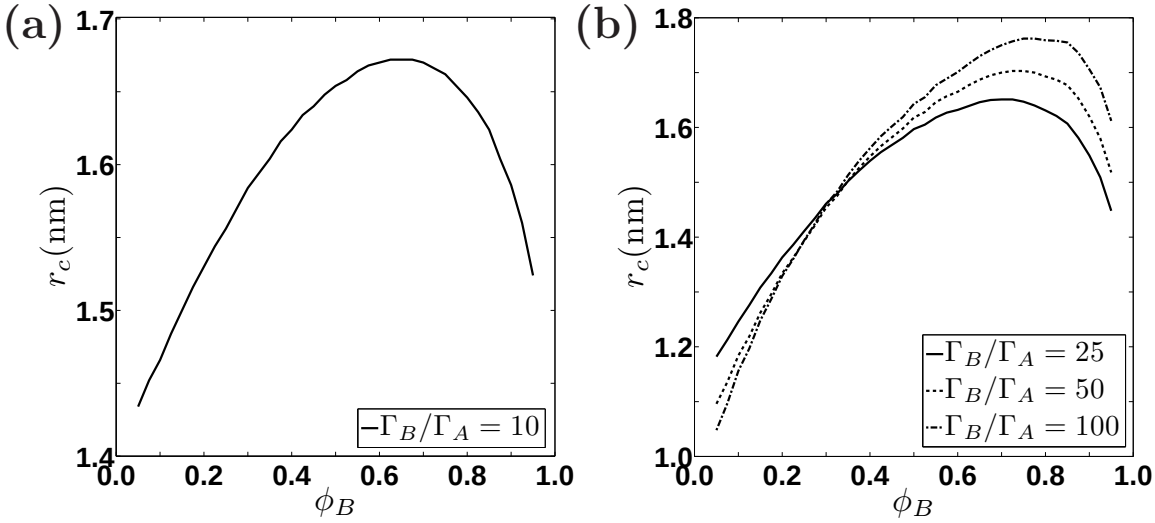

Figure 3.12: The critical initial radius of the central void in a single-crystal cylindrical diffusion couple with a 1-μm outer radius for (a) $\Gamma_B/\Gamma_A = 10$; (b) $\Gamma_B/\Gamma_A = 25$, 50, and 100.

Figure 3.12(b) shows r_c for different Γ_B/Γ_A ratios ($\Gamma_B/\Gamma_A = 25, 50$ and 100). The critical initial radius behaves similarly to the $\Gamma_B/\Gamma_A = 10$ case in Fig. 3.12(a). However, the peaks of r_c shift to the right as the hop frequency ratio increases. As mentioned previously, a higher Γ_B/Γ_A ratio results in a higher effective vacancy mobility in the B-rich region, which leads to a larger inward net vacancy flux. The enhanced inward vacancy flux will facilitate the void growth when ϕ_B is relatively low, where the vacancy fluxes due to the Kirkendall effect and the Gibbs-Thomson effect cancel directly. Thus the critical initial radius decreases with increasing Γ_B/Γ_A ratio. On the other hand, at a higher ϕ_B, where the void grows due to the chemical potential gradient caused by a vacancy accumulation in the B-rich core, the enhanced vacancy

mobility alleviates the vacancy accumulation, which reduces the positive vacancy concentration gradient. Hence, r_c increases with increasing Γ_B/Γ_A ratio.

Fully-Grown Void Radius and Elapsed Time

During the stage in which rapid outward diffusion of the fast diffuser occurs, the void and cylinder radii grow rapidly due to vacancy elimination and injection at the void surface and cylinder surface, respectively. After the atomic species reach nearly homogeneous distribution, the void starts to contract due to the Gibbs-Thomson effect at a comparatively very slow rate. This slow contraction of a void is similar to those observed from quasi-steady-state diffusion models [71, 124, 126]. Since our focus is to study void growth dynamics, the void collapse process will not be discussed in this thesis.

The fully-grown void radii before void shrinkage and the elapsed time to the fully-grown void radii are recorded for different ϕ_B and different Γ_B/Γ_A ratios during the simulations. Shown in Fig. 3.13(a) are the fully-grown void radii (r_f). The fully-grown void radius reflects the total number of vacancies injected at the outer surface, then transported to and annihilated at the void surface during the diffusion process. Since B atoms preferentially exchange with vacancies, the amount of B atoms in the system determines how many vacancies are transported from the outer surface to the void surface during the diffusion process. When ϕ_B is small, the B atoms are quickly exhausted; thus, the total number of transported vacancies is small. Similarly, when ϕ_B is large, the A atoms are quickly exhausted; thus, the total number of transported vacancies is expected to be small; this is observed in the simulation for low Γ_B/Γ_A ratios. At the intermediate values of ϕ_B, the supply of interdiffusing atoms is balanced; thus, diffusion processes involve a larger number of vacancies transported from the outer surface to the void surface, resulting in a maximum value of r_f; again, this is observed at low Γ_B/Γ_A ratios.

The above explanation only describes the behavior of diffusion couples in which

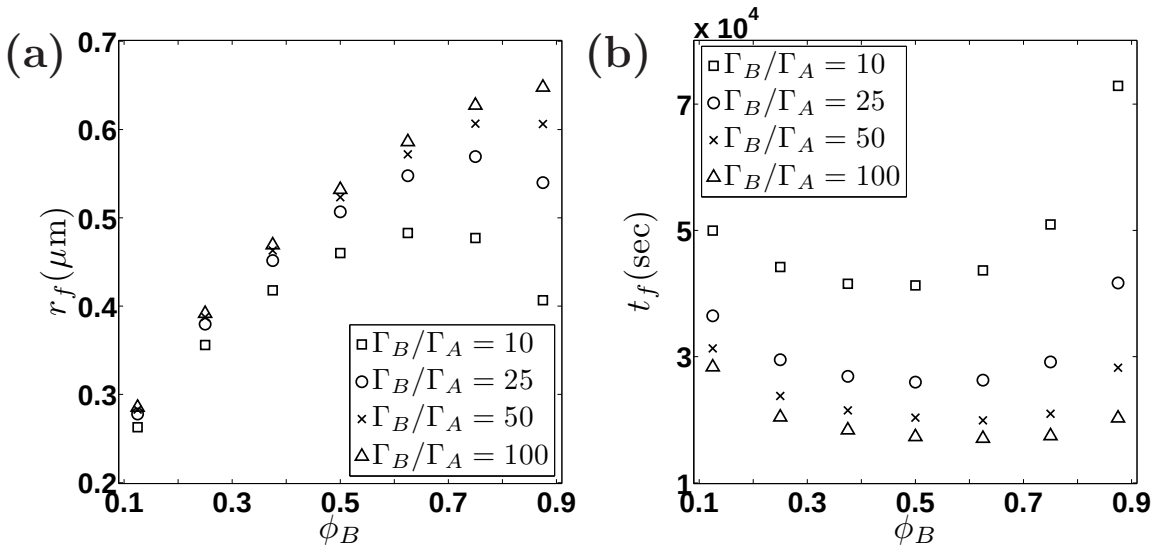

Figure 3.13: (a) The fully-grown radius of the central void in a single-crystal cylindrical diffusion couple for different B volume fractions and different Γ_B/Γ_A ratios. (b) The elapsed time to reach fully-grown void radius.

the Γ_B/Γ_A ratio is low (up to ~ 25). At large Γ_B/Γ_A ratios, the strong preference of vacancies to exchange with B atoms leads to more vacancies transported from the outer surface to the void surface without much intermixing of A and B. Therefore, more vacancies are transported per intermixing event, which leads to a larger r_f.

The elapsed time to reach fully-grown void radius, t_f, is related to how fast intermixing over the system can take place. Two aspects play a role. First is the kinetics of diffusion, which is faster when the Γ_B/Γ_A ratio is large (since B species can diffuse faster). This effect is clearly seen as the decrease in t_f with an increasing Γ_B/Γ_A ratio, see Fig. 3.13(b). This also manifests as an increase in t_f at smaller ϕ_B. The other aspect is the geometrical effect. When ϕ_B is large, the slow diffuser A must diffuse a larger distance before the equilibrium state is achieved; therefore, t_f increases.

Furthermore, the simulation results show that the increase in r_f and the decrease in t_f do not linearly scale with the Γ_B/Γ_A ratio. This is due to the fact that the diffusivities vary only by a relatively small amount at $X_B \lesssim 0.2$ regardless of Γ_B/Γ_A, see Fig. 3.14. Even though diffusivities involving B atoms and vacancies in the B-

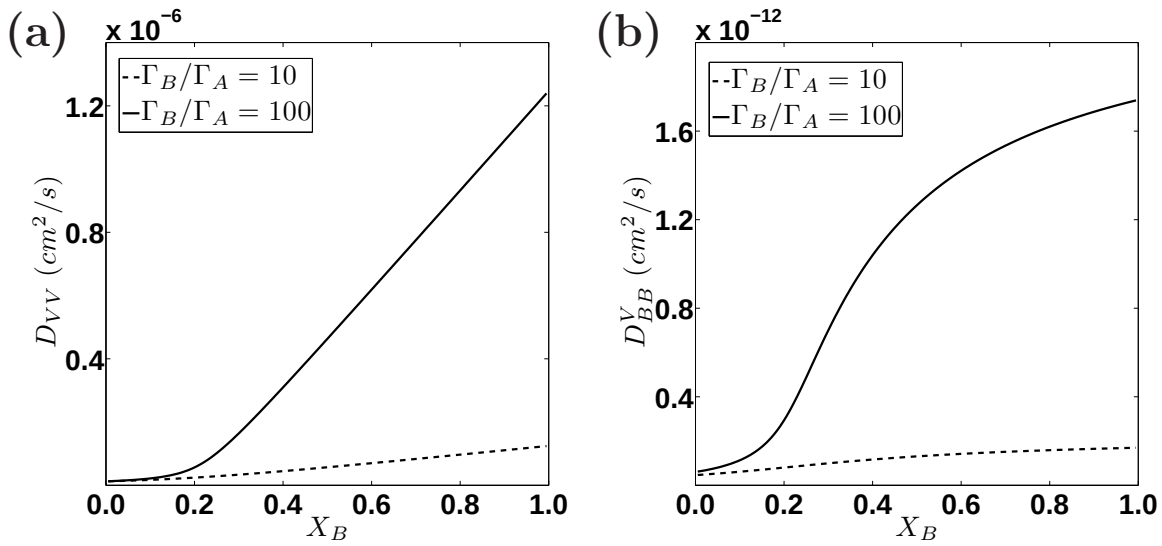

Figure 3.14: Diffusion coefficients as functions of X_B: (a) D_{VV} and (b) D^V_{BB} for $\Gamma_B/\Gamma_A = 10$ and $\Gamma_B/\Gamma_A = 100$ at $X_V = 1.6 \times 10^{-6}$.

rich region are large when Γ_B/Γ_A is large, the comparatively small diffusivities in the A-rich region through which vacancies must diffuse limit the rate of concentration evolution and vacancy transport. Therefore, the plots of r_f and t_f vs. ϕ_B approach asymptotic limits for these quantities when the Γ_B/Γ_A ratio is very large.

3.2.3 Void Growth in a Multi-Crystal Cylinder

Grain boundaries can act as internal vacancy sources/sinks and their effect on the Kirkendall-effect diffusion can be complicated due to their geometries. In this work, we assume a simple geometry to demonstrate the importance of the consideration of grain boundaries as vacancy sources/sinks in a quasi-1D cylindrical system. The grain boundaries are placed such that each grain forms a concentric layer. While diffusion along grain boundaries can be important in reality, it is not considered here because we assume cylindrical symmetry, and only diffusion in radial direction is investigated. The same set of equations is solved in this case, except for the fact that the divergence appearing in the expression for the vacancy injection rate, g, in Eq. (2.32) is treated as the jump in the flux, as discussed in Section 3.1.

Figure 3.15 illustrates the concentration evolution for a cylinder containing two [(a) and (b)] and three [(c) and (d)] initially equal-volume grains, as well as a void with an initial radius of 5 nm, for $\Gamma_B/\Gamma_A = 100$. Grain boundaries serve as sources of vacancies in A-rich regions and as sinks in B-rich regions. In the A-rich region, B atoms diffuse toward the grain boundary, and vacancies must be injected in order to supply the vacancies that exchange preferentially with B atoms. Conversely, in the B-rich region, B atoms diffuse away from the grain boundary toward the diffusion front, and vacancies diffuse in the opposite direction toward the grain boundary. Thus, the grain boundary becomes a vacancy sink. In Figs. 3.15(b) and 3.15(d), the grain boundaries supplying vacancies can be distinguished from those eliminating vacancies by examining the value of X_V. When X_V in the immediate neighborhood is less (greater) than the equilibrium value, a grain boundary acts as a source (sink).

Due to the different numbers and locations of the grain boundaries, the two-grain and three-grain cases evolve very differently. In the two-grain case, the grain boundary acts as a vacancy source because of its location, while the void surface acts as a sink; thus, they form a source-sink pair. The pair facilitates vacancy transport, which is more efficient because of the proximity of the source and the sink than the case without a grain boundary. Therefore, the fully-grown void radius is larger than that of the single-crystal case. Due to vacancy injection from the grain boundaries and the outer free surface, the volume of the outer-most grain grows as diffusion takes place. On the other hand, the volume of the innermost grain decreases because vacancies are eliminated at the void surface. This result clearly demonstrates that the Kirkendall effect can lead to grain boundary migration and grain size change when vacancy sources and sinks are explicitly discretely treated.

The evolution of the three-grain case exhibits similar growth of the outer-most grain and shrinkage of the innermost grain. However, in this case, the void collapses at a very early stage before the Kirkendall effect becomes important in the core region

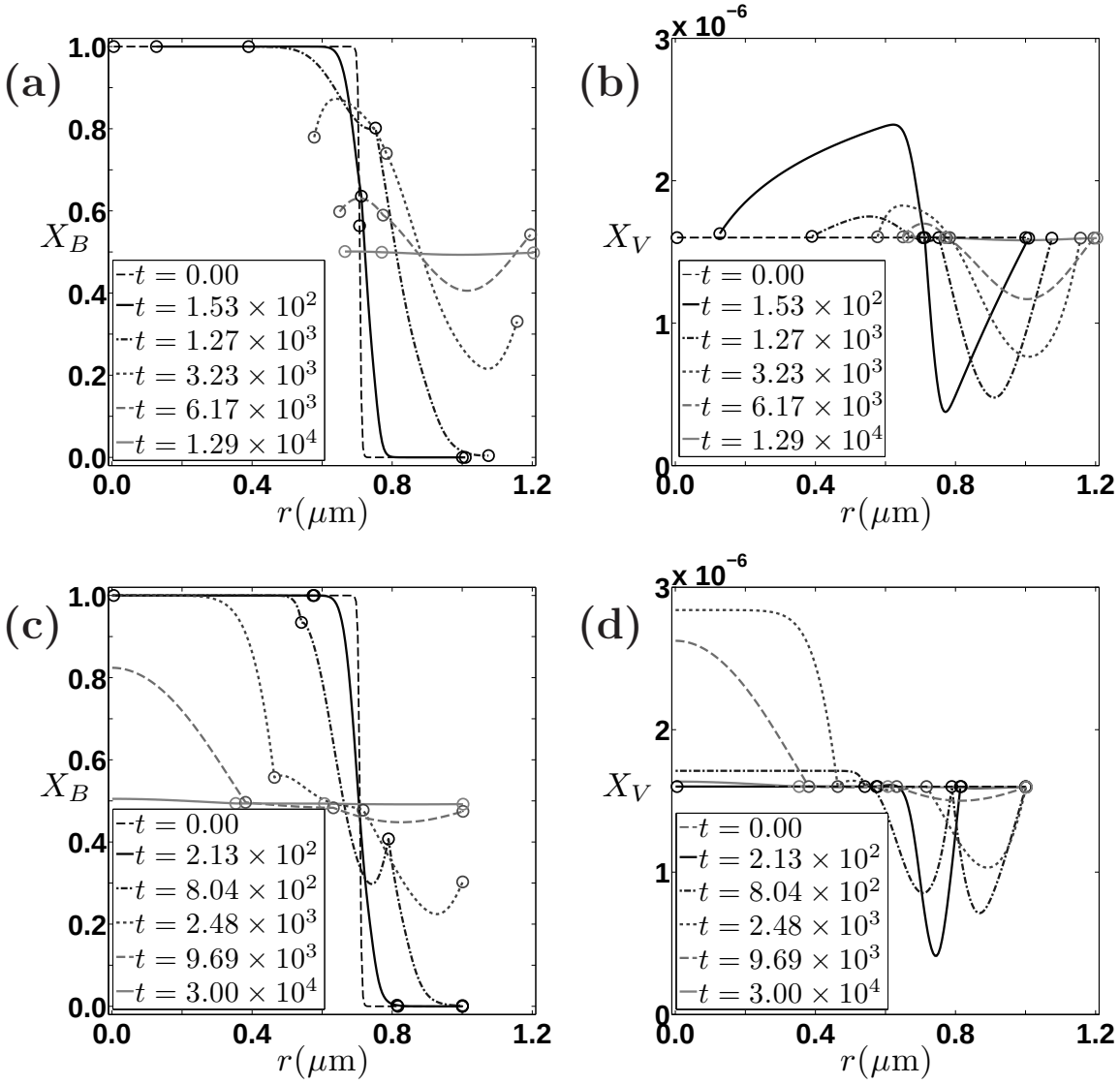

Figure 3.15: Normalized concentration profiles of (a) B atoms and (b) vacancies for $\Gamma_B = 10\Gamma_A$; (c) B atoms and (d) vacancies for $\Gamma_B = 100\Gamma_A$ in a concentric multi-crystal cylindrical diffusion couple with an initial central void with a 5-nm radius. The curves are taken at the same Ξ values as in Fig. 3.8. The circular markers denote free surfaces and grain boundaries.

because the grain boundary is located in the pure B region and the Gibbs-Thomson effect drives the diffusion of vacancies from the void surface outward. Therefore, hollow tubes are more difficult to form when many internal vacancy sources are present in the fast-diffuser-rich core region. This is consistent with the fact that Kirkendall void growth is impossible when the vacancy concentration is assumed to be at equilibrium everywhere in the bulk (i.e., Darken's approximation).

Figure 3.16(a) illustrates the fully-grown radius of the inner void for a cylindrical diffusion couple with different numbers of grain boundaries and Γ_B/Γ_A ratios. The cylinder initially contains 1, 2, 3, 4, and 5 grains of equal volume in a concentric structure and a 5-nm-radius void. The voids grow only in the one- and two-grain cases. As Γ_B/Γ_A ratio increases, r_f increases in the one- and two-grain cases. In the three-, four-, and five-grain cases, the void collapses because of the Gibbs-Thomson effect acting on the void surface in the pure B region, as described before.

The time to equilibrium, t_f, is plotted in Fig. 3.16(b). In addition to the cases where the cylinder has an initial void, the results of 1- and 2-grain cylinders without initial central voids are also plotted for comparison. In the cases of diffusion in a solid cylinder (1- and 2-grain cylinders without initial central voids and 3-, 4-, and 5-grain cylinders with collapsed voids), t_f decreases as the number of grains increases. This decrease indicates that vacancy injection and elimination by the internal vacancy sources and sinks accelerate the diffusion process. It can be noted for the multigrain cases with no initial void or with a collapsed void that the outer part of the cylinder evolves much more rapidly than the innermost grain [see, for example, Figs. 3.15(c) and 3.15(d)]. This is because the innermost grain in this case has only one source/sink, while other grains have one each at inner and outer boundaries, making a source-sink pair.

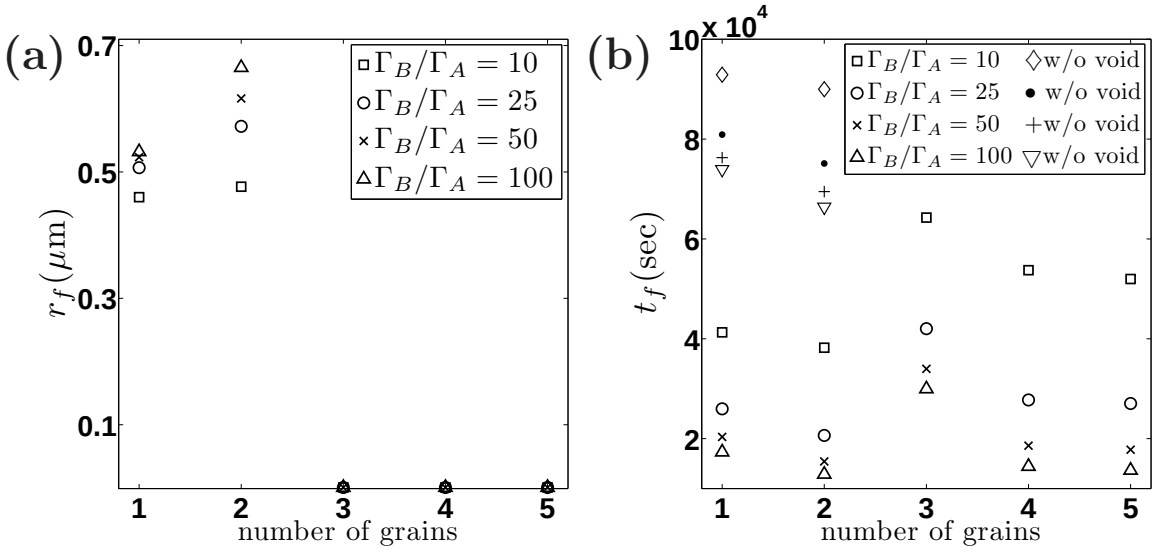

Figure 3.16: (a) The fully-grown void radius of a concentric multi-crystal cylindrical diffusion couple for different number of grains and different Γ_B/Γ_A ratios. (b) The elapsed time for voids to reach fully-grown size. For cylinders with collapsed voids, the elapsed times are taken at the state with nearly homogeneous concentration distribution.

3.2.4 Conclusion for Cylindrical Simulations

The simulations demonstrate that the inward vacancy flux caused by the preferential exchange with the outward-diffusing fast diffuser results in void growth. In the case where there are no internal vacancy sinks within the diffusion couples, the Kirkendall effect (nonreciprocal diffusion) is limited even if the hop frequency ratio between the fast and slow diffusers is large. When the vacancy supply/elimination is efficient, the unbalanced diffusion mode, in which net vacancy flux is large, is dominant. On the other hand, without sufficient vacancy supply and elimination, the intermixing mode of diffusion, where the net vacancy flux is small, dominates. The latter phenomena cannot be examined by the conventional Kirkendall diffusion model, which assumes vacancy sources to be uniformly distributed in a diffusion couple. Furthermore, based on the simulations for the polycrystalline cylindrical diffusion couples, the number of concentric grain boundaries in general accelerates the diffusion process. However, grain boundaries can also hinder void growth, depending on their locations. When

grain boundaries close to a void surface serve as vacancy sinks to eliminate vacancies diffusing from the void surface, the void shrinks. This result is consistent with the fact that void growth (the Frenkel effect) is impossible in the conventional model where the solid region surrounding a void can serve as a vacancy sink. (Note that our model converges to the Darken's model as the density of vacancy source increases.) Therefore, the results demonstrate that explicitly considering discretely distributed vacancy sources is important in predicting diffusion process and void growth dynamics when vacancy diffusion length is small compared to the typical spacing between sources.

The simulation results also reveal that the Kirkendall void formation involves two competing factors: the Kirkendall effect and the Gibbs-Thomson effect. The unbalanced diffusion caused by the different atomic hop frequencies between the fast and slow diffusers leads to a net inward vacancy flux that enlarges the void by injecting vacancies into the void, while the Gibbs-Thomson effect due to the curvature of the void surface favors the reduction of void radius by driving vacancies from the void to the solid. When the diffusion front is close to the void, the critical initial void radius is small because the net inward vacancy flux can easily access the void surface. This explains why Kirkendall voids are mostly observed near the diffusion interface on the fast-diffuser side in experiments. Moreover, due to the high vacancy mole fraction on the void surface caused by the Gibbs-Thomson effect, a negative vacancy concentration gradient is created, driving vacancies to diffuse outward. However, this vacancy concentration gradient will be balanced by the fast diffuser concentration gradient that tends to drive vacancies to diffuse inward. Thus, the void can exist nearly stably for a certain period of time (more precisely, the void shrinks at a much slower rate compared to rate of growth during the growth stage). Nonetheless, if the Gibbs-Thomson effect is sufficiently large, a void eventually collapses as the diffusion couple approaches equilibrium.

We computed the quantities such as the fully-grown void radius and the elapsed time as functions of the volume fraction of the fast diffuser for hollow cylinders forming due to the Kirkendall effect. The maximum of fully-grown void radii occurs around the intermediate volume fraction of the fast diffuser for low Γ_B/Γ_A ratios and shifts to a higher volume fraction as Γ_B/Γ_A ratio increases. The minimum of the elapsed time for a void to reach its fully-grown void size occurs around the intermediate volume fraction. As the Γ_B/Γ_A ratio increases, the fully-grown void radius increases, and the elapsed diffusion time decreases.

The present model provides a framework of studying hollow tube formation due to the Kirkendall effect. The model can be applied to systems with stoichiometric intermetallic compounds by incorporating the diffusivities of species in ordered phases obtained by either analytical derivations or Monte Carlo simulations. The model can also be extended further to simulate the process where solid-state reaction and diffusion occurs simultaneously.

CHAPTER IV

KIRKENDALL-EFFECT-INDUCED GRAIN BOUNDARY DIFFUSION

4.1 Introduction

Grain boundary diffusion is an important phenomenon that affects material behavior such as creep, sintering, precipitation at grain boundaries, and recrystallization [127]. Grain boundaries contain atomic disorder and incomplete bonding, which can lead to low migration barriers and high concentrations of diffusion-mediating defects. Hence, atomic mobility along grain boundaries is usually larger than within grains. In this chapter, we show that, in addition to potentially serving as a short-circuit diffusion path as usually accepted, a grain boundary in a substitutional solid can also substantially enhance diffusion in nearby crystalline regions by injecting or eliminating vacancies in adjacent grains through atomic mechanisms that give rise to the Kirkendall effect.

As discussed in the earlier chapters, the Kirkendall effect results from differences in the exchange rates between a vacancy and the various components of a substitutional alloy. In the presence of concentration gradients among the components of an alloy, vacancies preferentially exchange with the fast diffuser, producing a nonzero net vacancy flux. As a result, a shift of the lattice frame relative to the laboratory frame occurs in solids containing a high density of vacancy sources and sinks, giving rise to the Kirkendall effect.

Grain boundaries can act as vacancy sources and sinks inside polycrystalline solids.

During diffusion, vacancies are generated or eliminated at grain boundaries, which compensate for vacancy supersaturation and depletion. This causes local volume expansion or contraction normal to the grain boundaries. This effect was observed from the increased change in the sizes of diffusion couples, as well as larger marker shifts along the direction normal to the grain boundaries when the grain boundary density increases [116, 43]. In addition to the volume changes near grain boundaries, an enrichment of the fast diffusing species near the grain boundaries was observed experimentally, which was attributed to enhanced grain boundary diffusion [76, 36, 128, 77]. The Kirkendall effect along grain boundaries is considered to be responsible for the diffusion-induced grain boundary migration phenomenon [129, 130, 131, 132], in which a larger number of the fast diffuser atoms diffuse along or near grain boundaries than the slow counter-diffuser atoms, driving grain boundaries to migrate due to vacancy generation or elimination. As the grain boundaries migrate, intermixed regions are left behind. Furthermore, a phenomenon involving free surfaces analogous to the Kirkendall effect has also been reported in experiments [73, 74]. During diffusion, surface corrugation that initiates near the diffusion interfaces normal to the surfaces is observed. This is attributed to vacancies and dislocations that are generated (eliminated) at the surface and that migrate to (from) the bulk regions. This shows that free surfaces also act as vacancy sources and sinks for substitutional diffusion near the surface, in addition to serving as fast diffusion paths.

4.2 Model

In this chapter, we follow the model proposed in Chapter III to study diffusion near grain boundaries. We assume that grain boundaries are effective vacancy sources and sinks, and ignore the effect of dislocations. In reality, dislocations can contribute to the total vacancy generation and annihilation. As is discussed in Section 2.5, either grain boundaries or dislocations can serve as the main vacancy sources, depending on

the dislocation density and the average grain size in a polycrystalline material away from surface. Here, we assume that the dislocation density is negligible so that the bulk of a grain can be considered to have a perfect lattice structure. To isolate the effect of vacancy generation and annihilation at grain boundaries on interdiffusion, we neglect the contribution from short-circuit diffusion by assuming the atomic migration barrier along grain boundaries to be identical to that of the bulk regions. Assuming that grain boundaries serve as perfect vacancy sources and sinks, the vacancy mole fraction remains at its thermal-equilibrium value X_V^{eq} at the grain boundaries. We treat the grains as perfect binary crystals consisting of A and B atoms with a dilute concentration of vacancy V. The fluxes of A and B are then related to the gradients in concentrations according to Eq. (2.8). We restrict ourselves to a thermodynamically ideal binary random alloy for which the Gibbs free energy of the system is described by Eq. (2.43). The diffusion coefficients for this system are calculated following the procedures in Section 2.4 with the physical parameters listed in Table 3.2. As in the previous chapters, we solve Eq. (2.31) for V and B concentration evolution in the perfect lattice bulk region of a grain. At the grain boundaries, the value of C_B is updated according to Eq. (2.33), and the vacancy concentration is fixed at $C_V = \rho X_V^{eq}$, which serve as the boundary conditions for Eq. (2.31). To simplify the treatment, the local volume change due to vacancy generation and annihilation at grain boundaries is ignored. The diffusion equations can be non-dimensionalized in a similar manner as in Section 3.1. To avoid repetition, we omit the derivation here.

4.3 Numerical Methods

We employ the standard central difference scheme in space. In the grid system, each grid point is labeled with the indices x_i and y_j. The divergence of $D\nabla C$ at grid point

(x_i, y_j) is given by

$$\begin{aligned}\nabla \cdot D\nabla C\Big|_{x_i,y_j} =& \frac{D_{x_{i-1/2},y_j}(C_{x_{i-1},y_j} - C_{x_i,y_j}) + D_{x_{i+1/2},y_j}(C_{x_{i+1},y_j} - C_{x_i,y_j})}{\Delta x^2} \\ &+ \frac{D_{x_i,y_{j-1/2}}(C_{x_i,y_{j-1}} - C_{x_i,y_j}) + D_{x_i,y_{j+1/2}}(C_{x_i,y_{j+1}} - C_{x_i,y_j})}{\Delta y^2},\end{aligned} \tag{4.1}$$

where the diffusion coefficients appearing on the right-hand side are evaluated at the half points between the grid point (x_i, y_j) and its four neighboring grid points, as indicated by the subscripts containing $\pm 1/2$. The corresponding global matrix for $\nabla \cdot (D\nabla C)$ has a size of $m \times m$ and takes a band form, where m is the number of unknown concentration values to be solved for. In assembling the matrix, if a grid point has a neighboring grid point (x_i, y_{j-1}) located at the grain boundary, the value of $D_{x_i,y_{j-1/2}} C_{x_i,y_{j-1}}/\Delta y^2$ is moved to the known side of the matrix equation to form the vector containing boundary values. The same procedure will be performed for the remaining three neighboring grid points.

Since the explicit Euler time scheme is very inefficient due to the large difference in the diffusion coefficients for the vacancy diffusion (D_{VV}) and the B atom diffusion (D^V_{BB}), and the resulting vast difference between the numerically stable time step and the characteristic evolution time, we adopt the implicit time scheme presented in Eq. (3.9). The diffusion equations are discretized into a matrix equation having sparse matrices:

$$\begin{aligned}&\left(\mathbf{I} - \Delta t \bar{D}^{(n)}_{VV} \boldsymbol{\nabla}^2\right) \mathbf{C}_V^{(n+1)} - \Delta t \bar{D}^{(n)}_{VB} \boldsymbol{\nabla}^2 \mathbf{C}_B^{(n+1)} = \\ &\qquad \left[\mathbf{I} + \Delta t \, \boldsymbol{\nabla}\cdot \left(D^{(n)}_{VV} - \bar{D}^{(n)}_{VV}\right) \boldsymbol{\nabla}\right] \mathbf{C}_V^{(n)} + \Delta t \, \boldsymbol{\nabla}\cdot \left(D^{(n)}_{VB} - \bar{D}^{(n)}_{VB}\right) \boldsymbol{\nabla} \mathbf{C}_B^{(n)},\end{aligned} \tag{4.2a}$$

$$\begin{aligned}&-\Delta t \bar{D}^{(n)}_{BV} \boldsymbol{\nabla}^2 \mathbf{C}_V^{(n+1)} + \left(\mathbf{I} - \Delta t \bar{D}^{V(n)}_{BB} \boldsymbol{\nabla}^2\right) \mathbf{C}_B^{(n+1)} = \\ &\qquad \Delta t \, \boldsymbol{\nabla}\cdot \left(D^{(n)}_{BV} - \bar{D}^{(n)}_{BV}\right) \boldsymbol{\nabla} \mathbf{C}_V^{(n)} + \left[\mathbf{I} + \Delta t \, \boldsymbol{\nabla}\cdot \left(D^{V(n)}_{BB} - \bar{D}^{V(n)}_{BB}\right) \boldsymbol{\nabla}\right] \mathbf{C}_B^{(n)},\end{aligned} \tag{4.2b}$$

where the subscript n denotes the *n-th* time step, $\mathbf{C}_i^{(n)}$ is a column vector containing

m values of (known) concentration of the i species at the n-th time step, $\mathbf{C}_i^{(n+1)}$ contains m unknown values of the concentration at the $(n+1)$-th time step, Δt is the time step size, $\mathbf{I}$ is an m by m identity matrix, $\boldsymbol{\nabla}^2$ is the global matrix of a discretized Laplacian operator, and $\boldsymbol{\nabla}\cdot D\boldsymbol{\nabla}$ is the global matrix for the divergence of ∇C times the position-dependent diffusion coefficients. Equation (4.2) can be written in a short form as

$$\mathbf{A}_{11}\mathbf{C}_V^{(n+1)} - \mathbf{A}_{12}\mathbf{C}_B^{(n+1)} = \mathbf{B}_{11}\mathbf{C}_V^{(n)} + \mathbf{B}_{12}\mathbf{C}_B^{(n)} = \mathbf{f}_1^{(n)}, \tag{4.3a}$$

$$\mathbf{A}_{21}\mathbf{C}_V^{(n+1)} - \mathbf{A}_{22}\mathbf{C}_B^{(n+1)} = \mathbf{B}_{21}\mathbf{C}_V^{(n)} + \mathbf{B}_{22}\mathbf{C}_B^{(n)} = \mathbf{f}_2^{(n)}, \tag{4.3b}$$

where $\mathbf{A}$ and $\mathbf{B}$ are m by m sparse matrices and $\mathbf{f}$ is a column vector of length m, all of which can be obtained from Eq. (4.2). Equation (4.3b) can be rearranged to

$$\mathbf{C}_B^{(n+1)} = \mathbf{A}_{22}^{-1}\left(\mathbf{A}_{21}\mathbf{C}_V^{(n+1)} + \mathbf{f}_2^{(n)}\right), \tag{4.4}$$

which can then be substituted into Eq. (4.3a) to yield

$$\left(\mathbf{A}_{11} - \mathbf{A}_{12}\mathbf{A}_{22}^{-1}\mathbf{A}_{21}\right)\mathbf{C}_V^{(n+1)} = \mathbf{f}_1^{(n)} + \mathbf{A}_{12}\mathbf{A}_{22}^{-1}\mathbf{f}_2^{(n)}. \tag{4.5}$$

Equation (4.5) is solved for vacancy concentration at $(n+1)$-th time step by using a standard matrix solver. The B concentration at the $(n+1)$-th time step can then be obtained using Eq. (4.4).

4.4 Simulation

The numerical simulations are performed for a two-dimensional domain containing 100 (horizontal) $\times$ 121 (vertical) grid points. The slow diffuser A is initially placed in the left half of the diffusion couple, while the fast diffuser B initially occupies the right half. To clearly demonstrate the enhanced diffusion along a grain boundary (as compared to the bulk), one straight horizontal grain boundary is placed in the middle of the domain, which is normal to the initial diffusion front where the atomic

concentration gradient is large. The initial vacancy concentration is assumed to be at the equilibrium value throughout the domain. No-flux boundary conditions are assumed on the computational domain boundaries. The simulations are performed for three cases where the ratio between the atomic hop frequencies varies from 1 to 100 (case I: $\Gamma_B = \Gamma_A$, case II: $\Gamma_B = 10\Gamma_A$, and case III: $\Gamma_B = 100\Gamma_A$).

4.5 Concentration Evolution

Figure 4.1 illustrates the profiles of normalized concentration $\tilde{C}_B = C_B/\rho$ and $\tilde{C}_V = C_V/(\rho X_V^{eq})$ taken at time $t = 4.64 \times 10^5$ sec. The horizontal domain spans 100 μm. Figures 4.1(a) and 4.1(b) show that a grain boundary that only serves to create and annihilate vacancies does not affect diffusion in an alloy in which $\Gamma_A = \Gamma_B$. However, for an alloy in which $\Gamma_B > \Gamma_A$, Figs. 4.1(c) and 4.1(e) clearly show enhanced diffusion of B atoms along the grain boundary, as is evident from the high B concentration in the A-rich region. The enhanced diffusion is asymmetric in that much fewer A atoms have diffused toward the B-rich region. On the other hand, away from the grain boundary, the diffusion front remains straight, normal to the grain boundary and at its initial position, showing no signs of enhanced diffusion there even though B atoms have much higher hop frequency than that of the A atoms.

The vacancy concentration also behaves differently depending on Γ_B/Γ_A. For an alloy with $\Gamma_B = \Gamma_A$, since the two atomic species have equal chances to exchange with vacancies, the net vacancy flux vanishes everywhere; therefore, $\tilde{C}_V$ is unaffected by the presence of vacancy sources and sinks and remains uniform at its equilibrium value. On the other hand, for the alloys with $\Gamma_B > \Gamma_A$, $\tilde{C}_V$ only remains at the equilibrium value along the grain boundaries, where any excess or depletion of vacancies can be instantaneously accommodated [see Figs. 4.1(d) and 4.1(f)]. Away from the grain boundaries, however, $\tilde{C}_V$ is greatly depleted on the A-rich side and slightly enriched on the B-rich side. As the Γ_B/Γ_A ratio increases, the vacancy depletion in the A-rich

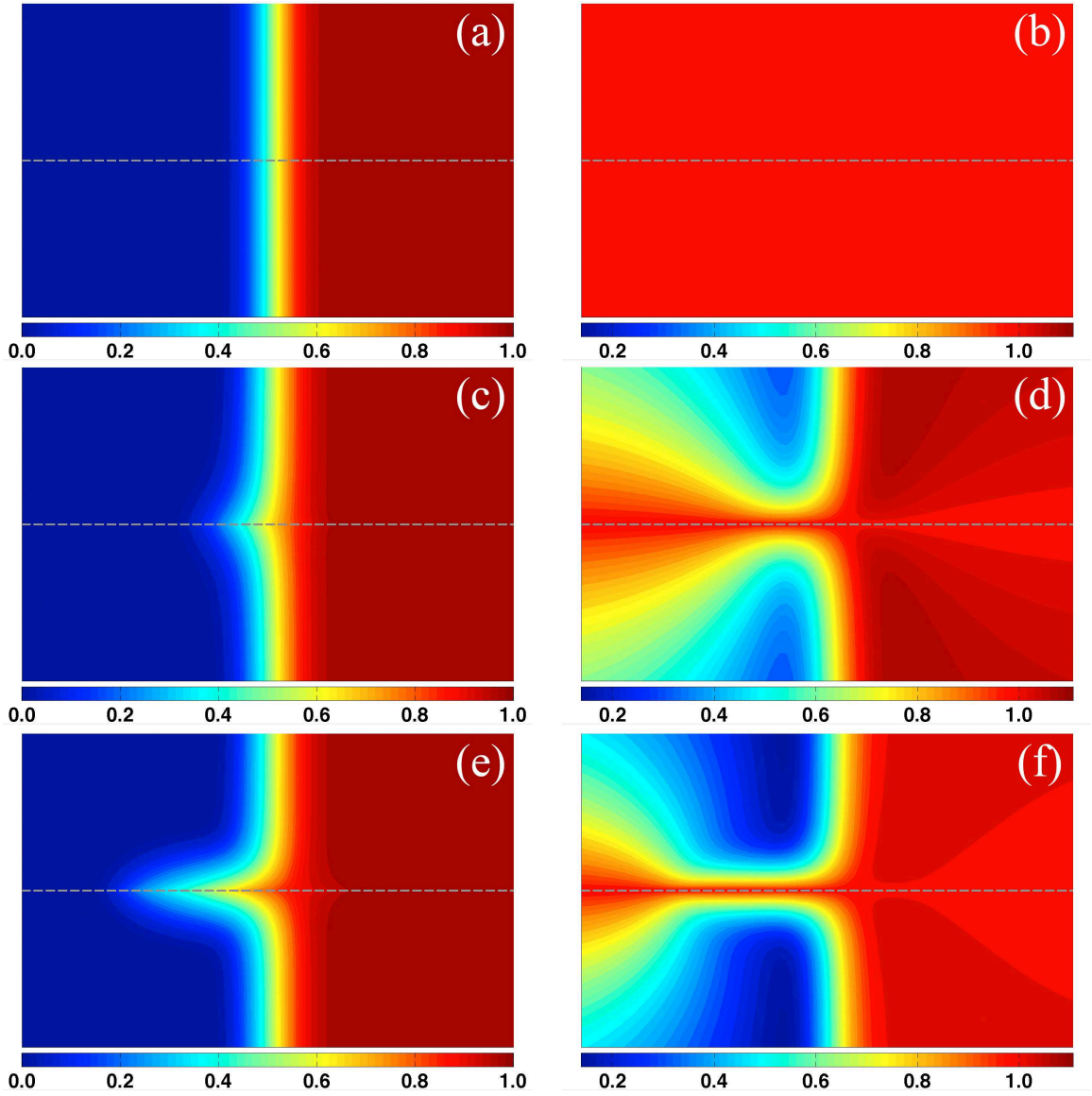

Figure 4.1: The profiles of normalized concentrations: $\tilde{C}_B = C_B/\rho$ (left column) and $\tilde{C}_V = C_V/(\rho X_V^{eq})$ (right column). Case I: (a) and (b); Case II: (c) and (d); Case III: (e) and (f). The figures are taken for the regions near grain boundaries: 80 μm (horizontal) $\times$ 50 μm (vertical).

region is enhanced, while the vacancy enrichment in the B-rich region is diminished.

4.6 Eigenvalues of the Diffusivity Matrix and Slow and Fast Modes of Diffusion

To understand the observed concentration evolution, it is useful to examine the eigenvalues of the diffusion coefficient matrix appearing in Eqs. (2.8) and (2.10) [133, 106]. The diffusion coefficients for a thermodynamically ideal substitutional binary alloy are given by

$$D_{AA} = L_{AA}\left(\frac{1}{X_A} + \frac{1}{X_V}\right) + \frac{L_{AB}}{X_V}, \tag{4.6a}$$

$$D_{AB} = \frac{L_{AA}}{X_V} + L_{AB}\left(\frac{1}{X_B} + \frac{1}{X_V}\right), \tag{4.6b}$$

$$D_{BA} = L_{AB}\left(\frac{1}{X_A} + \frac{1}{X_V}\right) + \frac{L_{BB}}{X_V}, \tag{4.6c}$$

$$D_{BB} = \frac{L_{AA}}{X_A} + L_{BB}\left(\frac{1}{X_B} + \frac{1}{X_V}\right). \tag{4.6d}$$

The eigenvalues of the diffusion coefficient matrix can be calculated according to [133, 106]

$$\lambda^{\pm} = \frac{D_{AA} + D_{BB}}{2}\left(1 \pm \sqrt{1 + 4\frac{D_{AB}D_{BA} - D_{AA}D_{BB}}{(D_{AA} + D_{BB})^2}}\right). \tag{4.7}$$

For a dilute vacancy concentration ($X_V \ll X_A$ or X_B), one can obtain the following relations:

$$D_{AA} + D_{BB} \simeq \frac{L_{AA} + 2L_{AB} + L_{BB}}{X_V}, \tag{4.8}$$

$$D_{AB}D_{BA} - D_{AA}D_{BB} \simeq -\frac{L_{AA}L_{BB} - L_{AB}^2}{X_V}\left(\frac{1}{X_A} + \frac{1}{X_B}\right). \tag{4.9}$$

By applying a Taylor expansion on the square root in Eq. (4.7), the eigenvalues are determined by

$$\lambda^{+} \simeq \frac{L_{AA} + 2L_{AB} + L_{BB}}{X_V}, \tag{4.10a}$$

$$\lambda^{-} \simeq \frac{L_{AA}L_{BB} - L_{AB}^2}{L_{AA} + 2L_{AB} + L_{BB}}\left(\frac{1}{X_A} + \frac{1}{X_B}\right). \tag{4.10b}$$

By substituting the kinetic transport coefficients given in Eq. (2.40) into these equations, one finds that λ^+ is independent of X_V, while λ^- is linearly proportional to X_V at this limit [106]. As shown below, for a perfect substitutional binary alloy having a dilute vacancy concentration, the larger eigenvalue λ^+ can be interpreted as a vacancy diffusion coefficient, while the smaller eigenvalue λ^- pertains to the intermixing diffusion mode in the absence of lattice frame shift [133], which should be distinguished from the interdiffusion coefficient defined in the presence of abundant vacancy sources and sinks to maintain an equilibrium vacancy concentration in the bulk. The significances of the two eigenvalues can be easily illustrated as follows. By using the Gibbs-Duhem relation, $\nabla\mu_V = -(X_A\nabla\mu_A + X_B\nabla\mu_B)/X_V$, the generalized flux equations, Eq. (2.5), can be rewritten as

$$J_A = -\frac{L_{AA}X_V + L_{AA}X_A + L_{AB}X_A}{X_V}\nabla\mu_A - \frac{L_{AA}X_B + L_{AB}X_V + L_{AB}X_B}{X_V}\nabla\mu_B, \tag{4.11a}$$

$$J_B = -\frac{L_{AB}X_V + L_{AB}X_A + L_{BB}X_A}{X_V}\nabla\mu_A - \frac{L_{AB}X_B + L_{BB}X_V + L_{BB}X_B}{X_V}\nabla\mu_B. \tag{4.11b}$$

In the dilute vacancy concentration limit, these equations are approximated to be

$$J_A \cong -\frac{L_{AA}X_A + L_{AB}X_A}{X_V}\nabla\mu_A - \frac{L_{AA}X_B + L_{AB}X_B}{X_V}\nabla\mu_B, \tag{4.12a}$$

$$J_B \cong -\frac{L_{AB}X_A + L_{BB}X_A}{X_V}\nabla\mu_A - \frac{L_{AB}X_B + L_{BB}X_B}{X_V}\nabla\mu_B, \tag{4.12b}$$

where $X_A\nabla\mu_A = \nabla C_A$ and $X_B\nabla\mu_B = \nabla C_B$ for an ideal random alloy. Thus, one can obtain the vacancy flux expression for a perfect lattice region where $J_A + J_B + J_V = 0$ and $\nabla C_A + \nabla C_B + \nabla C_V = 0$:

$$J_V \simeq \frac{L_{AA} + 2L_{AB} + L_{BB}}{X_V}(\nabla C_A + \nabla C_B) = -\lambda^+\nabla C_V. \tag{4.13}$$

The larger eigenvalue λ^+, therefore, characterizes one diffusion mode that homogenizes the fluctuation of the mass density (which equals the sum of the concentration

of the atomic species) in a perfect lattice solid. On the other hand, in a perfect crystal without vacancy sources and sinks, the vacancy concentration will deviate from its equilibrium value due to the different exchange rates with the two atomic species during diffusion. This results in a vacancy concentration gradient and thus a chemical potential gradient that hinders further vacancy diffusion. In the limit where vacancy diffusion finally freezes, $J_A + J_B = 0$, the driving force for vacancy diffusion can be obtained by using Eq. (2.5):

$$\nabla\mu_V = -\frac{L_{AA}\nabla\mu_A + L_{AB}\nabla\mu_B + L_{AB}\nabla\mu_A + L_{BB}\nabla\mu_B}{L_{AA} + 2L_{AB} + L_{BB}}. \tag{4.14}$$

With the approximation that $\nabla C_A \simeq -\nabla C_B$, the generalized flux equations for an ideal substitutional binary alloy in the absence of vacancy flux can be reformulated as

$$J_A \cong -\frac{L_{AA}L_{BB} - L_{AB}^2}{L_{AA} + 2L_{AB} + L_{BB}}\left(\frac{1}{X_A} + \frac{1}{X_B}\right)\nabla C_A = -\lambda^-\nabla C_A, \tag{4.15a}$$

$$J_B \cong -\frac{L_{AA}L_{BB} - L_{AB}^2}{L_{AA} + 2L_{AB} + L_{BB}}\left(\frac{1}{X_A} + \frac{1}{X_B}\right)\nabla C_B = -\lambda^-\nabla C_B. \tag{4.15b}$$

Therefore, the smaller eigenvalue λ^- characterizes the homogenization of the concentration fluctuation of the atomic diffusing species in the absence of mass density fluctuation. The significance of the smaller eigenvalue is analogous to the so-called Nernst-Planck diffusion coefficient in an ionic diffusion system [134], the slow-mode diffusion coefficient in an amorphous system [135], and the Nazarov-Gurov diffusion coefficient [136] in simple binary alloys in which the correlating terms (L_{AB}) can be ignored.

4.7 Behavior of λ^+ and λ^-

Figures 4.2(a) and 4.2(b) show the two analytically calculated eigenvalues for a constant vacancy mole fraction, $X_V = 1.6\times10^{-6}$, for different Γ_B/Γ_A ratios (similar plots can be found in Ref. [106]). When $\Gamma_B > \Gamma_A$, the larger eigenvalue, λ^+, increases lin-

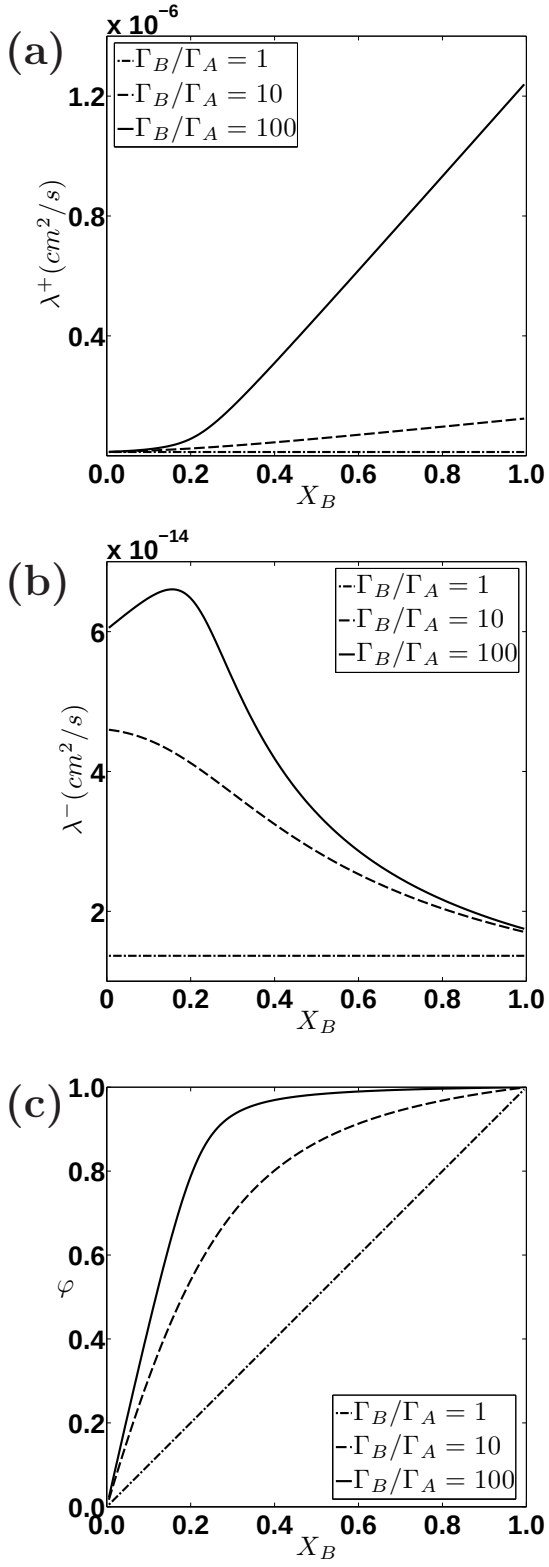

Figure 4.2: (a) The larger eigenvalues, (b) The smaller eigenvalues, and (c) the partition parameter φ (as defined in Ref. [106]) as functions of X_B for $X_V = 1.6 \times 10^{-6}$, and different Γ_B/Γ_A ratios.

early as X_B increases in the region $X_B \geq 0.25$. The slopes above the percolation limit ($X_B = 0.25$) scale well with the fast-to-slow atomic hop frequency ratio, reflecting that vacancies are more likely to exchange with the fast diffuser when more B atoms are available. However, the smaller eigenvalue, λ^-, decreases as X_B increases when $X_B \geq 0.25$. This shows that the intermixing between the two atomic species is more difficult when vacancies tend to only exchange with B atoms. Furthermore, it is noteworthy that the diffusivity associated with the intermixing process, λ^-, only increases by a factor of a few even when Γ_B/Γ_A increases by two orders of magnitude. This implies that the diffusion process under slow-mode diffusion (and thus intermixing) will also be enhanced by the increase in the fast-to-slow atomic hop frequency ratio, but not as notably as the fast-mode diffusion process that mainly involves the fast diffuser and vacancies.

The spatial variation of λ^+ and λ^- scaled with $D_0 = 7.48 \times 10^{-8}$ cm^{2}s^{-1} for the concentration profiles of Fig. 4.1 is illustrated in Fig. 4.3. As shown in Figs. 4.3(c) and 4.3(e), λ^+ in the B-rich regions is much larger than that in the A-rich regions. The vacancy diffusion coefficient in the B-rich regions is about Γ_B/Γ_A times larger than that in the A-rich regions, reflecting the difference in exchange rates with the two atomic diffusing species. Furthermore, there is an enhancement of λ^+ along the grain boundaries near the diffusion front on the initially A-rich side due to an increase in the concentration of B atoms there. This variation in λ^+ allows us to explain the vacancy concentration profiles in Figs. 4.1(d) and 4.1(f). Diffusion taking place away from the grain boundary near the diffusion front causes a vacancy depletion in the A-rich region next to the interdiffusion zone and a vacancy accumulation in the B-rich region because vacancies preferentially exchange with the more mobile B atoms. This deviation from the equilibrium vacancy concentration is rapidly alleviated by the grain boundary in the B-rich regions, where the vacancy diffusivity, λ^+, is large. However, the vacancy concentration is near equilibrium only very close to the grain

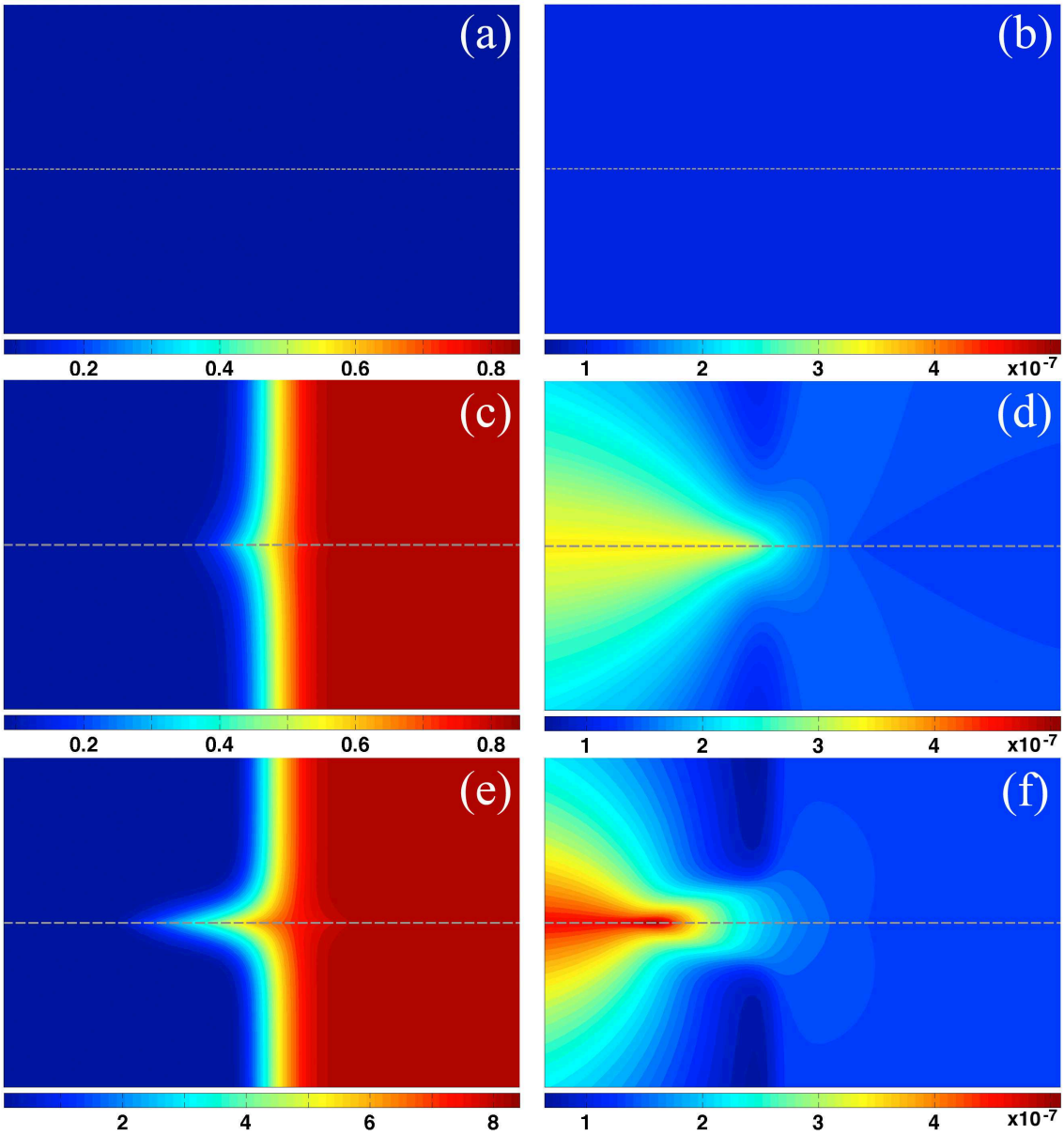

Figure 4.3: The profiles of λ^+ (left column) and λ^- (right column) scaled with $D_0 = 1.497 \times 10^{-7}$ cm^2/sec. Case I: (a) and (b); Case II: (c) and (d); Case III: (e) and (f). The figures are taken for the same regions as in Fig. 4.1.

boundary in the A-rich region because λ^+ is small in most of the A-rich region except along the grain boundary. As a result, the enrichment and depletion of vacancy concentration are asymmetric on the two sides of the diffusion couple. This effect is more pronounced in Fig. 4.1(f), since λ^+ in the B-rich region is about Γ_B/Γ_A times larger than that in the A-rich region.

4.8 The Estimate of Kirkendall-Effect-Enhanced Grain Boundary Diffusion

In this section, we make an estimate of the degree of enhancement of diffusion along grain boundaries attributed to the Kirkendall effect. Since the vacancy concentration gradient vanishes along grain boundaries, the chemical potential of the vacancies becomes constant along grain boundaries: $\partial\mu_V/\partial x|_{gb} = 0$, where the subscript 'gb' denotes quantities along grain boundaries. Thus, the driving forces for diffusion of A and B atoms are related to each other by the Gibbs-Duhem relation: $X_A\partial\mu_A/\partial x|_{gb} + X_B\partial\mu_B/\partial x|_{gb} = 0$. For thermodynamically ideal alloys under these conditions, it can be shown analytically that the ratio of J_B to $-J_A$ along grain boundaries equals the ratio of Γ_B to Γ_A by substituting the Gibbs-Duhem relation and the expressions of kinetic transport coefficients into Eq. (2.22):

$$\left.\frac{J_B}{J_A}\right|_{gb} = -\frac{X_A L_{BB} - X_B L_{AB}}{X_B L_{AA} - X_A L_{AB}} = -\frac{X_V X_A X_B \Gamma_B(\Lambda - 2X_A\Gamma_B - 2X_B\Gamma_A)}{X_V X_B X_A \Gamma_A(\Lambda - 2X_B\Gamma_A - 2X_A\Gamma_B)} = -\frac{\Gamma_B}{\Gamma_A}. \tag{4.16}$$

Thus, since J_B represents the fast-mode diffusion flux while J_A represents the intermixing flux, the magnitude of the enhancement of grain boundary diffusion due to the Kirkendall effect is given by the fast-to-slow ratio of the hop frequencies. This result indicates that interdiffusion of the two atomic species along grain boundaries that act as perfect vacancy sources and sinks follows the fast-mode diffusion that is equivalent to the Darken's type of interdiffusion. In contrast, far away from grain boundaries, the vacancy flux is small, and interdiffusion follows the slow-mode of diffusion. Thus,

the Kirkendall effect is weak even though the two atomic diffusing species have very different hop frequencies. The results clearly show that interdiffusion shifts from the fast-mode diffusion to the slow-mode diffusion as the distance from vacancy sources and sinks increases. While the simulation results presented here pertain to the very early stages of interdiffusion when local swelling or contraction at the grain boundary is still negligible, the qualitative conclusions are expected to hold for long times as well.

4.9 The Intermixing Flux and the Partition Parameter

While the two eigenvalues describe vacancy diffusion and the slow-mode intermixing diffusion in the perfect lattice regions, it is useful to analyze the diffusional fluxes using the parameter introduced by Van der Ven [106]:

$$\varphi = \frac{D_{BA}}{D_{AB} + D_{BA}}, \tag{4.17}$$

which can be interpreted as the fraction of vacancy flux exchanging with the fast diffuser. Here, we term this parameter as the partition parameter, where partition refers to that between the fast and slow modes. This interpretation is strictly true only for thermodynamically ideal alloys at the dilute vacancy concentration limit, as shown below. Since the flux of one atomic diffusing species consists of two parts, flux exchanging with vacancies and intermixing flux, the intermixing flux is determined by subtracting the fraction exchanging with vacancies from the atomic flux:

$$\breve{J}_A = J_A + (1-\varphi)J_V = \varphi J_A - (1-\varphi)J_B, \tag{4.18a}$$

$$\breve{J}_B = J_B + \varphi J_V = -\varphi J_A + (1-\varphi)J_B, \tag{4.18b}$$

where $\breve{J}_A = -\breve{J}_B$. By substituting Eq. (2.8) into (4.18) for flux expressions and using Eq. (4.6) for diffusion coefficients, the intermixing fluxes in a dilute vacancy

concentration are obtained by

$$\breve{J}_A = -\breve{J}_B \cong -\frac{L_{AA}L_{BB} - L_{AB}^2}{L_{AA} + 2L_{AB} + L_{BB}} \left(\frac{1}{X_A} + \frac{1}{X_B} \right) \nabla C_A = -\lambda^- \nabla C_A. \tag{4.19}$$

This equation is equivalent to Eq. (4.15) that indicates the intermixing flux when $J_V = 0$. This result clearly shows that the atomic flux subtracting the fraction exchanging with vacancies is the intermixing flux and that φ is the fraction of vacancy flux exchanging with the fast diffuser. Figure 4.2(c) shows φ as a function of X_B for different Γ_B/Γ_A ratios. When $\Gamma_B = \Gamma_A$, φ is a linear combination of the components. Once the two atomic hop frequencies deviate from each other ($\Gamma_B > \Gamma_A$), φ increases and has a more uniform distribution in the region $X_B > 0.25$, above which vacancies and B atoms frequently exchange back and forth.

Shown in Fig. 4.4 are the fluxes of A and B atoms and vacancies, corresponding to Figs. 4.1(e) and 4.1(f), case III. Away from the diffusion interface, vacancy flux is compensated by A flux on the A-rich side because almost no B atoms are there [Fig. 4.4(b)]. It shows that no intermixing process takes place away from the diffusion interface in the A-rich region during diffusion. This is consistent with $\breve{J}_A = J_A + (1 - \varphi)J_V = 0$ in the A-rich region outside the rapid diffusion zone, where $\varphi \approx 0$ and the vacancy flux is given by $J_V = -\lambda^+ \nabla C_V$. The flux J_A compensated by J_V in the A-rich region will not contribute to the homogenization of the concentration of atomic species. Instead, it only results in a shift of atoms without varying their concentration. Similarly, vacancy flux only exchanges with B flux on the B-rich side [Fig. 4.4(d)] away from the diffusion interface, and diffusion only leads to a shift of B atoms without varying B concentration.

On the other hand, near the diffusion interface but away from the grain boundary, vacancy flux vanishes [Fig. 4.4(e)], and the fluxes of A and B atoms are nearly equal in magnitude but opposite in direction. It shows that diffusion in the rapid diffusion zone (near the diffusion interface) away from vacancy sources and sinks takes place

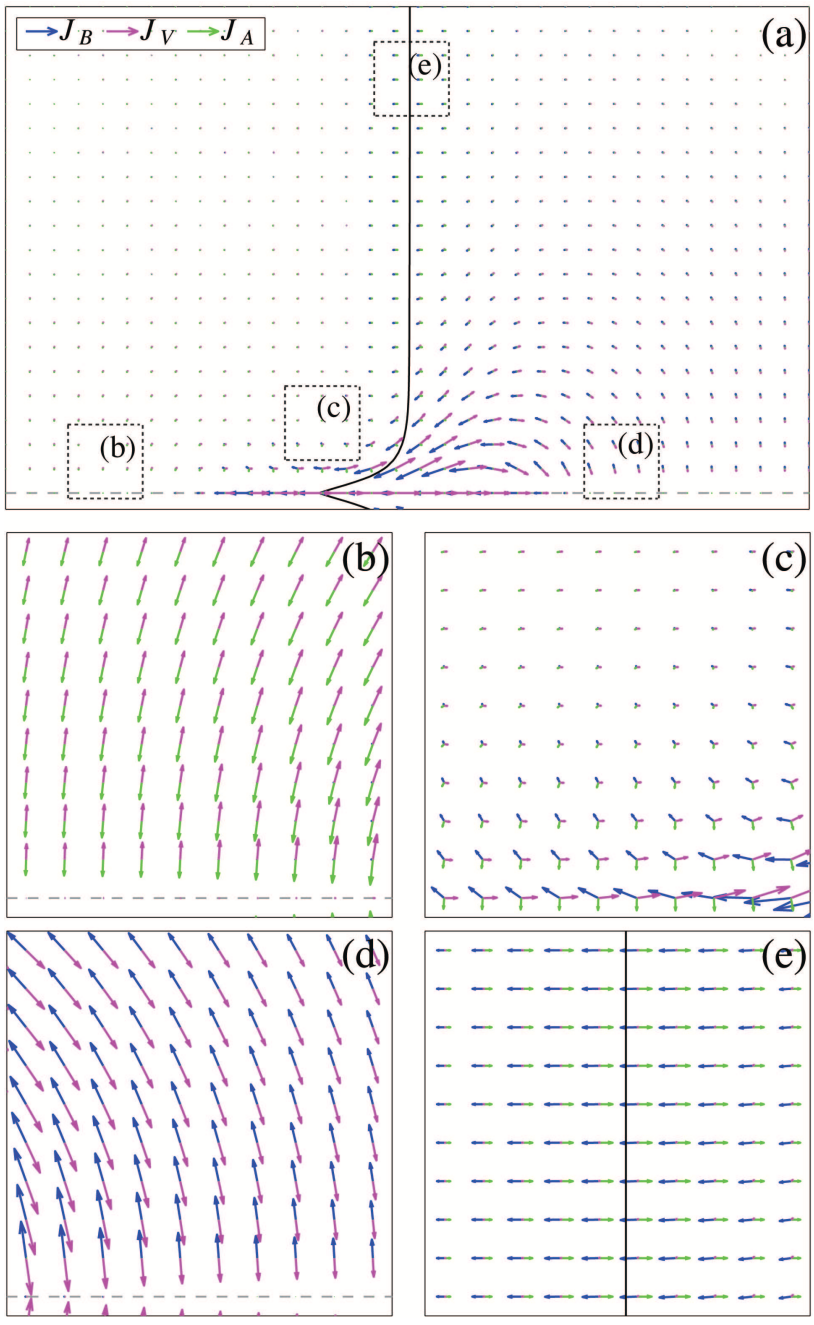

Figure 4.4: The diffusion fluxes corresponding to the concentration profiles of Figs. 4.1(e) and 4.1(f). Figures (b), (c), (d) and (e) are the magnified regions in (a) as indicated by the boxes.

via a complete intermixing process that well follows the slow-mode diffusion because the vacancy concentration gradient suppresses the difference in the exchange rates with the two atomic species. Since λ^- does not vary much with different Γ_B/Γ_A ratios, as illustrated in Fig. 4.2(b), diffusion of the atomic species in the diffusion zone away from grain boundaries occurs via a similarly slow process in the cases where Γ_B/Γ_A varies from 1 to 100 [Figs. 4.1(a), 4.1(c) and 4.1(e)]. These results demonstrate that diffusion process in the perfect lattice region of a substitutional crystalline solid consists of two modes characterized by the two eigenvalues of the diffusion coefficient matrix.

When close to the grain boundary, the magnitude of J_V increases [Fig. 4.4(c)], showing a transition from the slow-mode diffusion behavior to the fast-mode diffusion one. Eventually, interdiffusion shifts to a completely fast-mode diffusion that is similar to the Darken's type interdiffusion along the grain boundary. This is a manifestation that the vacancy source efficiency that depends on the distance from sources and sinks determines the diffusion mechanisms.

4.10 Summary

In this chapter, we demonstrated that vacancy-mediated diffusion in a substitutional alloy is enhanced along grain boundaries due to the supply and removal of vacancies, which change interdiffusion from slow-mode diffusion to fast-mode diffusion. This process, which becomes more pronounced in alloys having a large Kirkendall effect, will further enhance diffusion along grain boundaries in addition to any short-circuit diffusion mechanisms due to lower activation barriers there. For the *Kirkendall-effect-assisted grain boundary diffusion* mechanism described above, the role of grain boundaries in enhancing diffusion will differ qualitatively and quantitatively for alloys that exhibit a strong Kirkendall effect from those that do not, and it provides additional considerations when optimizing grain size distributions in heterostructures

that are to resist degradation as a result of interdiffusion.

Another finding, which may possibly be more surprising, is the significant suppression of the fast-mode diffusion away from the grain boundary. This stems from the fact that the vacancy gradient quickly responds to the diffusing species concentration gradients to cancel the driving force for the fast-mode diffusion. In this case, the slow-mode diffusion, or the intermixing mode, becomes dominant and carries the system toward equilibrium at a longer time scale. Therefore, the enhancement of grain boundary diffusion observed in experiments may in some cases be a manifestation of the suppression of diffusion in the low grain-boundary-density case as compared to the high-density case.

CHAPTER V

DIFFUSE INTERFACE APPROACH FOR CONVENTIONAL MODELING

5.1 Introduction

In Chapter III, we examined a rigorous model in which the diffusion of vacancies is explicitly considered in a one-dimensional domain. The volume change caused by vacancy injection and elimination was treated in this case by a planar lattice shift for the planar geometry and by considering conservation of volume for the cylindrical geometry. The motions of free surfaces, grain boundaries, and the mass center of the diffusion couple due to vacancy generation and annihilation were observed in these simulations. When the vacancy source density was high, the rigorous model converged to the conventional treatment, namely Darken's model (see Section 3.1.5). In Chapter IV, we examined the effect of grain boundaries serving as vacancy sources and sinks on interdiffusion in a substitutional binary alloy with a perfect lattice structure. It was found that the interdiffusion process can be characterized as a combination of the slow mode and the fast mode of interdiffusion. When vacancies are efficiently supplied or removed to maintain their equilibrium mole fraction, the fast mode dominates the interdiffusion process. In the absence of abundant sources and sinks of vacancies, the number of vacancies must be conserved, just like the atomic species, and the slow mode of interdiffusion is observed. We found that the fast-mode diffusion near the grain boundary contributes to an enhancement of diffusion. However, arbitrary volume expansion and contraction due to vacancy injection and elimination, which are

expected to occur in these systems, were not incorporated in these two-dimensional simulations. In a more realistic situation, the deformation, caused by lattice creation or destruction, occurs to maintain an equilibrium vacancy concentration. This phenomenon is difficult to implement in multidimensional simulations. In this chapter, we present a numerical method developed to circumvent this difficulty. The method is applied to simultaneously simulate the plastic deformation and the concentration evolution in a binary alloy during interdiffusion.

In Darken's analysis, the lattice flow relative to an observer's frame fixed outside of the diffusion zone is predicted to compensate for the unequal fluxes between the two atomic diffusing species. Shortly after his analysis was published, it was generally accepted that the marker motion observed experimentally was consistent with a one-dimensional incompressible plastic flow stemming from different diffusivities of different species. However, because diffusion couples are often not fully one dimensional, the plastic deformation is not necessarily confined to the diffusion direction. Instead, bending of a diffusion couple, as well as bulging and grooving near the diffusion interface induced by the Kirkendall effect, are commonly observed in experiments. To model the structural deformation during interdiffusion, models were proposed decades ago that account for vacancy generation and elimination and that also incorporate plastic deformation due to local volumetric changes [137]. In these models, plastic deformation is described by a Newtonian flow. These models have only been employed to simulate concentration evolutions in one-dimensional or quasi one-dimensional diffusion couples, due to the difficulties in numerical implementation for tracking the structural deformation in directions other than the diffusion direction [45, 50, 80, 110]. For higher dimensions, analytical solutions only exist for a very limited number of cases where the diffusion couples have very simple geometries [79]. For cases with a general geometry, only a two-dimensional simulation of Kirkendall effect-induced deformation has appeared in the literature [81] to the best of our knowl-

edge. That simulation was based on the traditional model of interdiffusion. In that work, an adaptive meshing technique for the finite element method was necessary for following the structural deformation.

A robust, flexible numerical method that allows the simulation of diffusion as well as the resulting deformation in two and three dimensions based on a rigorous model of the Kirkendall effect is needed to gain insights into interdiffusion phenomena involving complex geometries. The main challenge here is associated with following free boundaries internal to the computational domain, at which internal boundary conditions must be imposed. Therefore, we developed a diffuse interface method to circumvent the difficulty in explicitly tracking the boundaries (e.g., surfaces of the diffusion couples or grain boundaries within the couples) and imposing internal boundary conditions on these boundaries. In this chapter, the numerical method is described and applied to the traditional model of interdiffusion. In the next chapter, the method is applied to a few cases with the rigorous model of interdiffusion to demonstrate that it is an efficient and powerful tool to examine Kirkendall effect-induced deformation.

5.2 Model

5.2.1 Diffusion Under Advection

Our starting point is the generalized diffusion equation of vacancy concentration taken in the lattice frame for a thermodynamically ideal substitutional binary alloy:

$$\frac{\partial C_V}{\partial t} = -\nabla \cdot J_V + \left(1 - \frac{C_V}{\rho}\right) g, \qquad [2.29]$$

where the fluxes are determined by Fick's first law for a multi-component system:

$$J_V = -D_{VV}\nabla C_V - D_{VB}\nabla C_B. \qquad [2.11a]$$

Note that these concentration rate and flux equation can also be expressed in mole-, mass-, or volume-based quantities by incorporating molecular mass or volume into the

equations [138, 139, 81, 80]. Although the atomic volumes of different species usually differ and local lattice distortions commonly occur in reality, such considerations in a substitutional lattice structure will only change the problem quantitatively. For simplicity, we assume that the atomic volumes of all diffusing species are identical, such that the lattice structure remains unaltered during diffusion process. In addition, this solid is assumed to be completely incompressible ($\rho =$ constant).

The conventional treatment of interdiffusion assumes that a solid contains a sufficiently dense distribution of vacancy sources and sinks to constantly maintain the vacancy mole fraction at its thermal equilibrium value everywhere in the solid: $C_V = \rho X_V^{eq}$. As a result, the time and spatial derivatives in Eqs. (2.29) and (2.11a) go to zero, and one can calculate the vacancy generation rate that maintains the equilibrium vacancy mole fraction according to

$$g = -\frac{\nabla \cdot (D_{VB} \nabla C_B)}{1 - X_V^{eq}}. \tag{5.1}$$

Since the lattice density and vacancy concentration are kept constant, the vacancy generation rate is identical to the lattice site generation rate. The lattice site generation gives rise to a local volume change that, according to Eq. (2.35), can be viewed as a local stress-free dilatational strain rate: $\dot{\varepsilon}_\Omega = g/\rho$. For a plastically deformable body, $\dot{\varepsilon}_\Omega$ contributes to a flow velocity, $\mathbf{v}$, to relax the volume expansions or contractions, where $\mathbf{v}$ is a vector quantity. The determination of the magnitudes and directions of the plastic flow will be discussed later. At an arbitrary point in the solid, the number of lattice sites is described by a simple conservation law of lattice flux:

$$\frac{\partial \rho}{\partial t} = -\nabla \cdot J_\rho + g, \tag{5.2}$$

where $J_\rho = \mathbf{v}\rho$ is the flux of lattice sites. Similar to Eq. (2.26), the first term on the right-hand side of Eq. (5.2) accounts for lattice site accumulation, and the second term accounts for lattice site generation. Since ρ is constant, the time and spatial

derivatives of ρ in Eq. (5.2) go to zero, providing the relation between the lattice generation rate and the velocity field:

$$\nabla \cdot \mathbf{v} = g/\rho. \tag{5.3}$$

Equation (5.3) clearly indicates that the divergence of the velocity field of plastic deformation equals the stress-free dilatational strain rate.

In the laboratory frame outside the solid, the fast diffuser flux needs to include the advective effect due to deformation:

$$J_B^L = J_B + \mathbf{v}C_B, \tag{5.4}$$

where $\mathbf{v}$ is the plastic flow velocity relative to the laboratory frame, and the flux in the lattice frame is expressed by:

$$J_B = -D_{BV}\nabla C_V - D_{BB}^V \nabla C_B. \qquad \text{[2.11b]}$$

In the conventional treatment, the vacancy concentration gradient is zero; thus, the B flux is related only to its own concentration gradient: $J_B = -D_{BB}^V \nabla C_B$. Conservation of the fast diffuser is found by taking the divergence of its flux, yielding the rate of concentration change:

$$\frac{\partial C_B}{\partial t} = -\nabla \cdot J_B^L \Longrightarrow \frac{\partial C_B}{\partial t} + \mathbf{v} \cdot \nabla C_B = -\nabla \cdot J_B - C_B \nabla \cdot \mathbf{v}. \tag{5.5}$$

By substituting Eq. (5.3) into the second term on the right-hand side of Eq. (5.5), we obtain the diffusion equation for the fast diffuser in the laboratory frame:

$$\frac{\partial C_B}{\partial t} + \mathbf{v} \cdot \nabla C_B = -\nabla \cdot J_B - \frac{C_B}{\rho} g, \tag{5.6}$$

where the terms on the right-hand side are identical to those in Eq. (2.30) obtained for the lattice frame. The second term on the left-hand side has the usual form that accounts for advection and, together with the partial time derivative, represents the Lagrangian time derivative of C_B. To compare with Darken's analysis, we can simplify

the above formulation to a one-dimensional system, where Eq. (5.3) is written as

$$\frac{\partial v}{\partial x} = -\frac{1}{\rho(1-X_V^{eq})}\frac{\partial}{\partial x}\left(D_{VB}\frac{\partial C_B}{\partial x}\right) \Longrightarrow v = -\frac{1}{\rho(1-X_V^{eq})}D_{VB}\frac{\partial C_B}{\partial x}. \tag{5.7}$$

For a thermodynamically idea binary substitutional random alloy, the diffusion coefficients are related by $D_{VB} = D_{AA} - D_{AB} + D_{BA} - D_{BB} = L_{AA}/X_A - L_{AB}/X_B - L_{BB}/X_B + L_{AB}/X_A = D_A - D_B$, where D_A and D_B are the intrinsic diffusion coefficients in Darken's model, Eq. (2.23). Therefore, the velocity expression is identical to that predicted by Darken's analysis, Eq. (2.20), except for the small factor $1/(1-X_V^{eq}) \approx 1$. In one dimension, Eq. (5.4) can be reorganized to give

$$J_B^L = -D_{BB}^V\frac{\partial C_B}{\partial x} - \frac{X_B}{1-X_V^{eq}}D_{VB}\frac{\partial C_B}{\partial x} = -\tilde{D}\frac{\partial C_B}{\partial x}, \tag{5.8}$$

where $D_{BB}^V + X_B D_{VB} = X_A D_B + X_B D_A = \tilde{D}$, if the small factor X_V^{eq} is neglected. Again, this expression recovers the concentration evolution equation in Darken's model, Eq. (2.22). Therefore, our formulation derived from the rigorous model converges to the conventional model at the limit where there are abundant vacancy sources and sinks.

5.2.2 Formulation of Plastic Deformation

Let us consider the formulation of the plastic deformation caused by the stress-free dilatational strain. The following derivation is similar to those in Refs. [79, 81]. According to the theory of continuum mechanics the strain is the spatial derivative of the displacement. Thus, the strain rate is given by taking the time derivative of the total strain. Assuming the deformation is small, one obtains the strain rate in index notation as

$$\dot{\varepsilon}_{ij} = \frac{1}{2}\left(\frac{\partial v_i}{\partial x_j} + \frac{\partial v_j}{\partial x_i}\right), \tag{5.9}$$

where the subscript i denotes the directional component, and repeated indices imply summation over the index. The strain rate can be decomposed into a stress-free

dilatational strain rate and a shear strain rate:

$$\dot{\varepsilon}_{ij} = \frac{1}{d}\dot{\varepsilon_{\Omega}}\delta_{ij} + \dot{\gamma}_{ij}, \tag{5.10}$$

where $\dot{\varepsilon}_{\Omega}$ is proportional to the vacancy generation rate according to Eq. (2.35), δ_{ij} is the Kronecker delta ($\delta = 1$ for $i = j$; otherwise $\delta = 0$), and d is the dimensionality of the coordinate system. The first term accounts for the change in the number of the lattice sites, and the second term accounts for the strain relaxation. Note that the factor $1/d$ is adopted under the assumption that the deformation is small, and any volume change due to lattice generation is isotropic. While both the lattice structure and grain boundary orientations can lead to anisotropy, we do not consider crystallographic orientations in a macroscopic model, since the entire solid is assumed to contain vacancy sources and sinks.

We employ a linear constitutive relation for a viscous Newtonian fluid to model the plastic deformation process. The shear strain rate is related to the stress components by

$$\dot{\gamma}_{ij} = \frac{1}{2\eta}\left(\sigma_{ij} - \frac{1}{d}\sigma_{kk}\delta_{ij}\right), \tag{5.11}$$

where σ_{ij} is the stress component and η is the viscosity of the material. The quantity in parenthesis in Eq. (5.11) is the so-called deviatoric stress tensor. By substituting Eqs. (5.9), (2.35) and (5.11) into (5.10) and rearranging terms, we arrive at

$$\sigma_{ij} = \frac{\sigma_{kk}\delta_{ij}}{d} + \eta\left(\frac{\partial v_i}{\partial x_j} + \frac{\partial v_j}{\partial x_i}\right) - \eta\frac{2g}{d\rho}\delta_{ij}. \tag{5.12}$$

We assume that the deformation induced by diffusion is a slow process, such that the inertial force can be neglected. Therefore, the stress state of the solid body is governed by the mechanical equilibrium equation: $\partial\sigma_{ij}/\partial x_j = 0$. This assumption means that the solid material is always in an instantaneous quasi-static state. Taking

the divergence of Eq. (5.12), one obtains

$$-\frac{\partial P}{\partial x_j}+\frac{\partial}{\partial x_j}\eta\left(\frac{\partial v_i}{\partial x_j}+\frac{\partial v_j}{\partial x_i}\right)-\frac{\partial}{\partial x_j}\left(2\frac{\eta g}{d\rho}\right)=0, \tag{5.13}$$

where $P=-\sigma_{kk}/d$ is defined as an effective pressure. The first two terms in Eq. (5.13) correspond to the conventional Navier-Stokes equation for a slow flow, and the third term represents the dilatational strain caused by the unequal atomic fluxes in the system. The same slow-flow viscous fluid expressions are commonly applied to model Nabarro-Herring creep [140].

Up to this point, we have obtained three governing equations for the conventional model, including one for the concentration evolution and two for diffusion-induced plastic deformation:

$$\frac{\partial C_B}{\partial t}+\mathbf{v}\cdot\nabla C_B=\nabla\cdot D^V_{BB}\nabla C_B+\frac{C_B}{\rho_e}\nabla\cdot D_{VB}\nabla C_B, \tag{5.14}$$

$$-\nabla P+\nabla\cdot(\eta\nabla\mathbf{v})+\nabla\left(\frac{2\eta}{d\rho_e}\nabla\cdot D_{VB}\nabla C_B\right)=0, \tag{5.15}$$

$$\nabla\cdot\mathbf{v}=-\frac{1}{\rho_e}\nabla\cdot D_{VB}\nabla C_B, \tag{5.16}$$

where $\rho_e=\rho(1-X_V^{eq})$ is a constant scalar quantity, and $\nabla\mathbf{v}=(\partial v_i/\partial x_j+\partial v_j/\partial x_i)$ is a tensor of second rank. Equations (5.14) and (5.16) are scalar equations, while Eq. (5.15) is a vector equation. In a multi-dimensional domain, Eq. (5.15) consists of force balance equations in all the directions of the coordinate system. Note that these three equations only govern the physics within the solid domain. These equations can be solved using a standard finite element method in a sharp interface description, as has been done in Ref. [81]. However, since the solid domain of the diffusion couple involves time evolution of deformation during diffusion, a remeshing technique is required for tracking the deformation. In cases with severe deformations, the remeshing process may be computationally too expensive.

5.2.3 Phase Field Approach

We propose a flexible and efficient approach to solve the same set of equations using a diffuse interface description. In this model, an order parameter is employed to distinguish the solid medium from its environment (air), as the entire computational domain contains two phases: solid and air. Within each phase, the order parameter is kept at a constant value: e.g., $\psi = 1$ in the solid phase and $\psi = 0$ in the vapor phase. The order parameter value transitions continuously between these two phases in the narrow interfacial region. Thus, the region where $0 < \psi < 1$ is the interfacial region between solid and air, with $\psi = 0.5$ corresponding to the nominal interfacial position. Note that diffusion is confined to occur only in the solid phase.

A common example of a diffuse interface model for a conserved order parameter such as density is the Cahn-Hilliard equation. Similar to a typical phenomenological rate equation, the derivation of such an equation starts with the description of the total free energy in the system:

$$F_\psi = \int_{\mathbf{x}} \left[f(\psi) + \frac{\varkappa^2}{2} (\nabla \psi)^2 \right] d\mathbf{x}, \tag{5.17}$$

where $\mathbf{x}$ is the position vector, $f(\psi)$ is the free energy density functional in terms of the order parameter, and $\varkappa$ is the gradient energy coefficient. The second term in the integrand accounts for the penalty for a sharp change in the order parameter across the interfacial region. The integration is carried out over the volume of the entire domain. Similar to the typical phenomenological rate equation, the flux of the order parameter is proportional to the driving force:

$$J_\psi = -L_M \nabla \mu_\psi, \tag{5.18}$$

where L_M is a mobility coefficient, and $\nabla \mu_\psi$ is the driving force, defined as the gradient of the chemical potential. The potential μ_ψ represents the rate of change of the free energy in Eq. (5.17) with respect to the change in the order parameter

within a characteristic volume. This potential is obtained by taking the variational derivative of the total free energy with respect to the order parameter: $\mu_\psi = \delta F/\delta\psi$. Note that the chemical potential has units of energy per volume as a result of taking the variational derivative. By taking the divergence of the order parameter flux, the conservation law of the order parameter field gives the governing equation for the evolution of ψ, the well-known Cahn-Hilliard equation:

$$\frac{\partial\psi}{\partial t} = -\nabla\cdot J_\psi = \nabla\cdot L_M\nabla\left(\frac{\partial f}{\partial\psi} - \varkappa^2\nabla^2\psi\right). \tag{5.19}$$

If the free energy density functional in Eq. (5.17) is a double-well function, the system tends to separate into two phases, where each phase takes one of the two bulk values of the order parameter corresponding to the well minima in order to reduce the bulk free energy. For example, a simple choice of a double-well function having its minima at $\psi = 0$ and $\psi = 1$ would be

$$f(\psi) = W\psi^2(1-\psi)^2, \tag{5.20}$$

where $W/16$ is the barrier height between the two wells. Since the order parameter ψ is a non-dimensional quantity, W has units of energy per unit volume, and the gradient energy coefficient, $\varkappa$, has units of the square root of energy per unit length ($\sqrt{\text{energy/length}}$). Taking the derivative of Eq. (5.20) gives $\partial f/\partial\psi = 2W(\psi - 3\psi^2 + 2\psi^3)$. For a simple one-dimensional case with boundary conditions $\psi = 1$ at $x = -\infty$ and $\psi = 0$ at $x = \infty$, one can solve

$$2W(\psi - 3\psi^2 + 2\psi^3) - \varkappa^2\frac{\partial\psi}{\partial x} = 0 \tag{5.21}$$

to determine the steady-state order parameter profile. The non-trivial solution of this equation is given by

$$\psi = \frac{1}{2}\left[1 - \tanh\left(\frac{1}{2}\frac{\sqrt{2W}}{\varkappa}x\right)\right]. \tag{5.22}$$

Note that the quantity $\varkappa/\sqrt{2W}$ has units of length and can be considered the char-

acteristic length of the interface. The hyperbolic tangent solution indicates that the order parameter is distributed uniformly away from the interface at $x = 0$. On the other hand, the order parameter continuously transitions from $\psi = 1$ to $\psi = 0$ in a narrow region near $x = 0$. The distance from $\psi = 0.1$ to $\psi = 0.9$ is approximately $4\sqrt{2W}/\varkappa$, which can then be considered the thickness of the interface (see Fig. 5.1). The interfacial energy between the two phases can be written in terms of the gradient energy coefficient and the gradient of the order parameter:

$$\gamma_\psi = \int_{-\infty}^{+\infty} \varkappa^2 \left(\frac{d\psi}{dx}\right)^2 dx. \tag{5.23}$$

At steady state, the relation $\varkappa d\psi/dx = -\sqrt{2f(\psi)}$ can be used to change the variable in Eq. (5.23), such that $\varkappa^2(d\psi/dx)^2 = -\sqrt{2\varkappa^2 f(\psi)}(d\psi/dx)$. The interfacial energy is therefore obtained as

$$\gamma_\psi = \int_0^1 \sqrt{2\varkappa^2 f(\psi)} d\psi = \varkappa \frac{\sqrt{2W}}{6}, \tag{5.24}$$

which balances the bulk free energy at steady state. By changing the well height of the free energy density function, W, and the gradient energy coefficient, $\varkappa$, the interfacial thickness and the interfacial energy can be controlled in a phase field simulation. When the interfacial thickness is taken to be zero, the diffuse interface description converges to the sharp interface description. However, in practice, it is sufficient to require that the thickness be much smaller than the characteristic lengths such as the domain size or the radii of curvature in the system. Numerically, we require that at least four to six grid points exist within the interfacial regions in order to accurately describe the steep changes in the gradient of the order parameter.

Up to this point, the Cahn-Hilliard equation is derived in the absence of advection. Equation (5.19) can be simply modified to include a general advective term describing

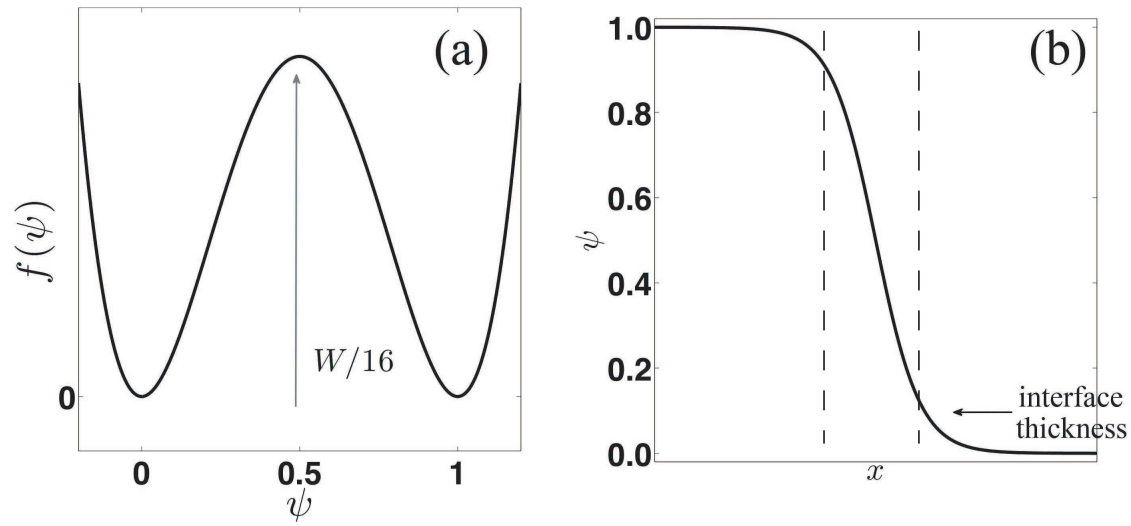

Figure 5.1: (a) Schematic plot of a double-well free energy functional with the minima at $\psi = 0$ and $\psi = 1$. (b) Schematic plot of an order parameter profile in one dimension.

phase morphological evolution under an external or internal flow field:

$$\frac{\partial \psi}{\partial t} + \mathbf{v} \cdot \nabla \psi = L_M \nabla^2 \left(\frac{\partial f}{\partial \psi} - \varkappa^2 \nabla^2 \psi \right). \tag{5.25}$$

Here, for simplicity, the mobility in Eq. (5.25) is assumed to be independent of the order parameter. One should note that the velocity field is defined over the entire computational domain, in both solid and vapor phases.

Now we consider conservation of momentum, which allows us to obtain the velocity field. In a system containing two coexisting phases, Eq. (5.15) is modified to include the capillary force exerted on the interfaces [90, 141]:

$$-\nabla P + \nabla \cdot (\eta \nabla \mathbf{v}) + \nabla \left(\frac{2\eta}{d\rho_e} \nabla \cdot D_{VB} \nabla C_B \right) + \mu_\psi \nabla \psi = 0. \tag{5.26}$$

This interfacial force term [90, 141] stems from the free energy change in time due to advection, according to

$$\left. \frac{\partial F}{\partial t} \right|_{\text{advection}} = \int_{\mathbf{x}} \left. \frac{\delta F}{\delta \psi} \frac{\partial \psi}{\partial t} \right|_{\text{advection}} d\mathbf{x}, \tag{5.27}$$

where $\delta F / \delta \psi = \mu_\psi$ and $\partial \psi / \partial t|_{\text{advection}} = -\nabla \cdot (\mathbf{v}\psi)$. Performing integration by parts

and using the divergence theorem on the right-hand side of Eq. (5.27), one obtains

$$-\int_{\mathbf{x}} \mu_\psi \nabla \cdot (\mathbf{v}\psi) d\mathbf{x} = -\int_s \mu_\psi \psi \mathbf{n} \cdot \mathbf{v} ds - \int_{\mathbf{x}} \mathbf{v} \cdot (\mu_\psi \nabla \psi) d\mathbf{x}. \tag{5.28}$$

Here, s is the boundary of this volume, $\mathbf{n}$ is the unit normal vector of the boundary, ds is the area element on s, and the volume is taken to be large enough that the boundary of the volume does not include any interfaces. Since the system is a closed system, the integrand along boundary goes to zero, and the free energy change must balance the kinetic energy change due to the interfacial force. As a result, we can obtain

$$\int_{\mathbf{x}} \mathbf{v} \cdot (\mu_\psi \nabla \psi) d\mathbf{x} = \int_{\mathbf{x}} \mathbf{v} \cdot \mathbf{f}_s d\mathbf{x}, \tag{5.29}$$

where $\mathbf{f}_s$ is the interfacial force appearing in Eq. (5.26). This type of modified equation of momentum balance, along with the advective Cahn-Hilliard equation, form the model-H phase field model, which has been widely used in modeling multi-phase fluid flow [142, 143, 140, 144].

The momentum balance equation can be nondimensionalized in a procedure similar to that used for Eq. (3.4). We define a reference diffusion coefficient, D_0, a reference concentration, ρ (the lattice density), a length scale, l, and a time scale, $\tau = l^2/D_0$, as in Eq. (3.4). We also scale the velocity with the quantity l/τ, the effective pressure with a reference pressure, P_0, and the viscosity coefficient with the reference value $P_0\tau$ in Eq. (5.26):

$$\begin{aligned} &-\frac{1}{l}\hat{\nabla} P_0 \hat{P} + \frac{1}{l}\hat{\nabla} \cdot \left(P_0 \tau \hat{\eta} \frac{1}{l}\hat{\nabla} \frac{l}{\tau} \hat{\mathbf{v}} \right) + \frac{1}{l}\hat{\nabla} \left(\frac{2}{d} \frac{P_0 \tau \hat{\eta}}{\rho_e} \frac{1}{l}\hat{\nabla} \cdot D_0 \hat{D}_{VB} \frac{1}{l}\hat{\nabla} \rho X_B \right) + W \hat{\mu}_\psi \frac{1}{l}\hat{\nabla}\psi = 0 \\ &\implies -\hat{\nabla}\hat{P} + \hat{\nabla} \cdot \left(\hat{\eta}\hat{\nabla}\hat{\mathbf{v}} \right) + \hat{\nabla} \left(\frac{2\hat{\eta}}{d(1 - X_V^{eq})} \hat{\nabla} \cdot \hat{D}_{VB} \hat{\nabla} X_B \right) + \frac{W}{P_0} \hat{\mu}_\psi \hat{\nabla}\psi = 0, \end{aligned} \tag{5.30}$$

where the hats denote nondimensionalized quantities: $\hat{P} = P/P_0$, $\hat{\eta} = \eta/(P_0\tau)$, $\hat{\mathbf{v}} = \mathbf{v}/(l/\tau)$, and $\hat{\mu}_\psi = \mu_\psi/W$. The nondimensionalized quantity W/P_0 characterizes the relative magnitude of the viscous force and the interface force. Similarly, we

nondimensionalize Eq. (5.25) into

$$\begin{aligned}\frac{1}{\tau}\frac{\partial\psi}{\partial\hat{t}}+\frac{l}{\tau}\hat{\mathbf{v}}\cdot\frac{1}{l}\hat{\nabla}\psi=&\frac{D_0}{l^2}\hat{L}_M\hat{\nabla}^2\left(\frac{\partial\hat{f}}{\partial\psi}-\frac{\varkappa^2}{Wl^2}\hat{\nabla}^2\psi\right)\\ \Longrightarrow\frac{\partial\psi}{\partial\hat{t}}+\hat{\mathbf{v}}\cdot\hat{\nabla}\psi=&\hat{L}_M\hat{\nabla}^2\left(\frac{\partial\hat{f}}{\partial\psi}-\hat{\varkappa}^2\psi\right),\end{aligned}\tag{5.31}$$

where $\hat{L}_M = L_M W/D_0$ is a dimensionless mobility coefficient. Furthermore, since we only consider diffusion and lattice site generation within the solid phase, we multiply the lattice generation rate by the order parameter, such that no lattice generation occurs in the vapor phase while the lattice generation within the solid phase remains unchanged. The equation relating the plastic flow velocity and the lattice generation rate is nondimensionalized into

$$\hat{\nabla}\cdot\hat{\mathbf{v}}=-\frac{\psi}{1-X_V^{eq}}\hat{\nabla}\cdot\hat{D}_{VB}\hat{\nabla}X_B=\hat{g}_\psi.\tag{5.32}$$

Similarly, Eq. (5.14) is modified and nondimensionalized into

$$\frac{\partial X_B}{\partial\hat{t}}+\hat{\mathbf{v}}\cdot\hat{\nabla}X_B=\hat{\nabla}\cdot\hat{D}^V_{BB}\hat{\nabla}X_B-X_B\hat{g}_\psi.\tag{5.33}$$

For convenience, the hats denoting dimensionless quantities will be omitted from the equations in the following derivation.

The evolution of the order parameter and the concentration are simulated by stepping in time, whereas the velocity field is solved in a quasi-steady-state manner at each time step. In this plastic deformation model, we treat the solid phase as a very viscous fluid, while the vapor phase is treated as a nearly inviscid fluid. A simple way to implement this is to define the viscosity coefficient as $\eta(\psi) = \bar{\eta}\psi + \epsilon$, where $\bar{\eta}$ is a constant viscosity coefficient for the solid phase and $\epsilon \ll \bar{\eta}$ is a small value used to avoid numerical instability. To solve the velocity field with a variable viscosity coefficient, we adopt the iterative method introduced in Refs. [143, 140]. The divergence of the viscous stress tensor is decomposed to a linear part and a residual

part, giving

$$\nabla \cdot (\eta \nabla \mathbf{v}) = h \nabla \cdot (\nabla \mathbf{v}) + \mathbf{r}_v, \tag{5.34}$$

where h is a constant scalar numerical parameter for the scheme (normally taken between $0.5\bar{\eta}$ and $\bar{\eta}$), and $\mathbf{r}_v$ is a vector quantity that is also iterated. Note the identity that $\nabla \cdot (\nabla \mathbf{v}) = \nabla^2 \mathbf{v} + \nabla(\nabla \cdot \mathbf{v})$, where $\nabla^2 \mathbf{v} = \partial^2 v_i / \partial x_j \partial x_j$ is a vector containing the Laplacian of each velocity component. Using Eqs. (5.32) and (5.34), one can rewrite Eq. (5.30) as

$$-\nabla P + h \nabla^2 \mathbf{v} + h \nabla g_\psi + \mathbf{r}_v + \frac{2}{d} \nabla (\eta g_\psi) + \frac{1}{C_a} \mu_\psi \nabla \psi = 0, \tag{5.35}$$

where $C_a = P_0 / W$. By taking the divergence of Eq. (5.35) and rearranging the terms, one obtains a scalar equation:

$$-\nabla^2 P + h \nabla \cdot (\nabla^2 \mathbf{v}) - h \nabla^2 g_\psi + \nabla \cdot \mathbf{r}_v + \frac{2}{d} \nabla^2 (\eta + hd) g_\psi + \frac{1}{C_a} \nabla \cdot (\mu_\psi \nabla \psi) = 0, \tag{5.36}$$

where $h \nabla \cdot (\nabla^2 \mathbf{v}) = h \nabla^2 (\nabla \cdot \mathbf{v}) = h \nabla^2 g_\psi$ will cancel the third term. This gives one of the two equations for the iterative scheme:

$$\nabla^2 P^{(n)} = \nabla \cdot \mathbf{r}_v^{(n-1)} + \frac{2}{d} \nabla^2 (\eta_1 g_\psi) + \frac{1}{C_a} \nabla \cdot (\mu_\psi \nabla \psi), \tag{5.37}$$

where $\eta_1 = \eta + hd$, and the superscript n denotes quantities at the n-th iterative step. Equation (5.37) is Poisson's equation for the pressure field. The second and third terms on the right-hand side do not change during the iteration performed within a time step.

To obtain the equation for the velocity field, we can reorganize Eq. (5.35) to

$$\nabla^2 \mathbf{v}^{(n)} = \frac{1}{h} \left[\nabla P^{(n)} - \mathbf{r}_v^{(n-1)} - \frac{2}{d} \nabla (\eta_2 g_\psi) - \frac{1}{C_a} \mu_\psi \nabla \psi \right], \tag{5.38}$$

where $\eta_2 = \eta + (hd/2)$. This equation contains Poisson's equation for the velocity component along each coordinate direction. The vector $\mathbf{r}_v$ is obtained from Eq. (5.34),

and is updated during iteration:

$$\mathbf{r}_v^{(n)} = \nabla \cdot (\eta \nabla \mathbf{v}^{(n)}) - h\nabla^2 \mathbf{v}^{(n)} - h\nabla g_\psi. \tag{5.39}$$

Within each time step, the pressure field and velocity field are solved iteratively until the pressure and the velocity components converge to stable values. The velocity field is then substituted into the advective terms in the order parameter and concentration evolution equations.

5.2.4 Smooth Boundary Method

Since diffusion only occurs within the solid phase, a no-flux boundary condition must be applied to the solid-vapor interface in this model. Here, we adopt the smooth boundary method to implement this condition at the diffuse interfaces. This method has been successfully employed in simulating diffusion processes [145, 146] and wave propagation [97, 98] constrained within geometries described by order parameters with no-flux boundary conditions imposed on the diffuse interfaces. We show that this method is applicable to general flux boundary conditions (Neumann boundary conditions) in this chapter. Furthermore, we generalize this method to general boundary conditions, including Dirichelet and mixed boundary conditions, in the next chapter.

Instead of directly solving the diffusion equation, we multiply both sides of Eq. (5.33) by the order parameter that describes the domain of the solid phase:

$$\psi \frac{\partial X_B}{\partial t} - \psi \mathbf{v} \cdot \nabla X_B = \psi \nabla \cdot (D_{BB}^V \nabla X_B) - \psi X_B g_\psi, \tag{5.40}$$

where the first term on the right-hand side can be replaced by the relation $\psi \nabla \cdot (D_{BB}^V \nabla X_B) = \nabla \cdot (\psi D_{BB}^V \nabla X_B) - \nabla \psi \cdot (D_{BB}^V \nabla X_B)$. The normal flux across the interface can be defined by $B_f = \mathbf{n} \cdot (D_{BB}^V \nabla X_B)$, where $D_{BB}^V \nabla X_B$ is the vector flux. In a diffuse interface model, the unit normal vector of the interface is given by

$\mathbf{n} = \nabla\psi/|\nabla\psi|$. Using these relations in Eq. (5.40), we obtain an auxiliary equation:

$$\psi\frac{\partial X_B}{\partial t} - \psi\mathbf{v}\cdot\nabla X_B = \nabla\cdot(\psi D_{BB}^V \nabla X_B) - |\nabla\psi|B_f - \psi X_B g_\psi. \tag{5.41}$$

To demonstrate that this auxiliary equation satisfies the assigned Neumann boundary condition (or specifying boundary flux), we use the one-dimensional version of Eq. (5.41) without loss of generality. By reorganizing and integrating over the interface region, we obtain

$$\int_{a_i-\xi/2}^{a_i+\xi/2} \psi\left(\frac{\partial X_B}{\partial t} - v\frac{\partial X_B}{\partial x} + X_B g_\psi\right)dx = \psi D_{BB}^V \frac{\partial X_B}{\partial x}\bigg|_{a_i-\xi/2}^{a_i+\xi/2} - \int_{a_i-\xi/2}^{a_i+\xi/2}\left|\frac{\partial\psi}{\partial x}\right| B_f dx, \tag{5.42}$$

where $a_i - \xi/2 < x < a_i + \xi/2$ is the region of the interface, and ξ is the thickness of the interface. Following Refs. [145, 97, 98], we shall introduce the mean value theorem of integrals, which states that, for a continuous function, $f(x)$, there must exist a constant value, h_0, such that:

$$\min f(x) < \frac{1}{q-p}\int_p^q f(x)dx = h_0 < \max f(x), \tag{5.43}$$

where $p < x < q$. By eliminating the second term on the right-hand side of Eq. (5.42), the no-flux boundary condition can be imposed, as in Refs. [145, 97, 98]. However, we retain the term in order to maintain the generality of the method. Therefore, the analysis below is an extension of the original method that greatly expands the applicability of the method.

Since the function on the left-hand side of Eq. (5.42) is continuous and finite within the interfacial region, we can use the mean value theorem of integrals to obtain the relation:

$$\int_{a_i-\xi/2}^{a_i+\xi/2} \psi\left(\frac{\partial X_B}{\partial t} - v\frac{\partial X_B}{\partial x} + X_B g_\psi\right)dx = h_0\xi. \tag{5.44}$$

Using the conditions that $\psi = 1$ at $x = a_i + \xi/2$ and $\psi = 0$ at $x = a_i - \xi/2$, the first

term in the right-hand side of Eq. (5.42) is written as:

$$1 \cdot D_{BB}^{V} \frac{\partial X_B}{\partial x}\bigg|_{a_i+\xi/2} - 0 \cdot D_{BB}^{V} \frac{\partial X_B}{\partial x}\bigg|_{a_i-\xi/2} = D_{BB}^{V} \frac{\partial X_B}{\partial x}\bigg|_{a_i+\xi/2}. \tag{5.45}$$

Since $|\partial\psi/\partial x| = 0$ for $x < a_i - \xi/2$ or $x > a_i + \xi/2$, the second term on the right-hand side of Eq. (5.42) can be replaced by:

$$\int_{a_i-\xi/2}^{a_i+\xi/2} \left|\frac{\partial \psi}{\partial x}\right| B_f dx = \int_{-\infty}^{+\infty} \left|\frac{\partial \psi}{\partial x}\right| B_f dx. \tag{5.46}$$

Substituting Eqs. (5.44), (5.45) and (5.46) into (5.42), we obtain:

$$h_0 \xi = D_{BB}^{V} \frac{\partial X_B}{\partial x}\bigg|_{a_i+\xi/2} - \int_{-\infty}^{+\infty} \left|\frac{\partial \psi}{\partial x}\right| B_f dx. \tag{5.47}$$

Taking the limit of Eq. (5.47) for $\xi \to 0$:

$$\begin{aligned} 0 &= D_{BB}^{V} \frac{\partial X_B}{\partial x}\bigg|_{a_i} - \int_{-\infty}^{+\infty} \lim_{\xi \to 0} \left|\frac{\partial \psi}{\partial x}\right| B_f dx \\ \implies D_{BB}^{V} \frac{\partial X_B}{\partial x}\bigg|_{a_i} &= \int_{-\infty}^{+\infty} \delta(x - a_i) B_f dx \\ \implies D_{BB}^{V} \frac{\partial X_B}{\partial x}\bigg|_{a_i} &= B_f\Big|_{a_i}, \end{aligned} \tag{5.48}$$

where $\lim_{\xi \to 0} |\partial\psi/\partial x| = \delta(x - a_i)$ for when ψ has a form as in Eq. (5.22), and $\delta(x - a_i)$ is the Dirac delta function. The Dirac delta function has the property that $\int_{-\infty}^{+\infty} \delta(x - a_i) f(x) dx = f(a_i)$. Therefore, Eq. (5.48) clearly shows that the smooth boundary method recovers the Neumann boundary condition at the diffuse interface when the interfacial thickness approaches zero. This convergence is satisfied for stationary and moving boundaries [145].

When the smooth boundary method is numerically implemented, the specified value of the boundary condition can vary in both space and time. It is possible to impose boundary conditions that are functions of the composition, order parameters, or other fields that evolve in time. Therefore, the smooth boundary method is a very powerful method for solving time-dependent boundary value problems and can be

used to describe the evolution of many physical systems.

To solve the diffusion equation of the traditional model of the Kirkendall effect in isolated solid objects, we apply the above method to impose a no-flux boundary condition ($B_f = 0$) at the solid-vapor interfaces to formulate the following governing equation:

$$\frac{\partial X_B}{\partial t} - \mathbf{v} \cdot \nabla X_B = \frac{1}{\psi} \nabla \cdot (\psi D_{BB}^V \nabla X_B) - X_B g_\psi. \tag{5.49}$$

This equation is solved along with the model-H phase-field equations described above.

5.3 Results

5.3.1 One-dimensional Simulations

We start by verifying our model in one dimension, for which we have sharp-interface results. In a one-dimensional system, the deviatoric stress vanishes: $\sigma_{ij} - \sigma_{kk}\delta_{ij}/d = \sigma_{11} - \sigma_{11}/1 = 0$; thus, the momentum balance, Eq. (5.15), becomes

$$\frac{\partial}{\partial x} 2\eta \frac{\partial v}{\partial x} - \frac{\partial}{\partial x}\left(2\eta \frac{g}{\rho}\right) = 0 \Longrightarrow \frac{\partial v}{\partial x} = \frac{g}{\rho} = -\frac{1}{\rho_e}\frac{\partial}{\partial x}\left(D_{VB}\frac{\partial C_B}{\partial x}\right), \tag{5.50}$$

which is identical to the lattice-site conservation equation obtained for a one-dimensional system, Eq. (5.7). Note that, in one dimension, this equation is also identical to Eq. (5.16). The velocity field can be directly calculated according to the vacancy flux described by the B concentration gradient. Thus, the iterative method introduced in Eqs. (5.37) − (5.39)for solving the plastic-flow (lattice-flow) velocity is unnecessary. When the velocity obtained by Eq. (5.50) is substituted into Eq. (5.49), this formulation recovers the conventional treatment of interdiffusion (Darken's model) in the solid phase.

The physical parameters in Table 3.2 are used in the numerical simulation. The fast-to-slow atomic hop frequency ratio is selected to be 4, i.e., $\Gamma_B = 4\Gamma_A$. The fast diffuser (B) and the slow diffuser (A) are initially on the left half and the right half the domain, respectively. The computational domain is discretized into 256 grid

points. We initialize an order parameter profile that distinguishes the solid and vapor phases, where the interfaces are approximately at the $27th$ and $233rd$ grid points. We select the length scale to be 1 μm, such that the solid domain spans approximately 216 μm. The reference diffusion coefficient is chosen to be $D_0 = a^2\Gamma_A = 7.48 \times 10^{-8}$ cm^2/s, which gives the time scale $\tau = 1.34 \times 10^{-1}$ s. The advective Navier-Stokes equation, Eq. (5.30), only requires suitable parameters to maintain numerical stability while exhibiting a strong viscous flow behavior. Therefore, we select the dimensionless quantities $C_a = 1\times10^8$ and $\bar{\eta} = 1\times10^5$ for Eq. (5.30), and $\hat{\varkappa} = 1$ and $\hat{L}_M = 1.25\times10^{-8}$ for the advective Cahn-Hilliard equation, Eq.(5.31). Here, we select a smaller value for the fast-to-slow atomic hop frequency ratio of 4, than the value used in Chapter III, which is closer to the experimental values for common metals [9]. Therefore, these results are quantitatively different from the results in Section 3.1.5. However, the two sets of results remain qualitatively similar. It should be noted that the two sets of results have different reference frames. The results presented below take the laboratory reference frame. Therefore, no rigid shift of the diffusion couple is observed. In Section 3.1.5, the reference frame is taken to be the lattice frame, and, therefore, a rigid shift of the diffusion couple is observed. However, the two results are equivalent when the results are transformed to have a consistent frame.

Figure 5.2(a) shows the nondimensionalized concentration evolution of the fast diffuser using the new diffuse interface method. The results are in excellent agreement with the results obtained by directly solving the conventional Darken's equation, Eq. (2.21b) (also shown in Fig. 5.2(a), with circles). This again shows that our rigorous formulation is identical to the conventional model when the vacancy concentration is kept constant everywhere in the solid, as in Section 3.1.5, except for the difference in choice of the reference frame. The excellent agreement also demonstrates that the smooth boundary method can accurately impose the no-flux boundary condition at the solid-vapor interfaces described by a smoothly varying order parameter. It is

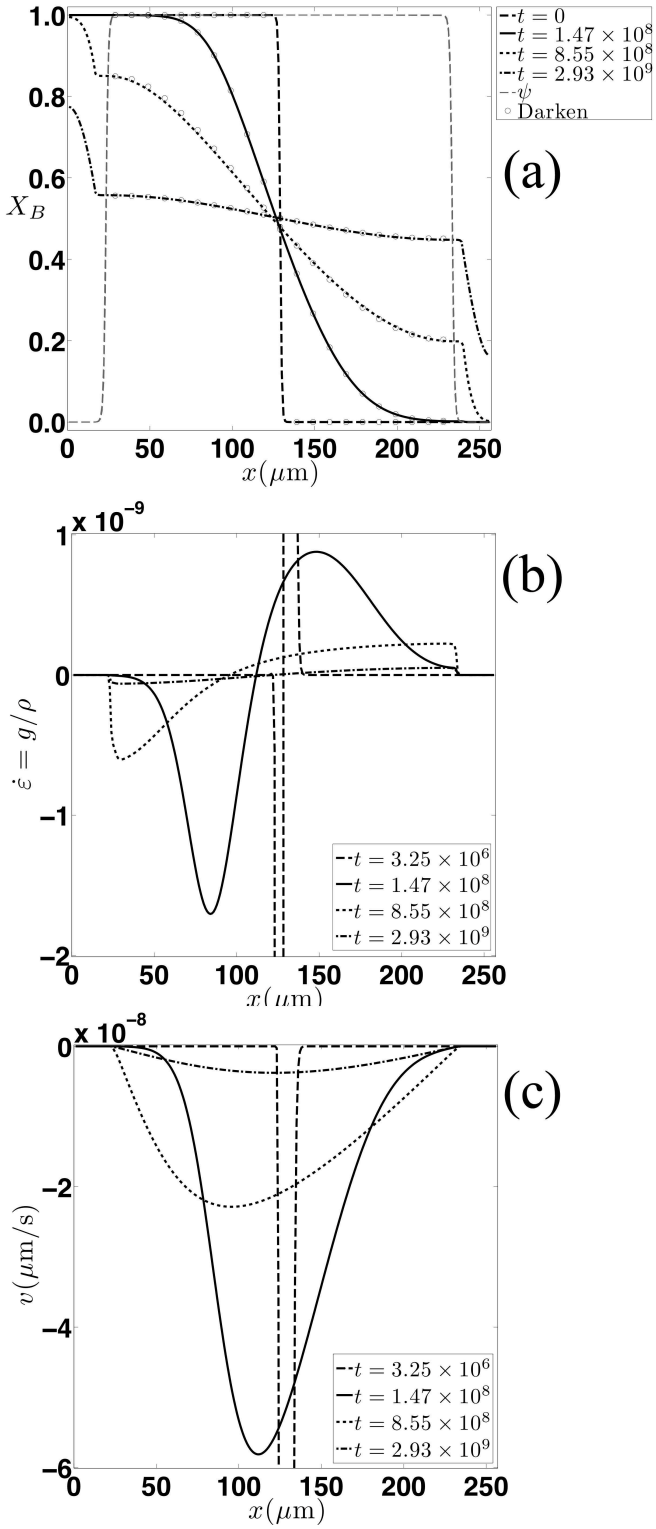

Figure 5.2: One dimensional smooth-boundary-method simulation results of the (a) X_B evolution, (b) dilatational strain, and (c) plastic flow velocity. The unit of time is second.

noted that the concentration in the vapor phase evolves as well, since we perform calculations in the entire domain, containing both solid and vapor phases. However, diffusion in the vapor phase is irrelevant and does not affect the evolution of the interface or the concentration within the solid, as pointed out in Ref. [97].

Figure 5.2(b) shows the dilatational strain calculated at various times. The dilatational strain is proportional to the lattice generation rate, which regulates the vacancy concentration at it equilibrium value. The result behaves similarly to the plot shown in Fig. 3.7(a), having a wide region of comparatively smaller vacancy generation on the A-rich side and a narrow region of larger vacancy elimination on the B-rich side. The large difference in the magnitudes of the dilatational strain between these two examples is a result of the large difference in the length and time scales. Figure 5.2(c) shows the plastic flow velocity calculated according to the lattice generation rate. During diffusion, lattice planes are created in the A-rich region and are eliminated in the B-rich region, as illustrated in Fig. 5.2(b). The lattice planes then move toward the B-rich region to maintain a constant lattice density at the velocity shown in Fig. 5.2(c). Due to the no-flux boundary conditions at the two ends of the solid phase, lattice generation does not occur at the two ends; thus, the internal velocity goes to zero at these points. As a result, the overall size of the solid remains invariant. This result can also be understood from the conservation of the lattice site within the solid phase. Based on the excellent agreement between the plastic deformation model and the conventional model, these results prove that the rigid shift between the lattice frame and the laboratory frame in Darken's model is a direct outcome of an incompressible plastic flow [137, 80, 79, 81].

5.3.2 Diffusion-Induced Lateral Deformation

In a two-dimensional domain, an iterative scheme, Eqs. (5.37) $-$ (5.39), is necessary for solving the plastic flow velocity. The iterative method involves solving one

Poisson's equation for the effective pressure field and two Poisson's equations for the velocity field along the x and y directions. Among several possible matrix solvers that can be applied, we employ the alternative direction implicit (ADI) method for numerical implementation. In the first two-dimensional simulation, we select a 192 μm $\times$ 64 μm solid phase described by a continuous order parameter profile in the middle of a 256 μm $\times$ 128 μm computational box. The inter-grid spacing is taken to be 1 μm. We apply zero-pressure and zero-velocity boundary conditions on the computational box boundaries. The fast diffuser and the slow diffuser initially occupy the right and left halves of the solid, respectively. Figure 5.3 shows snapshots of the nondimensionalized B concentration (X_B) profiles and the order parameter profiles (ψ) during interdiffusion. Here, we only show the X_B value within the solid phase, and omit the trivial values in the vapor phase. During diffusion, B atoms diffuse toward the left-hand side, alleviating the concentration gradient in the diffusion zone. As diffusion proceeds, the original A-rich side expands due to lattice-site generation. On the other hand, the original B-rich side contracts due to lattice-site destruction. This process results in lateral deformations normal to the main diffusion direction. A bulge on the A-rich side and a groove on the B-rich side initially form near the diffusion front. The bulge then extends toward the B-rich side, as it increases the lateral size of the A-rich region. On the other hand, the groove continues to move toward the B-rich side. The deformation eventually stops when the B concentration (and thus the A concentration) reaches a uniform distribution within the solid phase. The shape of the diffusion couple changes from an initially rectangular block to a bottle shape with a larger width on the initially A-rich side and a narrower neck on the initially B-rich side.

Snapshots of the dilatational strain rate at three different times are shown in Fig. 5.4. Similar to the one-dimensional case, lattice sites are generated in a larger region on the A-rich side, and are eliminated in a narrower region on the B-rich side.

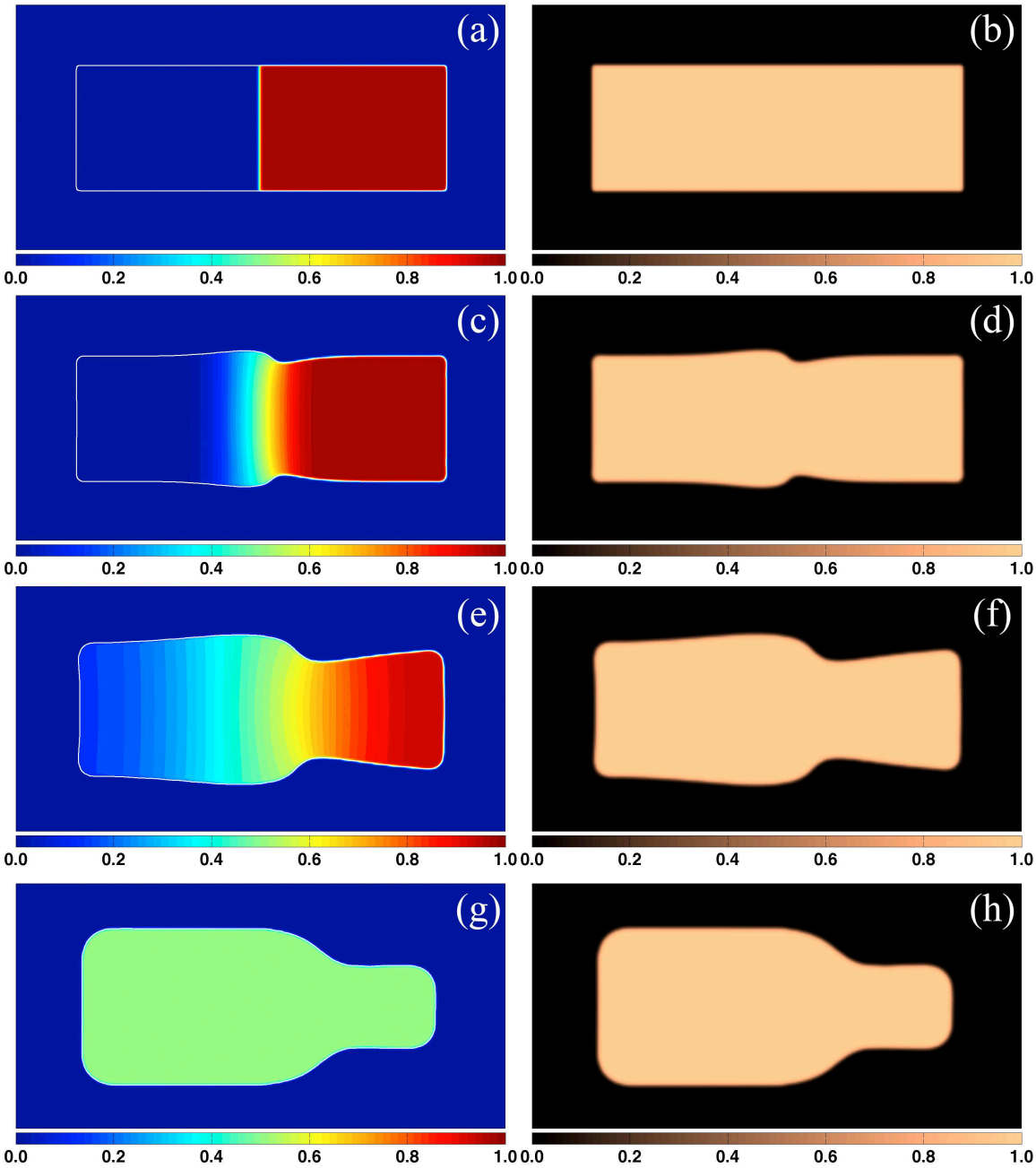

Figure 5.3: Snapshots of X_B evolution (left column) and order parameter ψ (right column) in a 192 μm $\times$ 64 μm slab diffusion couple, taken at $t = 0$, $t = 3.96 \times 10^7$, $t = 5.09 \times 10^8$, and $t = 4.32 \times 10^9$ sec (from the top row to the bottom row).

As diffusion proceeds, the regions where lattice-site generation and destruction occur shift to the left and to the right, respectively, as they broaden. In a two-dimensional case, the lattice site generation results in deformation along the primary diffusion direction (perpendicular to the diffusion front) and the secondary lateral direction. The plastic flow velocity is illustrated in Fig. 5.5, where the black and gray arrows denote the velocity within the solid and vapor phases, respectively. The velocity vectors start from regions where lattice sites are generated and end in regions where lattice sites are eliminated. In the early stage [Fig. 5.5(a)], the plastic flow is confined to a small region near the diffusion front. As lattice generation and elimination spread through the diffusion couple, the plastic flow also spreads along the main diffusion direction [Figs. 5.5(b) and 5.5(c)].

During simulations, the positions of artificial markers are updated and recorded for tracking the transport of materials under deformation. These markers are initially evenly distributed in the solid. In the early stage, the markers initially near the diffusion front move to the right [Fig. 5.6(b)]. The locations of the markers initially at the diffusion front are noted by line segments outside the solid, and show a clear shift to the right. As diffusion continues, the diffusion zone expands, as does the motion of the markers [Fig. 5.6(c)]. Nevertheless, all markers move to the B-rich region on the right. These marker motions are accompanied by a lateral contraction on the B-rich side and a lateral expansion on the A-rich side, as observed by changes in the density of markers in the lateral direction. When the concentration reaches its final homogeneous distribution, the inter-marker spacing becomes nearly uniform in each of the originally B-rich and A-rich regions divided by the markers located initially at the diffusion front [Fig. 5.6(d)] . This result indicates that the B-rich and A-rich sides of the diffusion couple undergo an overall uniform volume contraction and expansion, respectively, since their original diffuser concentration is uniformly distributed on either side. Bending deformation near the initial diffusion front can be

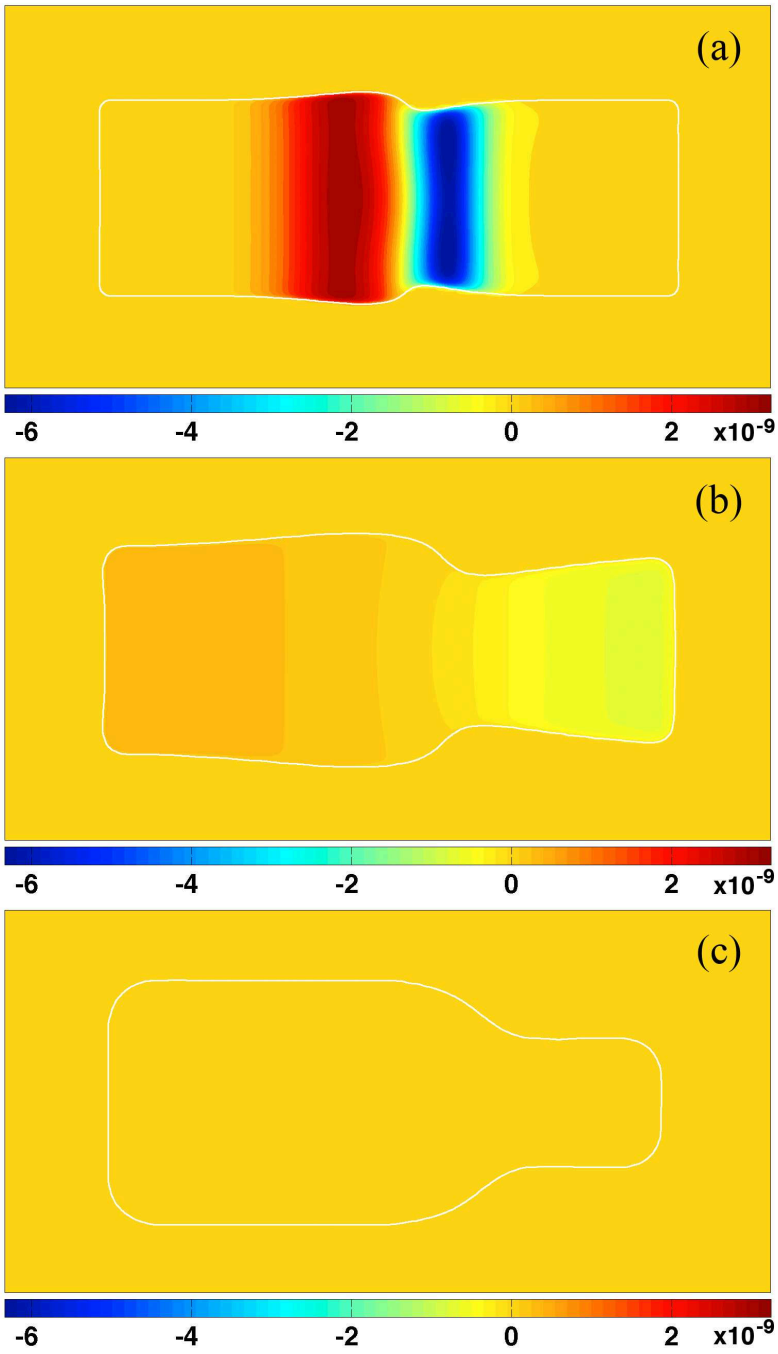

Figure 5.4: Dilatational strain rate $\dot{\varepsilon}$ (proportional to the lattice site generation rate) taken at (a) $t = 3.96 \times 10^7$, (b) $t = 5.09 \times 10^8$, and (c) $t = 4.32 \times 10^9$ sec. The white contour lines indicate the solid-vapor interfaces.

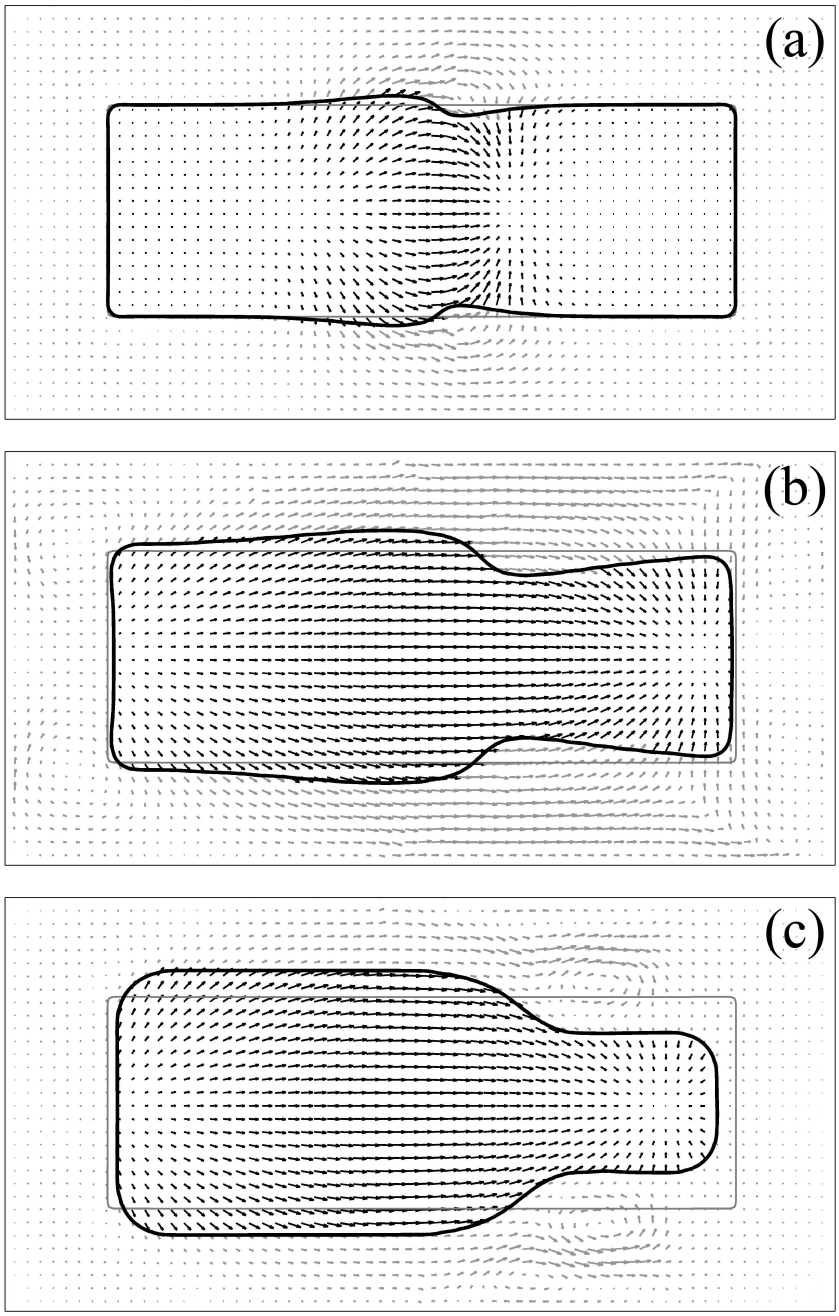

Figure 5.5: The plastic flow velocity calculated according to the dilatational strain shown in Fig. 5.4. The black arrows denote velocity within the solid phase, and the gray arrows denote velocity within the vapor phase.

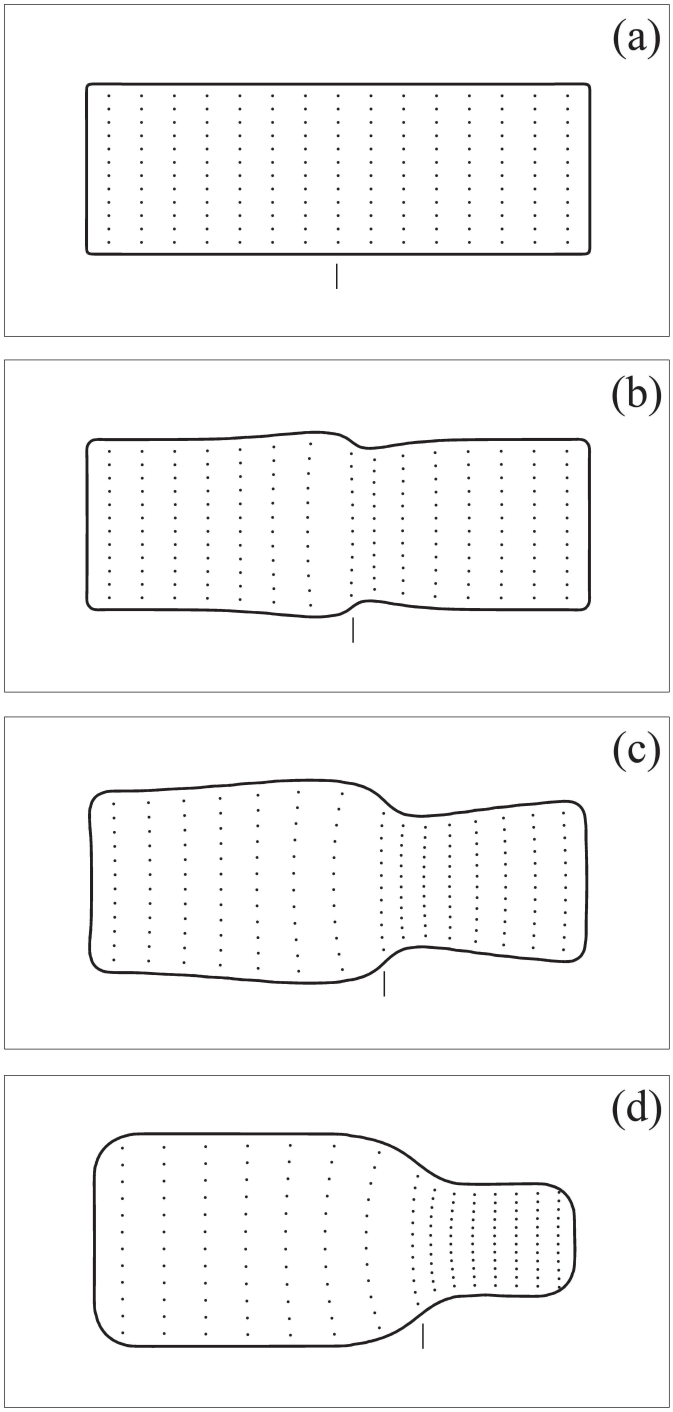

Figure 5.6: Snapshots of the marker positions corresponding to Fig. 5.3. The markers initially located at the diffusion front are indicated by the short line segments outside the solid.

observed from the curved arrangement of markers. However, this bending deformation diminishes toward the ends of the diffusion couple.

5.3.3 Diffusion-Induced Bending Deformation

We next perform simulations of interdiffusion in a thin plate diffusion couple. The solid phase spans a 192 μm $\times$ 48 μm domain within a 384 μm $\times$ 116 μm computational box. The fast diffuser and the slow diffuser initially occupy the top and bottom halves of the solid, respectively, as shown in Fig. 5.7(a). Thus, diffusion is mainly along the direction of the shorter dimension of the couple. Figure 5.7 shows snapshots of the X_B profile during diffusion. The original rectangular slab evolves to an arc-shaped object. During diffusion, vacancies diffuse to the B-rich region and annihilate there, resulting in volume contractions. On the other hand, vacancy generation in the A-rich region leads to volume expansions. The combination of contraction on the inner side and expansion on the outer side results in a bending of the slab into an arc. This result demonstrates the Kirkendall-effect-induced bending deformation that has been observed experimentally [45, 46, 50], see Fig. 1.1(d). The deformation of the left and right boundaries of the solid, which is similar to the lateral deformation in the previous case, is also observed in this simulation. Therefore, the bending of the plate can be understood as a linear network of smaller sections of narrow diffusion couples, similar to the case studied in the previous section, Section 5.3.2. Consequently, the extent of bending depends on the ratio of the sample dimensions parallel and perpendicular to the diffusion front. Figure 5.8 illustrates how the marker positions change over time. We observe the volume contraction on the inner side and the volume expansion on the outer side by noting changes in the marker density. The inter-marker spacing decreases along both the radial and lateral directions in the initially B-rich region, whereas it increases in the initially A-rich region, although to a lesser degree [Fig. 5.8(d)].

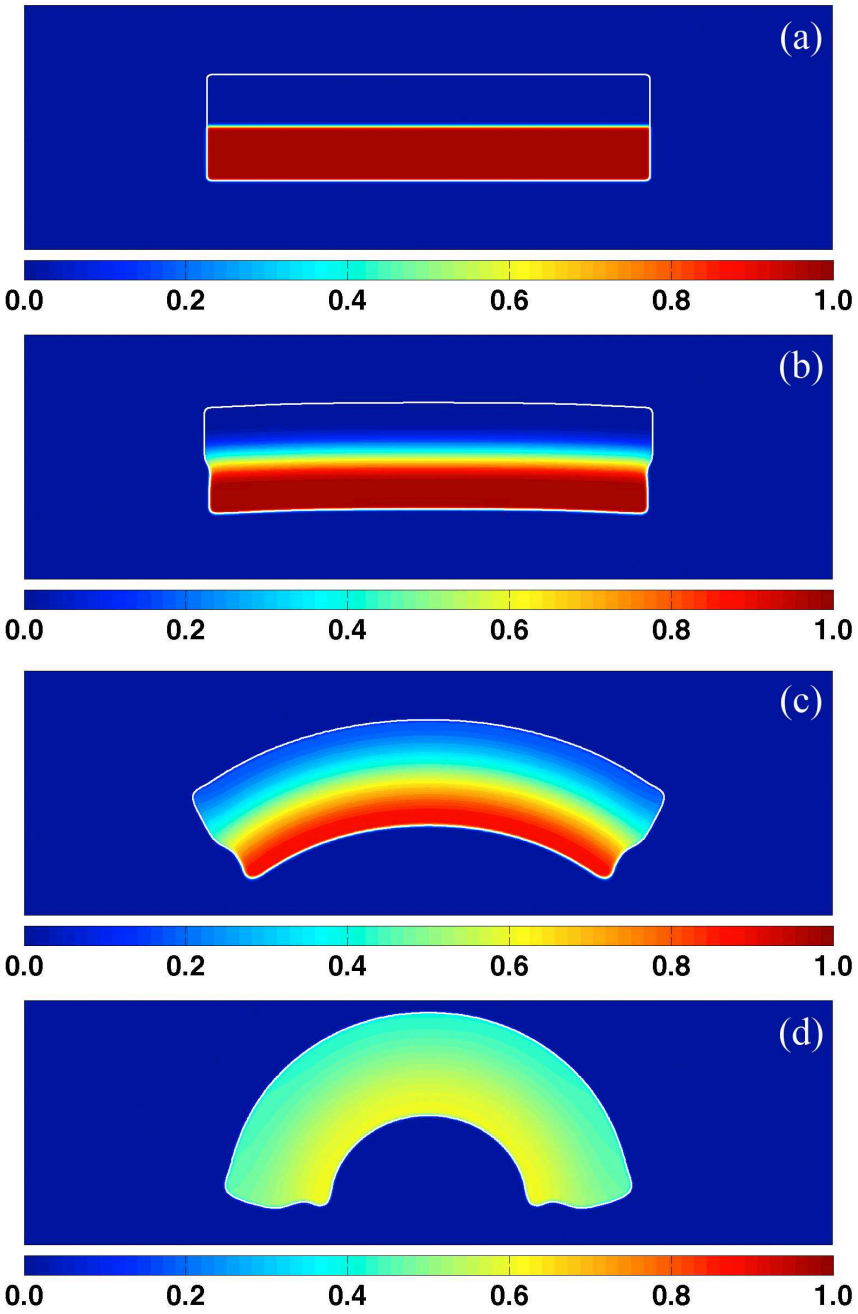

Figure 5.7: Snapshots of X_B evolution in a 192 μm $\times$ 48 μm plate diffusion couple taken at (a) $t = 0$, (b) $t = 5.98 \times 10^6$, (c) $t = 3.95 \times 10^7$, and (d) $t = 1.40 \times 10^8$ sec. The white contour lines indicate the solid-vapor interfaces.

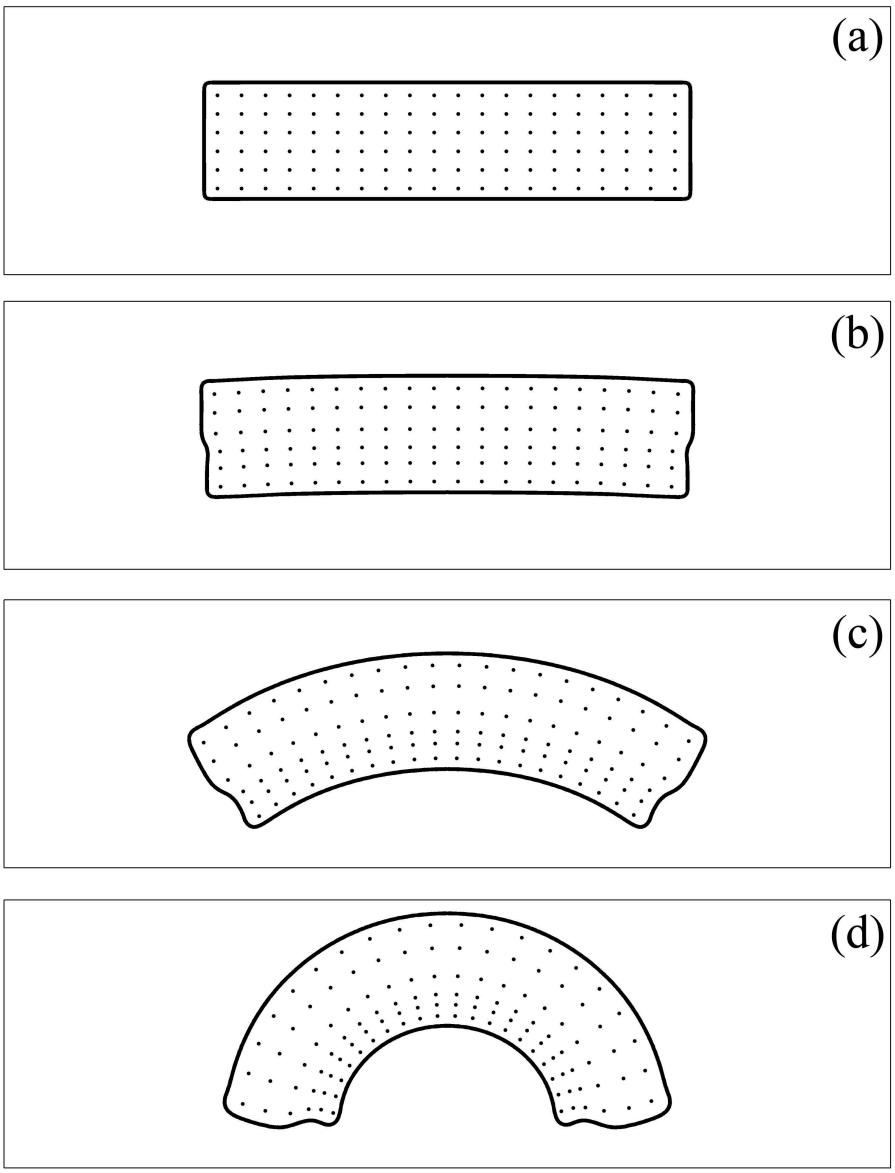

Figure 5.8: Snapshots of the marker positions corresponding to Fig. 5.7.

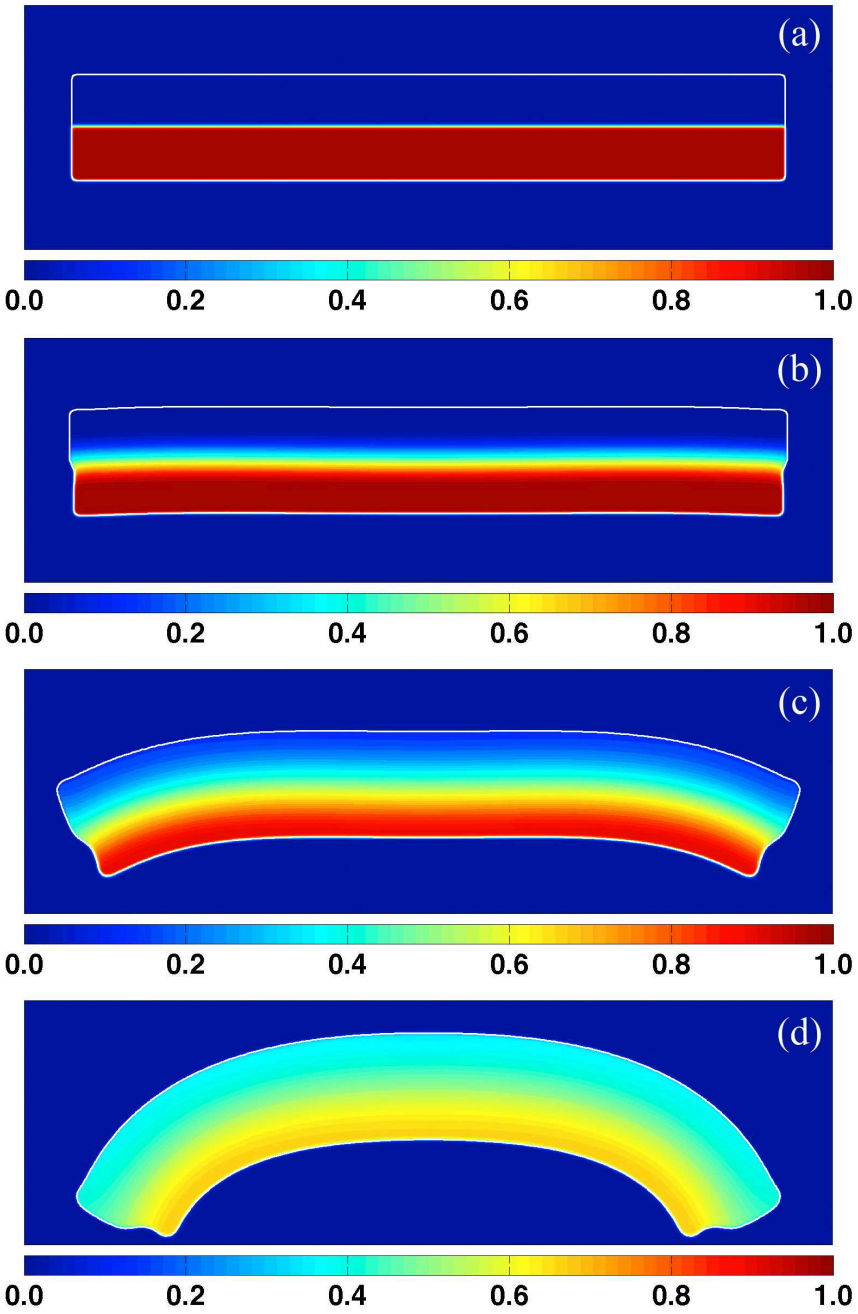

Figure 5.9: Snapshots of X_B evolution in a 256 μm $\times$ 48 μm plate diffusion couple taken at (a) $t = 0$, (b) $t = 5.14 \times 10^6$, (c) $t = 3.60 \times 10^7$, and (d) $t = 9.81 \times 10^7$ sec. The white contour lines indicate the solid-vapor interfaces.

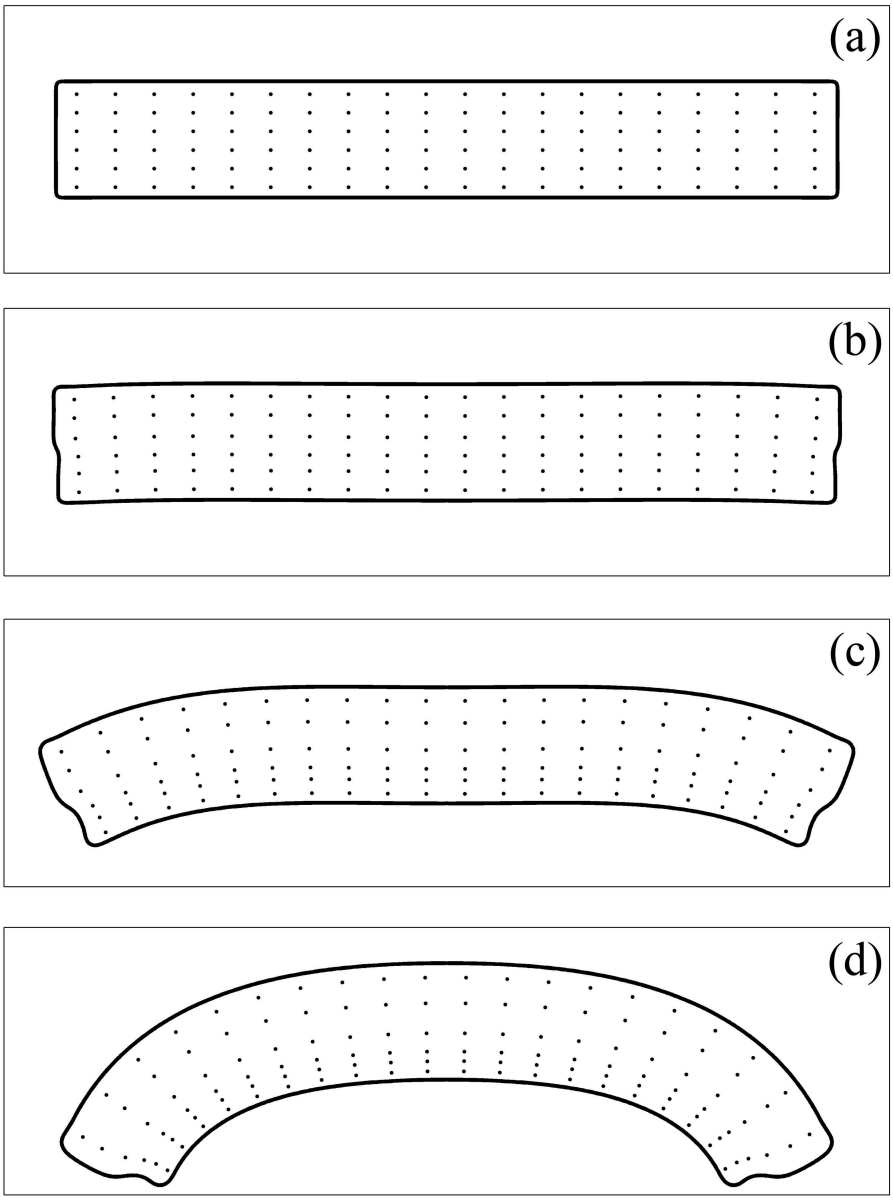

Figure 5.10: Snapshots of the marker positions corresponding to Fig. 5.9.

We also simulate interdiffusion in a plate-shaped diffusion couple with a larger aspect ratio, 256 μm $\times$ 48 μm. Snapshots of the X_B profile are shown in Fig. 5.9. As in the previous case, we observe bending deformation induced by diffusion in the simulation. However, one may notice that the bending deformation initiates from the left and right ends of the diffusion couple [Figs. 5.9(b) and 5.9(c)]. In the middle of the solid, lateral deformation is constrained along the horizontal direction. Thus, this geometry is locally equivalent to a one-dimensional diffusion couple along the vertical direction. At the two horizontal free ends, lateral deformation is less constrained and is able to relieve the local volume changes. Therefore, bending deformation initiates at the two ends. As the bending deformation propagates toward the middle of the solid, diffusion is no longer constrained in the vertical direction, leading to bending deformation. The above argument can also be supported by the marker movements shown in Fig. 5.10. As can be seen in Fig. 5.10(c), the inter-marker spacing remains comparatively uniform along the horizontal direction, even as the two ends undergo bending deformation. In the later stage [Fig. 5.10(d)], most markers near the center are still aligned in a relatively straight line along the vertical direction. The dynamics of bending-deformation propagation have not been simulated before, since Kirkendall-effect-induced bending deformation has only been solved in a quasi-1D cylindrical geometry that implicitly incorporated a pre-existing radial curvature [45, 50].

5.3.4 Deformation in a General Geometry

We also provide an example of a diffusion couple with a more complex geometry to demonstrate the capability of this method to handle such cases. We consider the lap joint shown in Fig. 5.11(a). Two 167 μm $\times$ 44 μm slabs are partially connected on their lateral sides. The contacting region is around 1/3 of the slab length. One slab is made of pure B material, and the other slab is made of pure A material. This diffusion couple is located in the middle of a 348 μm $\times$ 160 μm computational box.

All material properties and boundary conditions on the computational box boundary are similar to those used in the previous sections in this chapter.

Figure 5.11 shows snapshots of the X_B concentration profile and the shape of the diffusion couple during diffusion. As expected, diffusion initiates at the contacting region. As the B atoms diffuse from the bottom slab to the top slab through the contacting region, we observe a pronounced lateral contraction at the left end of the bottom slab, whereas we observe a lateral expansion at the right end of top slab [Fig. 5.11(b)]. The contraction on the fast diffuser side and the expansion on the slow diffuser side in the diffusion zone continue as diffusion proceeds. The combination of contraction and expansion leads to a bending deformation in the joint region, which is indicated by the tilting of the two slabs from the horizontal axis, as shown in Fig. 5.11(c). Away from the joint region, diffusion is constrained along the axes of the longer dimensions of the slabs. Thus, a comparatively uniform contraction and a uniform expansion occur in the bottom slab and the top slab, respectively. This conclusion is evident when comparing Fig. 5.11(d) and 5.11(a). Away from the joint, the bottom slab remains nearly rectangular in shape but smaller in size. The top slab increases its size but also remains rectangular away from the joint.

By examining the marker movements, we also observe a contraction in the bottom slab and an expansion in the top slab near the joint region [Fig. 5.12(c)], which results in a bending deformation. In Fig. 5.12(d), nearly straight alignment of the markers away from the joint region is evident. We observe a similar uniform distribution of markers in Fig. 5.6(d) for the wire-like diffusion couple. These observations indicate that bending deformation occurs near the contacting region where contraction takes place on one side and expansion takes place on the other side. Away from the initial diffusion front, free expansions and contractions can occur, and, thus, the deformation is dominated by dilatation. However, near the regions where the fast diffusers and slow diffusers were initially in contact, the difference in the volume change causes

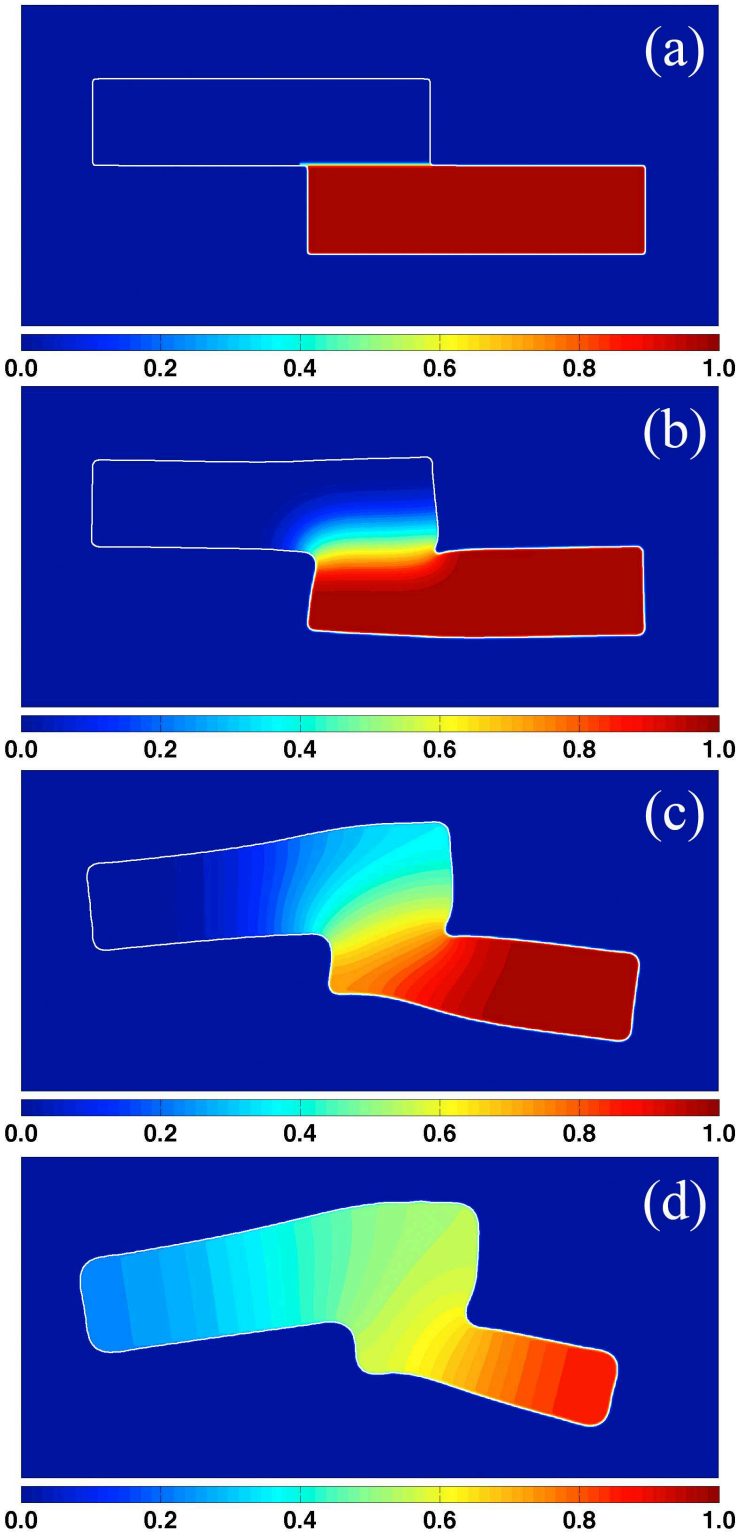

Figure 5.11: Snapshots of X_B evolution in a lap-joint diffusion couple taken at (a) $t = 0$, (b) $t = 2.94 \times 10^7$, (c) $t = 2.37 \times 10^8$, and (d) $t = 1.54 \times 10^9$ sec. The white contour lines indicate the solid-vapor interfaces.

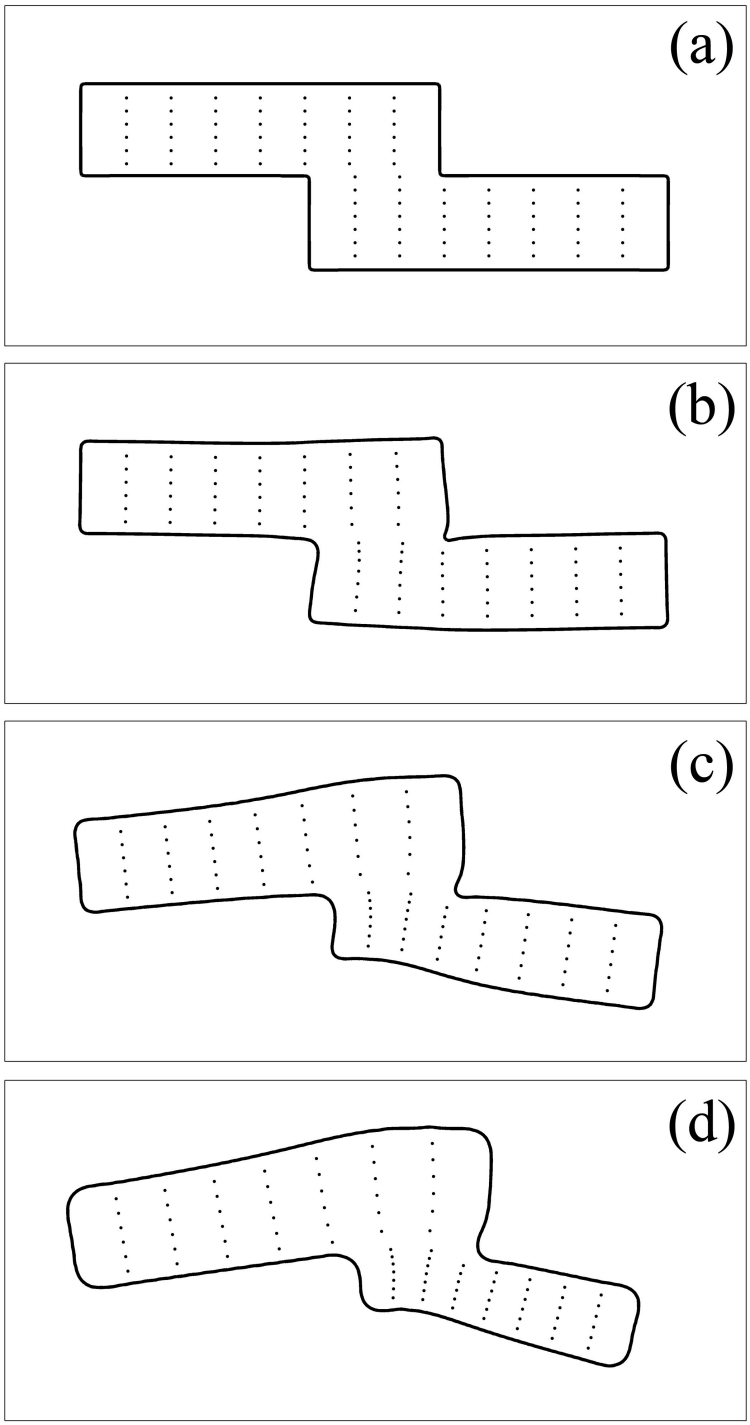

Figure 5.12: Snapshots of the marker positions corresponding to Fig. 5.11.

more complex types of deformation, including bending.

5.4 Conclusions Regarding the Plastic Deformation Model

In this chapter, we develop and demonstrate a numerical method for solving partial differential equations with internal boundary conditions in order to simulate Kirkendall-effect-induced deformation phenomena. Our governing equations are equivalent to the traditional model of the Kirkendall effect, based on Darken's analysis. This model is valid when sufficiently dense vacancy sources constantly maintain the vacancy concentration at the equilibrium value throughout the solid and when the solid is assumed to be completely incompressible and to plastically deform in response to lattice site generation and elimination. To solve the diffusion equations within the solid body that deforms during interdiffusion, we develop a smooth boundary formulation that permits generalized Neumann boundary conditions to be imposed on the internal boundaries within the computational domain. The 1D simulation results prove that the assumption of plastic deformation is consistent with Darken's model. We also demonstrate the accuracy of the smooth boundary method. Lateral deformations and bending deformations induced by interdiffusion are simulated in two dimensions. The simulation results are qualitatively consistent with experimental observations [47, 45, 46, 50]. The generality of the model is also demonstrated by simulating a lap joint geometry, where bending deformation, volume shrinkage, and volume expansion are observed in different parts of the diffusion couple.

At the macroscopic scale, vacancy diffusion between sources and sinks is neglected because the typical distance between vacancy sources and sinks is very small compared to the size of the diffusion zone. In this case, Darken's model provides an excellent prediction. Therefore, this proposed method is expected to be a useful and powerful tool for studying Kirkendall-effect-induced deformation at this limit.

CHAPTER VI

DIFFUSE INTERFACE APPROACH FOR RIGOROUS MODELING

6.1 Introduction

When the typical average distance between vacancy sources and sinks is comparable to the size of the diffusion zone, the assumption of constant vacancy concentration is no longer valid, and diffusion of vacancies as one of the diffusing species must be considered explicitly. In Chapter III, we presented simulation results based on the rigorous model with quasi-one-dimensional geometries, accounting for vacancy diffusion. The motion of free surfaces and grain boundaries was observed, resulting from local volume changes in the immediate vicinity of free surfaces and grain boundaries that act as explicit vacancy sources and sinks. These results provided a glimpse into the different dynamics and equilibrium states that may result from vacancy diffusion when the vacancy concentration is not in equilibrium. However, these simulations were performed for one-dimensional systems to avoid the challenges associated with tracking multi-dimensional deformation of a diffusion couple. In this chapter, we will extend the rigorous model to a multi-dimensional system. To this end, we will extend the smooth boundary method to include a capability of imposing Dirichlet boundary conditions (i.e., specifying the boundary value of the field variable rather than its gradient) at diffuse interfaces. This new method enables us to specify the vacancy concentration at the boundaries that act as vacancy sources and sinks, as dictated in the rigorous model of interdiffusion, and to solve for the concentration evolution

within a solid that changes its shape as interdiffusion proceeds.

As in Chapter V, a phase field approach that distinguishes solid phase from vapor phase with a continuous order parameter will be employed in this work. For simplicity, only deformation of a single crystal solid will be considered. On a free surface, vacancy injection and annihilation change the surface shape by lattice reconstruction, which will not result in dilatational strains or internal stresses within the solid body. Therefore, we will not incorporate the plastic deformation model into this work.

6.2 Model

6.2.1 Smooth Boundary Method for Dirichlet Boundary Conditions

Let us first consider Fick's Second Law of diffusion in a solid object: $\partial C/\partial t = \nabla \cdot D\nabla C$, where C is the concentration and D is the diffusion coefficient. A phase-field-type order parameter distinguishes the solid domain from its environment, such that $\psi = 1$ denotes the solid phase and $\psi = 0$ denotes the vapor phase. To solve for the concentration evolution in the region where $\psi = 1$, we multiply the diffusion equation with the square of the order parameter profile:

$$\psi^2 \frac{\partial C}{\partial t} = \psi\psi\nabla \cdot D\nabla C = \psi\nabla \cdot (\psi D\nabla C) - \psi\nabla\psi \cdot D\nabla C. \tag{6.1}$$

Here, we can use the identity $\psi\nabla\psi \cdot D\nabla C = \nabla\psi \cdot D\nabla(\psi C) - DC\nabla\psi \cdot \nabla\psi$ to obtain

$$\psi^2 \frac{\partial C}{\partial t} = \psi\nabla \cdot (\psi D\nabla C) - \nabla\psi \cdot D\nabla(\psi C) + DC|\nabla\psi|^2. \tag{6.2}$$

To impose the boundary condition, the boundary value B_v is substituted for C in the third term on the right-hand side of Eq. (6.2); thus, we solve the following equation for the case:

$$\frac{\partial C}{\partial t} = \frac{1}{\psi}\nabla \cdot (\psi D\nabla C) - \frac{1}{\psi^2}\nabla\psi \cdot D\nabla(\psi C) + \frac{|\nabla\psi|^2}{\psi^2} DB_v. \tag{6.3}$$

To prove the convergence of the solution at the boundaries to the specified boundary value, we start with a one-dimensional version of the smooth boundary formulation. Integrating Eq. (6.2) over the interface region and reorganizing the equation give

$$\int_{a_i-\xi/2}^{a_i+\xi/2}\left[\psi^2\frac{\partial C}{\partial t}-\psi\frac{\partial}{\partial x}\left(\psi D\frac{\partial C}{\partial x}\right)\right]dx=\int_{a_i-\xi/2}^{a_i+\xi/2}\frac{\partial\psi}{\partial x}\cdot\left[D\frac{\partial\psi C}{\partial x}-DB_v\frac{\partial\psi}{\partial x}\right]dx, \quad (6.4)$$

where a_i is the location of the interface and ξ is the interface thickness. Similar to the derivation of Eq. (5.44), the left-hand side of Eq. (6.4) is proportional to the interface thickness, and it approaches zero in the limit of $\xi \to 0$. On the right-hand side of Eq. (6.4), the gradient of ψ approaches the Dirac delta function, $\delta(x-a_i)$, as the interface thickness approaches zero. Therefore, we can reformulate Eq. (6.4) to

$$0=D\frac{\partial\psi C}{\partial x}-DB_v\frac{\partial\psi}{\partial x}\Longrightarrow\frac{\partial\psi C}{\partial x}=B_v\frac{\partial\psi}{\partial x} \quad (6.5)$$

in the limit $\xi \to 0$. By taking integration over the interface region of Eq. (6.5) again, we obtain

$$1\cdot C|_{a_i+\xi/2}-0\cdot C|_{a_i-\xi/2}=\int_{a_i-\xi/2}^{a_i+\xi/2}B_v\frac{\partial\psi}{\partial x}dx, \quad (6.6)$$

which, in the limit $\xi \to 0$, recovers the specified Dirichlet boundary condition: $C|_{a_i} = B_v|_{a_i}$. Note that the boundary value B_v does not required to be a constant value. It can vary spatially or temporally or be a function of C. Therefore, the smooth boundary method is applicable to generalized boundary conditions. In addition, by incorporating the method described in Chapter V, one can impose Neumann boundary conditions simultaneously to yield mixed (or Robin) boundary conditions. The equation then becomes

$$\frac{\partial C}{\partial t}=\frac{1}{\psi}\nabla\cdot(\psi D\nabla C)-\frac{1}{\psi^2}\nabla\psi\cdot D\nabla(\psi C)+\frac{|\nabla\psi|^2}{\psi^2}DB_v-|\nabla\psi|B_f. \quad (6.7)$$

6.2.2 Smooth Boundary Method Applied to the Rigorous Model

The starting point is the formulation for diffusion in a single crystal solid in which no internal lattice site creation or destruction that result in plastic deformation. Thus, no advection is considered below. In a prefect lattice region of a binary substitutional alloy, diffusion of vacancies is governed by the standard Fick's Second Law, which, in a nondimensional form, reads

$$\frac{\partial X_V}{\partial t} = -\nabla \cdot J_V = \nabla \cdot (D_{VV}\nabla X_V + D_{VB}\nabla X_B), \tag{6.8}$$

where all quantities are dimensionless and were defined in previous chapters. By applying the smooth boundary method given in Eq. (6.3) to Eq. (6.8), we obtain

$$\begin{aligned}\frac{\partial X_V}{\partial t} =& \frac{1}{\psi}\nabla \cdot \psi(D_{VV}\nabla X_V + D_{VB}\nabla X_B) - \frac{1}{\psi^2}[\nabla\psi \cdot D_{VV}\nabla(\psi X_V) - |\nabla\psi|^2 D_{VV} X_V^{eq}] \\ =& \frac{1}{\psi}\nabla \cdot \psi(D_{VV}\nabla X_V + D_{VB}\nabla X_B) - K,\end{aligned} \tag{6.9}$$

where $K = [\nabla\psi \cdot D_{VV}\nabla(\psi X_V) - |\nabla\psi|^2 D_{VV} X_V^{eq}]/\psi^2$, and X_V^{eq} is the equilibrium vacancy concentration that serves as the boundary condition at the solid-vapor interfaces. Within the solid phase, ψ uniformly equals one, and $\nabla\psi$ equals zero. Therefore, Eq. (6.9) reduces back to Eq. (6.8) within the solid phase. Note that the terms absorbed in K are only important at the boundaries, while the first two terms in Eq. (6.9) act within the bulk. Therefore, the terms in K specify the boundary condition $X_V = X_V^{eq}$. K is thus related to the vacancy generation rate at the boundary appearing in the corresponding equation for the rigorous model, Eq. (2.29).

To derive the governing equation for the B concentration in the smooth boundary formulation, we note that the vacancy generation rate appears in both Eq. (2.29) and Eq. (2.30). By comparing these equations and the equation above, we conclude that the vacancy generation rate g is equivalent to $K/(1-X_V)$. Substituting this into the

smoothed boundary formulation, we obtain

$$\frac{\partial X_B}{\partial t} = \frac{1}{\psi}\nabla \cdot \psi(D_{BV}\nabla X_V + D_{BB}^V \nabla X_B) + \frac{X_B}{1 - X_V^{eq}} K. \tag{6.10}$$

Equations (6.9) and (6.10) serve as the governing equations describing interdiffusion in the solid phase where only surfaces act as vacancy sources and sinks.

According to Eq. (2.37), the magnitude of the normal velocity of a solid surface is determined by $v_n = \mathbf{n} \cdot J_V/(1 - X_V^{eq})$, where $\mathbf{n}$ is the unit normal vector of the solid surface. In a phase-field-type diffuse interface model, $\mathbf{n} = \nabla\psi/|\nabla\psi|$ gives the unit normal vector of the interface. The interface positions are indirectly evolved by changing the order parameter values. Therefore, the quantity $\mathbf{n} \cdot J_V/(1 - X_V^{eq})$ serves as a source of the order parameter so that the Cahn-Hilliard equation becomes

$$\frac{\partial \psi}{\partial t} = L_M \nabla^2 \mu_\psi + \frac{\nabla\psi}{|\nabla\psi|} \cdot \frac{J_V}{1 - X_V^{eq}}. \tag{6.11}$$

Note that the source term is only nonzero at solid-vapor interfaces and is uniformly zero in the bulk phases. The source term relates the jump of vacancy flux across the solid-vapor interface to the volume change, as discussed in Section 2.3. Therefore, the evolution of the order parameter field is coupled with the concentration evolution through the source term. This is similar to the "latent heat" terms for solidification that couples the order parameter and the temperature fields.

6.3 Results

We provide examples of simulations to demonstrate the smooth boundary formulation of the rigorous model in a single crystal diffusion couple in a two-dimensional domain. The first example is a cylindrical diffusion couple with a void located at the center of the cylinder. A cylindrical diffusion couple with an outer radius of 0.64 μm and a void radius of 0.05 μm is placed in a 1.92 μm $\times$ 1.92 μm computational box as shown in Figs. 6.1(a), 6.1(b) and 6.3(a). The void is concentric with the cylinder. The fast

diffuser initially occupies the central region with a radius smaller than 0.46 μm. All physical parameters are similar to those in Chapter V. The governing equation for the vacancy concentration, Eq. (6.9), is constrained by a very small time step because of the large diffusivity, D_{VV}. Thus, we use a semi-implicit time scheme to solve the equation and significantly enhance numerical efficiency. In the time-discretized form, the scheme is given by

$$\frac{X_V^{(n+1)} - X_V^{(n)}}{\Delta t} - \frac{\chi \bar{D}_{VV}^{(n)}}{\psi^{(n)}} \nabla \cdot \psi^{(n)} \nabla X_V^{(n+1)} = \frac{1}{\psi^{(n)}} \nabla \cdot \psi^{(n)} [(D_{VV}^{(n)} - \chi \bar{D}_{VV}^{(n)}) \nabla X_V^{(n)} + D_{BB}^{V(n)} \nabla X_B^{(n)}] - K^{(n)}, \tag{6.12}$$

where the superscript n denotes the n-th time step and χ is a weight factor that can be optimized to increase numerical stability. The diffusion equation for B atoms [Eq. (6.10)] and the Cahn-Hilliard equation [Eq. (6.11)] are solved using the explicit Euler time scheme.

Figure 6.1 shows snapshots of the dimensionless B concentration ($\tilde{C}_B = C_B/\rho = X_B$) and dimensionless scaled vacancy concentration ($\tilde{C}_V = C_V/(\rho X_V^{eq}) = X_V/X_V^{eq}$). During diffusion, B atoms diffuse outward mainly by exchange with vacancies, thus reducing vacancy concentration in the A-rich region and enhancing vacancy concentration in the B-rich region. In order to maintain equilibrium vacancy concentration at the solid surface, vacancies are injected at the outer solid surface and are eliminated at the void surface. As can be seen in the figure, the smooth boundary method regulates the vacancy concentration at its equilibrium value at both the outer surface and the void surface. When vacancies are injected into the solid, the source term of the order parameter induces the outer surface to move outward by increasing the order parameter value at the solid-vapor interface. On the other hand, the source term induces the void surface to move into the solid by reducing the order parameter value at the void surface where vacancies are annihilated. As both the void radius and the outer radius increase, the cylinder with an initially small hole transforms

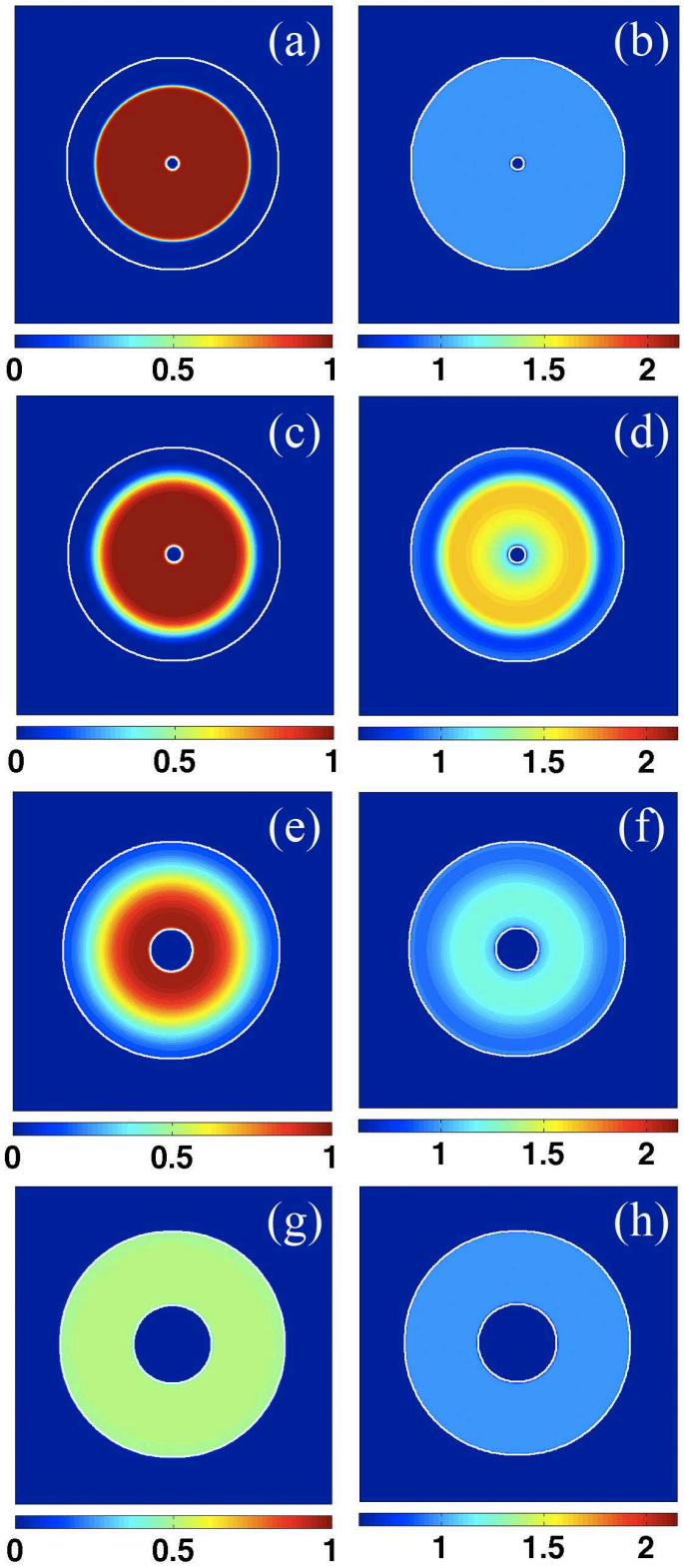

Figure 6.1: Snapshots of the dimensionless concentration of B atoms ($\tilde{C}_B = C_B/\rho$) (in the left column), and the dimensionless scaled concentration of vacancies ($\tilde{C}_V = C_V/(\rho X_V^{eq})$) (in the right column) taken at $t = 0$, $t = 2.88 \times 10^2$, $t = 2.57 \times 10^3$ and $t = 3.28 \times 10^4$ sec (from the top row to the bottom row). The white lines indicate the solid-vapor interfaces.

into a tube with a homogeneous-concentration solid region surrounding a larger hole. This resulting growth dynamics is consistent with the prediction in Chapter III, although quantitatively matching the results will require precise parameterization of the Cahn-Hilliard equation employed in the simulation.

To gain further insight into the dynamics of hollow cylinder formation, we perform a simulation in which the initial void is not located at the center of the cylinder. This case cannot be simulated with the simplified one-dimensional cylindrical symmetry that was used in Chapter III. The cylinder radius and the initial void radius are taken to be 0.64 μm and 0.05 μm, respectively, as in the previous case. The center of the void is offset from the center of the cylinder by 0.38 μm, as shown in Figs. 6.2(a) and 6.3(a). The result is shown in Fig. 6.2. The diffusion process behaves similarly to the concentric case. The fast diffuser diffuses outward by exchanging with vacancies. Vacancy injection at the outer surface and vacancy elimination at the void surface lead to the tube formation. Therefore, the outer surface and void surface are the vacancy source and sink, respectively.

The final void radius and the final cylinder radius are both slightly smaller than those in the concentric case, see Fig. 6.3(b). Since the distance between the outer surface and the void surface in the bottom region of the cylinder is smaller than that in the concentric case, the diffusion process terminates quicker at that location. After the concentration reaches equilibrium in the bottom region, diffusion only occurs in the top region, where the average vacancy source-sink distance is larger. As a result, in comparison to the concentric case, the fast mode of interdiffusion decreases, and the slow mode becomes more important overall. Since slow mode diffusion homogenizes the atomic concentrations without causing a net vacancy flux while fast-mode diffusion results in net mass transport via a nonzero net vacancy flux, the final void size is reduced compared to the concentric void case. In addition, since diffusion terminates in the bottom region earlier, the Gibbs-Thomson effect may also contribute

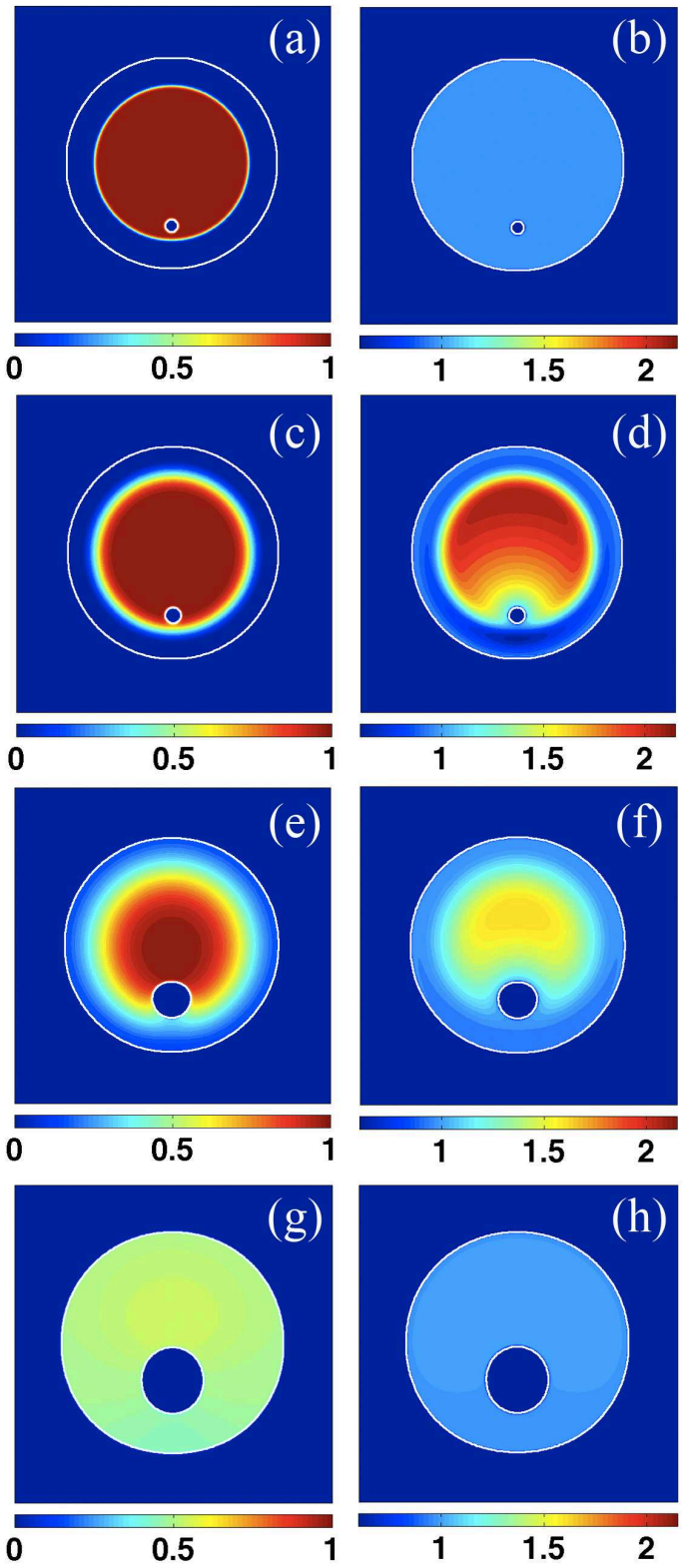

Figure 6.2: Snapshots of the dimensionless concentration of B atoms ($\tilde{C}_B = C_B/\rho$) (in the left column), and the dimensionless scaled concentration of vacancies ($\tilde{C}_V = C_V/(\rho X_V^{eq})$) (in the right column) taken at $t = 0$, $t = 2.79 \times 10^2$, $t = 2.62 \times 10^3$ and $t = 3.74 \times 10^4$ sec (from the top row to the bottom row). The white lines indicate the solid-vapor interfaces.

to void radius reduction. Nevertheless, the dynamics of tube formation is qualitatively unchanged by the location of the initial void, supporting the validity of the quasi-one-dimensional results presented in Chapter III.

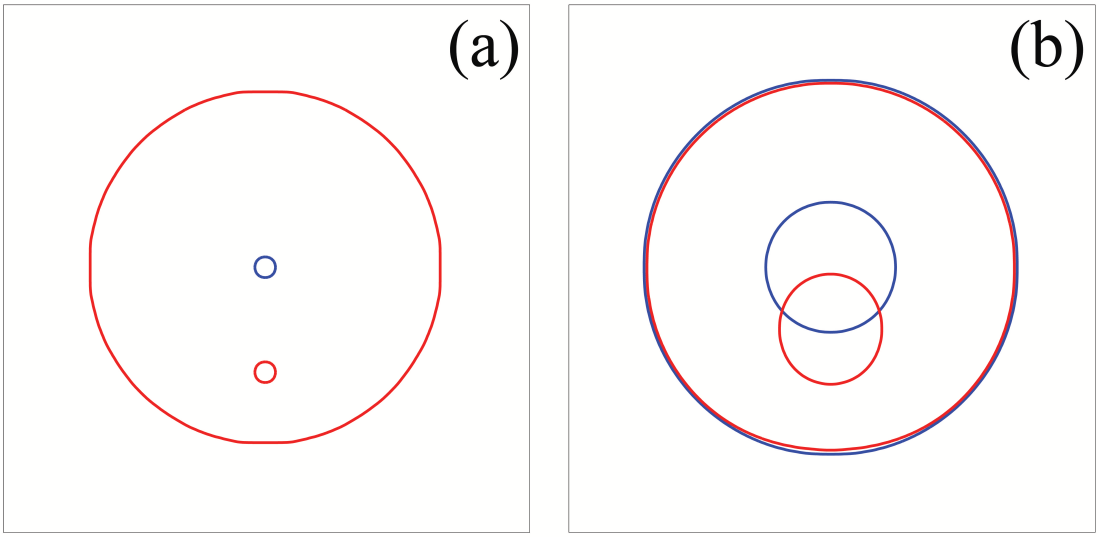

Figure 6.3: (a) The initial contour of cylinders: the blue lines for the concentric case and the red lines for the non-concentric case. The two outer radii of the concentric and non-concentric cases overlap. (b) The final contour of the tubes in the two cases

6.4 Conclusion

In this chapter, we proposed a new smooth boundary method that can properly impose the Dirichlet boundary condition at the diffuse interface. Along with the smooth boundary method for the Neumann boundary condition presented in Chapter V, the new numerical technique is expected to become widely employed as a flexible and powerful tool for solving various differential equations within static or dynamic complex geometries. We applied this method to hollow cylinder formation via the Kirkendall effect, and observed the effect of the distance between the source and the sink on formation dynamics. These results supported the validity of the quasi-one-dimensional simulations presented in Chapter III.

CHAPTER VII

SUMMARY, CONCLUSIONS, AND FUTURE WORK

In this dissertation, we proposed a new, more rigorous model of the Kirkendall effect. We considered explicit and localized sources and sinks of vacancies, where vacancies can be supplied or eliminated. We assumed that free surfaces and grain boundaries are more efficient vacancy sources and sinks than dislocations are, and therefore the role of dislocations as a vacancy source or sink within the bulk of a grain was ignored. This assumption is different from the current standard model based on Darken's analysis, where vacancy sources and sinks are assumed to exist everywhere within a solid. As with Darken's model, we assumed that sources and sinks act ideally; i.e., any supersaturation or depletion is immediately accommodated at these locations. At the macro scale, in which the typical vacancy-source-sink distance is negligible compared to the characteristic length of the diffusion zone, the rigorous model recovers the conventional model (i.e., Darken's model).

A set of rigorous diffusion equations for both the atomic diffusing species and vacancies was derived using the flux expressions for a substitutional binary alloy with explicit consideration of vacancy diffusion. These diffusion equations include a vacancy generation rate that maintains the vacancy concentration at vacancy sources and sinks at the equilibrium value, which results in local volume expansion or shrinkage. This model was first applied to one-dimensional planar systems and quasi-one-dimensional cylindrical geometries. The former showed a Kirkendall shift that is qualitatively and

quantitatively different from the predictions of Darken's model. The latter was used to simulate tube formation dynamics and to estimate the fully-grown tube sizes and elapsed time under different initial conditions. Motion of surfaces and grain boundaries was observed when vacancies were injected or eliminated at these locations in both of these cases. These results demonstrated that explicit consideration of vacancy diffusion leads to different dynamics and final states (after the concentrations achieve equilibrium or near equilibrium) compared with what Darken's model would predict.

Two-dimensional simulations of the concentration evolution in a solid containing a grain boundary demonstrated that the interdiffusion process changes from fast-mode diffusion to slow-mode diffusion as the region, where interdiffusion occurs, becomes farther away from a grain boundary. Without a sufficient density of sources and sinks, vacancy concentration deviates from its equilibrium value. The resulting concentration gradient suppresses further rapid vacancy diffusion; thus, interdiffusion proceeds by slow-mode diffusion. Conversely, near a grain boundary, fast-mode diffusion dominates because vacancy supply and elimination are efficient.

We also extended the smooth boundary method to impose generalized boundary conditions, namely Neumann, Dirichlet, and mixed types, at internal boundaries of arbitrary shapes. This numerical approach was applied to the traditional interdiffusion model coupled with a linear visco-plastic deformation model that governs the Kirkendall-effect-induced deformation. Expansion and contraction of a simple diffusion couple occurred due to vacancy generation and elimination taking place throughout the volume. For a sheet-like diffusion couple, significant bending was also observed. In a diffusion couple resembling a lap joint, we observed a complex combination of deformations. Furthermore, using the smooth boundary method to impose the equilibrium vacancy concentration at the solid surface (a Dirichlet boundary condition), tube formation based on our rigorous model, similar to that examined using a quasi-one-dimensional sharp interface model mentioned earlier, was simulated; the

results were consistent with the quasi-one-dimensional results. The two-dimensional effect was examined by displacing the initial void toward the diffusion front. The results remained qualitatively similar, and thus this formed the basis for the validity of the quasi-one-dimensional model of tube formation. We also performed a simple analysis to show that the consideration of vacancy diffusion between sources and sinks is important at the micron or nanometer scale in alloys.

Our model that includes plastic deformation is capable of solving the interdiffusion process accompanied by resultant deformation of the solid. We expect that this new smooth boundary method will become widely adapted as a flexible numerical method for solving various differential equations. Currently, the coupled diffusion/visco-plastic-deformation model based on the smooth boundary method is being extended so that polycrystalline materials can be simulated. This model involves implementation of Dirichlet boundary conditions associated with the equilibrium vacancy concentration at the grain boundaries (as well as on surfaces if applicable) and a modification to include diffusion flux across and along the grain boundaries. An example of the preliminary results is shown in Fig. 7.1. Bulge formation near the intersection between surfaces and grain boundaries was observed on the surface near a grain boundary, which is consistent with experimental results [43, 147], an example of which is shown in Fig. 7.2. This polycrystalline model possesses the potential to theoretically explain the whisker growth phenomenon that plagues lead-free solder joints. In addition, we plan to develop an adaptive grid system that allows us to use finer grid spacing at diffuse interfaces while keeping coarser grid spacing in the bulk regions to enhance the accuracy and the efficiency of the proposed smooth boundary method.

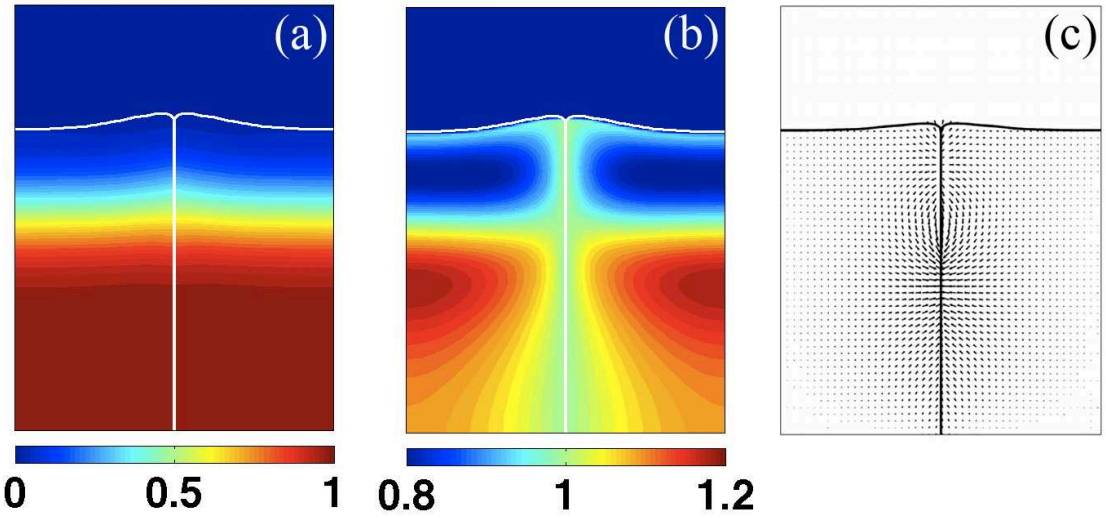

Figure 7.1: (a) The dimensionless concentration of B atoms ($\tilde{C}_B = C_B/\rho$), and (b) the dimensionless scaled concentration of vacancies ($\tilde{C}_V = C_V/(\rho X_V^{eq})$) near an intersection between a surface and a grain boundary. (c) The plastic flow velocity induced by the lattice generation at the grain boundary.

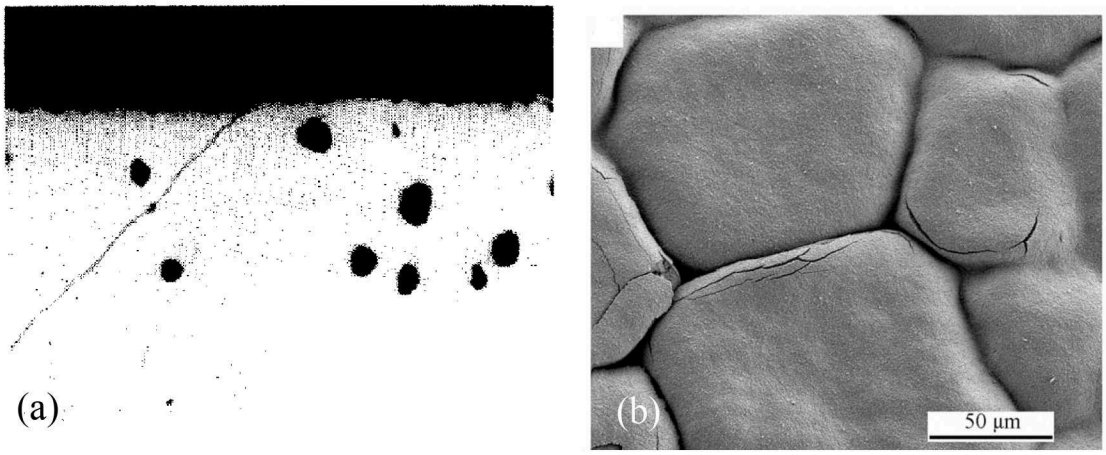

Figure 7.2: (a) The step forming (due to Kirkendall effect) at the intersection between a surface and a grain boundary, from Ref. [43]. (b) The surface rumpling near grain boundaries, from Ref. [147].

APPENDICES

APPENDIX A

AN ALTERNATIVE DERIVATION OF EQS (2.29) AND (2.30)

In a Cartesian coordinate system, the center of mass of an infinitesimal cubic-shaped control volumes is located at $\mathbf{x}(x, y, z)$, and the control volume has dimensions Δx, Δy and Δz. The size of a control volume can vary in time. Inside the control volume, the concentrations of diffusers are assumed to be uniformly distributed. If a control volume contains a vacancy source or sink, such as a grain boundary, it will have a nonzero vacancy generation rate, $g(\mathbf{x}, t)$ per unit volume per unit time. The vacancy concentration within the control volume containing vacancy sources at time $t + \Delta t$ is described by

$$C_V(t + \Delta t) = \frac{N_V(t + \Delta t)}{U(t + \Delta t)} = \frac{N_V + \Delta N_V}{U + \Delta U}, \tag{A.1}$$

where N_V is the number of vacancies within the control volume and $U = \Delta x \Delta y \Delta z$ is the size of the control volume. Here, ΔN_V and ΔU are the change in N_V and U over a small time step Δt. For given J_V^x, J_V^y and J_V^z on the boundaries of the control volume, Eq. (A.1) can be written as

$$\begin{aligned} C_V(t + \Delta t) = & \frac{1}{U + \Delta U} \Big\{ U C_V(t) + \Big[\left(J_V^x|_{x - \frac{\Delta x}{2}} - J_V^x|_{x + \frac{\Delta x}{2}} \right) \Delta y \Delta z \\ & + \left(J_V^y|_{y - \frac{\Delta y}{2}} - J_V^y|_{y + \frac{\Delta y}{2}} \right) \Delta z \Delta x \\ & + \left(J_V^z|_{z - \frac{\Delta z}{2}} - J_V^z|_{z + \frac{\Delta z}{2}} \right) \Delta x \Delta y + U g \Big] \Delta t \Big\}. \end{aligned} \tag{A.2}$$

The volume change of the control volume in a time step Δt is expressed by

$$\Delta U = \frac{U}{\rho}\left(-\nabla \cdot J_V + g - \nabla \cdot J_B - \nabla \cdot J_B\right)\Delta t, \tag{A.3}$$

where ρ is the lattice site density.

By substituting Eq. (A.3) to Eq. (A.2) and taking limit of $\Delta x \to 0$, $\Delta y \to 0$, $\Delta z \to 0$ and $\Delta t \to 0$, we can derive

$$\frac{\partial C_V}{\partial t} = -\nabla \cdot J_V + g\left(1 - \frac{C_V}{\rho}\right) + \frac{C_V}{\rho}\nabla \cdot \left(J_V + J_A + J_B\right). \tag{A.4}$$

By following the same procedure as in derivation of Eq. (A.4), the concentration change rate of B atoms is obtained as

$$\frac{\partial C_B}{\partial t} = -\nabla \cdot J_B - g\frac{C_B}{\rho} + \frac{C_B}{\rho}\nabla \cdot \left(J_V + J_A + J_B\right). \tag{A.5}$$

Due to conservation of lattice site, the divergence of total fluxes across the control volume faces vanishes, $\nabla \cdot (J_V + J_A + J_B) = 0$, in Eqs. (A.4) and (A.5).

BIBLIOGRAPHY

[1] E. Kirkendall, L. Thomassen, and C. Uethegrove, Transactions of the American Institute of Mining and Metallurgical Engineers **133**, 186 (1939).

[2] H. Nakajima, JOM-Journal of the Minerals Metals and Materials Society **49**, 15 (1997).

[3] E. O. Kirkendall, Transactions of the American Institute of Mining and Metallurgical Engineers **147**, 104 (1942).

[4] A. D. Smigelskas and E. O. Kirkendall, Transactions of the American Institute of Mining and Metallurgical Engineers **171**, 130 (1947).

[5] L. C. C. da Silva, JOM-Journal of the Minerals Metals and Materials Society **50**, 6 (1998).

[6] H. B. Huntington and F. Seitz, Physical Review **61**, 315 (1942).

[7] L. S. Darken, Transactions of the American Institute of Mining and Metallurgical Engineers **175**, 184 (1948).

[8] *Atom Movements* (American Society for Metals, Cleveland, Ohio, 1951).

[9] L. C. C. da Silva and R. F. Mehl, Transactions of the American Institute of Mining and Metallurgical Engineers **191**, 155 (1951).

[10] L. N. Paritskaya, Defect and Diffusion Forum **249**, 73 (2006).

[11] H. C. Bhedwar, V. Balasubr, S. D. Kulkarni, and K. K. Ray, Scripta Metallurgica **6**, 919 (1972).

[12] H. Oikawa and A. Hosoi, Scripta Metallurgica **9**, 823 (1975).

[13] A. Bolk, Acta Metallurgica **6**, 59 (1958).

[14] A. Bolk, Acta Metallurgica **9**, 632 (1961).

[15] A. Bolk, Acta Metallurgica **9**, 643 (1961).

[16] R. O. Meyer and L. M. Slifkin, Physical Review **149**, 556 (1966).

[17] R. O. Meyer, Physical Review **181**, 1086 (1969).

[18] D. H. Killpatrick and R. W. Balluffi, Journal of Applied Physics **30**, 449 (1959).

[19] H. W. Paxton and E. J. Pasierb, Transactions of the American Institute of Mining and Metallurgical Engineers **218**, 794 (1960).

[20] M. M. P. Janssen and G. D. Rieck, Transactions of the Metallurgical Society of AIME **239**, 1372 (1967).

[21] A. Kohn, J. Levasseur, J. Philibert, and M. Wanin, Acta Metallurgica **18**, 163 (1970).

[22] H. Kahkonen and E. Syrjanen, Journal of Materials Science **5**, 710 (1970).

[23] M. Weinhagen, B. Kohler, J. Wolff, and T. Hehenkamp, Defect and Diffusion Forum **143**, 449 (1997).

[24] D. Ansel, I. Thibon, M. Boliveau, and J. Debuigne, Acta Materialia **46**, 423 (1998).

[25] M. J. H. van Dal, M. C. L. P. Pleumeekers, A. A. Kodentsov, and F. J. J. van Loo, Journal of Alloys and Compounds **309**, 132 (2000).

[26] C. H. Yu, K. S. Kim, and J. M. Yang, Materials Transactions **44**, 2163 (2003).

[27] K. J. Zeng, R. Stierman, T. C. Chiu, D. Edwards, K. Ano, and K. N. Tu, Journal of Applied Physics **97**, 024508 (2005).

[28] Z. Q. Mei, M. Ahmad, M. Hu, and G. Ramakrishna, 55th Electronic Components and Technology Conference, Vols 1 and 2, 2005 Proceedings , 415 (2005).

[29] K. Okumura, Journal of the Electrochemical Society **128**, 571 (1981).

[30] E. Zakel and H. Reichl, IEEE Transactions on Components Hybrids and Manufacturing Technology **16**, 323 (1993).

[31] S. Murali, N. Srikanth, and C. J. Vath, Materials Letters **58**, 3096 (2004).

[32] I. D. Choi, D. K. Matlock, and D. L. Olson, Materials Science and Engineering A-Structural Materials Properties Microstructure and Processing **124**, L15 (1990).

[33] S. H. Wang, D. K. Matlock, and D. L. Olson, Materials Science and Engineering A-Structural Materials Properties Microstructure and Processing **167**, 139 (1993).

[34] L. G. Feinstein and J. B. Bindell, Thin Solid Films **62**, 37 (1979).

[35] S. Nakahara and R. J. McCoy, Thin Solid Films **72**, 457 (1980).

[36] S. Nakahara and R. J. McCoy, Applied Physics Letters **37**, 42 (1980).

[37] S. Pramanick, Y. N. Erokhin, B. K. Patnaik, and G. A. Rozgonyi, Applied Physics Letters **63**, 1933 (1993).

[38] D. L. Anton and A. F. Giamei, Materials Science and Engineering **76**, 173 (1985).

[39] J. A. Nesbitt and R. W. Heckel, Metallurgical Transactions A-Physical Metallurgy and Materials Science **18**, 2061 (1987).

[40] N. Matan, H. M. A. Winand, P. Carter, M. Karunaratne, P. D. Bogdanoff, and R. C. Reed, Acta Materialia **46**, 4587 (1998).

[41] R. W. Balluffi and B. H. Alexander, Journal of Applied Physics **23**, 1237 (1952).

[42] R. W. Balluffi, Acta Metallurgica **2**, 194 (1954).

[43] R. W. Balluffi and L. L. Seigle, Acta Metallurgica **3**, 170 (1955).

[44] R. S. Barnes and D. J. Mazey, Acta Metallurgica **6**, 1 (1958).

[45] I. Daruka, I. A. Szabo, D. L. Beke, C. S. Cserhati, A. Kodentsov, F. J. J. van Loo, Acta Materialia **44**, 4981 (1996).

[46] G. Opposits, S. Szabo, D. L. Beke, Z. Guba, and I. A. Szabo, Scripta Materialia **39**, 977 (1998).

[47] R. Voigt and V. Ruth, Journal of Physics-Condensed Matter **7**, 2655 (1995).

[48] O. Kahlen, A. Kern, and V. Ruth, Defect and Diffusion Forum **143**, 489 (1997).

[49] D. L. Beke and I. A. Szabo, Defect and Diffusion Forum **95-98**, 537 (1993).

[50] D. L. Beke, I. A. Szabo, Z. Erdelyi, and G. Opposits, Materials Science and Engineering A-Structural Materials Properties Microstructure and Processing **387**, 4 (2004).

[51] P. R. Okamoto and H. Wiedersi, Journal of Nuclear Materials **53**, 336 (1974).

[52] A. D. Marwick, Journal of Physics F-Metal Physics **8**, 1849 (1978).

[53] S. Watanabe, H. Kinoshita, N. Sakaguchi, and H. Takahashi, Journal of Nuclear Materials **226**, 330 (1995).

[54] R. G. Faulkner, S. H. Song, P. E. J. Flewitt, M. Victoria, and P. Marmy, Journal of Nuclear Materials **255**, 189 (1998).

[55] V. A. Pechenkin, G. A. Epov, I. A. Stepanov, and Y. V. Konobeev, Effects of Radiation on Materials: 18th International Symposium **1325**, 850 (1999).

[56] J. Bardeen, Physical Review **76**, 1403 (1949).

[57] F. Seitz, Acta Metallurgica **1**, 355 (1953).

[58] H. Fara and R. W. Balluffi, Journal of Applied Physics **30**, 325 (1959).

[59] L. Peichl and D. F. Bettridge, Overlay and diffusion coatings, in *Materials for Advanced Power Engineering 1994 (Part 1)*, edited by D. Coutsouradis, J. H. Davidson, J. Ewald, P. Greenfield, T. Khan, M. Malik, D. B. Meadowcroft, V. Regis, R. B. Scarlin, F. Schubert, and D. V. Thornton, pp. 717 – 740, Springer, 1994

[60] J. Angenete and K. Stiller, Oxidation of Metals **60**, 83 (2003).

[61] H. J. Fan, M. Knez, R. Scholz, K. Nielsch, E. Pippel, D. Hesse, M. Zacharias, and U. Gosele, Nature Materials **5** (2006).

[62] H. J. Fan, U. Gosele, and M. Zacharias, Small **3**, 1660 (2007).

[63] B. Liu and H. C. Zeng, Journal of the American Chemical Society **126**, 16744 (2004).

[64] Y. D. Yin, R. M. Rioux, C. K. Erdonmez, S. Hughes, G. A. Somorjai, and A. P. Alivisatos, Science **304**, 711 (2004).

[65] Y. D. Yin, C. K. Erdonmez, A. Cabot, S. Hughes, and A. P. Alivisatos, Advanced Functional Materials **16**, 1389 (2006).

[66] N. H. Chou and R. E. Schaak, Chemistry of Materials **20**, 2081 (2008).

[67] J. B. Fei, Y. Cui, X. H. Yan, W. Qi, Y. Yang, K. W. Wang, Q. He, and J. B. Li, Advanced Materials **20**, 452 (2008).

[68] Q. Li and R. M. Penner, Nano Letters **5**, 1720 (2005).

[69] H. Arami, M. Mazloumi, R. Khalifehzadeh, and S. K. Sadrnezhaad, Advances in Applied Ceramics Advances in Applied Ceramics **108**, 73 (2009).

[70] K. N. Tu and U. Gosele, Applied Physics Letters **86**, 093111 (2005).

[71] A. M. Gusak, T. V. Zaporozhets, K. N. Tu, and U. Gosele, Philosophical Magazine **85**, 4445 (2005).

[72] F. Aldinger, Acta Metallurgica **22**, 923 (1974).

[73] L. N. Paritskaya and Y. E. Geguzin, Physics of Metals and Metallography **40**, 311 (1974).

[74] L. N. Paritskaya and Y. E. Geguzin, Physics of Metals and Metallography **41**, 656 (1976).

[75] Y. Kaganovskii, L. N. Paritskaya, and V. V. Bogdanov, Defect and Diffusion Forum **277**, 9 (2008).

[76] J. C. W. Hwang, J. D. Pan, and R. W. Balluffi, Journal of Applied Physics **50**, 1349 (1978).

[77] L. N. Paritskaya, V. V. Bogdanov, Y. Kaganovskii, and W. Gust, Interface science **10**, 297 (2002).

[78] G. T. Galyon and L. Palmer, IEEE Transactions on Electronics Packaging Manufacturing **28**, 17 (2005).

[79] W. J. Boettinger, G. B. McFadden, S. R. Coriell, and J. A. Warren, Acta Materialia **53**, 1995 (2005).

[80] W. J. Boettinger, J. E. Guyer, C. E. Campell, and G. B. McFadden, Proceedings of the Royal Society A **463**, 3347 (2007).

[81] J. A. Dantzig *et al.*, Metallurgical and Materials Transactions **37A**, 2701 (2006).

[82] H.-C. Yu, A. Van der Ven, and K. Thornton, Applied Physics Letters **93**, 091908 (2008).

[83] J. D. van der Waals (translated by J. S. Rowlinson), Journal of Statistical Physics **20**, 197 (1979).

[84] J. W. Cahn and J. E. Hilliard, Journal of Chemical Physics **28**, 250 (1958).

[85] V. L. Ginzburg and L. D. Landau, Soviet Physics JETP **20**, 1064 (1950).

[86] S. M. Allen and J. W. Cahn, Acta Metallurgica **27**, 1085 (1979).

[87] A. A. Wheeler, W. J. Boettinger, and G. B. McFadden, Physical Review A **45**, 7424 (1992).

[88] A. A. Wheeler, B. T. Murray, and R. J. Schaefer, Physica D **66**, 243 (1993).

[89] J. A. Warren and W. J. Boettinger, Acta Metallurgica et Materialia **43**, 689 (1995).

[90] M. E. Gurtin, D. Polignone, and J. Vinals, Mathematical Models and Methods in Applied Sciences **6**, 815 (1996).

[91] D. M. Anderson, G. B. McFadden, and A. A. Wheeler, Annual Review of Fluid Mechanics **30**, 139 (1998).

[92] A. Karma and W.-J. Rappel, Physical Review E **57**, 4323 (1998).

[93] A. Karma and W.-J. Rappel, Physical Review E **60**, 3614 (1999).

[94] J. W. Cahn, Journal of Chemical Physics **66**, 3667 (1977).

[95] L. Granasy, T. Pusztai, D. Saylor, and J. A. Warren, Physical Review Letters **98**, 035703 (2007).

[96] J. A. Warren, T. Pusztai, L. Kornyei, and L. Granasy, Physical Review B **79**, 014204 (2009).

[97] A. Bueno-Orovio and V. M. Perez-Garcia, Numerical Methods for Partial Differential Equations **22**, 435 (2006).

[98] A. Bueno-Orovio, V. M. Perez-Garcia, and F. H. Fenton, SIAM Journal on Scientific Computing **28**, 886 (2006).

[99] J. R. Manning, Physical Review B **4**, 1111 (1971).

[100] L. K. Moleko, A. R. Allnatt, and E. L. Allnatt, Philosophical Magazine A **59**, 141 (1989).

[101] A. Van der Ven and G. Ceder, Physical Review Letters **94**, 045901 (2005).

[102] F. Seitz, Physical Review **74**, 1513 (1948).

[103] S. R. deGroot and P. Mazur, *Non-equilibrium thermodynamics* (Dover, New York, 1984).

[104] L. Onsager, Physical Review **37**, 405 (1931).

[105] L. Onsager, Physical Review **38**, 2265 (1931).

[106] A. Van der Ven, H.-C. Yu, K. Thornton, and G. Ceder, Progress in Materials Science (in press).

[107] J. Bardeen and C. Herring, *Atom Movements* (American Society for Metals, Cleveland, Ohio, 1951), pp. 87–111.

[108] J. Svoboda, F. D. Fischer, P. Fratzl, and A. Kroupa, Acta Materialia **50**, 1369 (2002).

[109] J. Svoboda, F. D. Fischer, and P. Fratzl, Acta Materialia **54**, 3043 (2006).

[110] J. Svoboda, F. D. Fischer, and E. Gamsjager, Acta Materialia **56**, 351 (2008).

[111] H.-C. Yu, D.-H. Yeon, A. Van der Ven, and K. Thornton, Acta Materialia **55**, 6690 (2007).

[112] R. W. Balluffi, S. M. Allen, and W. C. Carter, *Kinetics of Materials* (Wiley-Interscience, Hoboken, New Jersey, 2005), chap. 7–8.

[113] G. H. Vineyard, Journal of Physics and Chemistry of Solids **3**, 121 (1957).

[114] A. R. Allnatt, Journal of Physics C-Solid State Physics **15**, 5605 (1982).

[115] I. V. Belova and G. E. Murch, Philosophical Magazine A **80**, 599 (2000).

[116] R. W. Balluffi and B. H. Alexander, Journal of Applied Physics **23**, 953 (1952).

[117] J. D. Whittenb, Metallurgical Transactions **3**, 3038 (1972).

[118] D. N. Seidman and R. W. Balluffi, Dislocations as sources and sinks for point defects in metals, in *Lattice Defects and Their Interactions*, edited by R. R. Hasiguti, pp. 913 – 960, Gordon and Breach Science Publishers, New York, 1967.

[119] J. S. Koehler and C. Lund, Nonequilibrium situations involving vacancies in gold, in *Lattice Defects in Quenched Metals*, edited by R. M. Cotterill, M. Doyama, J. J. Jackson, and M. Meshii, pp. 1–13, Academic Press, New York, 1965.

[120] P. E. Doherty and R. S. Davis, Acta Metallurgica **7**, 118 (1959).

[121] B. K. Basu and C. Elbaum, Acta Metallurgica **13**, 1117 (1965).

[122] H. Gleiter, Journal of the less-Common Metals **28**, 297 (1972).

[123] R. W. Siegel, S. M. Chang, and R. W. Balluffi, Acta Metallurgica **28**, 249 (1980).

[124] A. M. Gusak, S. V. Kornienko, and G. V. Lutsenko, Defect and Diffusion Forum **264**, 109 (2007).

[125] J. Svoboda, F. D. Fischer, and D. Vollath, Acta Materialia **57**, 1912 (2009).

[126] A. V. Evteev, E. V. Levchenko, I. V. Belova, and G. E. Murch, Philosophical Magazine **88**, 1525 (2008).

[127] I. Kaur, Y. Mishin, and W. Gust, *Fundamentals of Grain and Interphase Boundary Diffusion*, 3rd rev. and enl. ed. (John Wiley, New York, 1995), chap. 1, pp. 8–9.

[128] E. Rabkin, L. Klinger, T. Izyumova, and V. N. Semenov, Scripta Materialia **42**, 1031 (2000).

[129] J. W. Cahn, J. D. Pan, and R. W. Balluffi, Scripta Metallurgica **13**, 503 (1979).

[130] R. W. Balluffi and J. W. Cahn, Acta Metallurgica **29**, 493 (1981).

[131] D. B. Butrymowicz, D. E. Newbury, D. Turnbull, and J. W. Cahn, Scripta Metallurgica **18**, 1005 (1984).

[132] D. Liu, W. A. Miller, and K. T. Aust, Acta Metallurgica **37**, 3367 (1989).

[133] K. W. Kehr, K. Binder, and S. M. Reulein, Physical Review B **39**, 4891 (1989).

[134] I. V. Belova and G. E. Murch, Philosophical Magazine A **84**, 2139 (2004).

[135] E. Kramer, P. Green, and C. J. Palmstrom, Polymer **25**, 473 (1984).

[136] A. V. Nazarov and K. P. Gurov, Physics of Metals and Metallography **37**, 41 (1974).

[137] G. B. Stephenson, Acta Metallurgica **36**, 2663 (1988).

[138] J. Philibert, *Atom Movements: Diffusion and Mass transport in Solids* (Les Editions de Physique, Les Ulis, France, 1991), pp. 233–241.

[139] R. F. Sekerka, Progress in Materials Science **49**, 511 (2004).

[140] D. Kim and W. Lu, Journal of the Mechanics and Physics of Solids **54**, 2554 (2006).

[141] D. Jacqmin, Journal of Computational Physics **155**, 96 (1999).

[142] B. Zhou and A. Powell, Journal of Membrane Science **268**, 150 (2006).

[143] D. Kim and W. Lu, Computational Materials Science **38**, 418 (2006).

[144] W. Villanueva, K. Gronhagen, G. Amberg, and J. Agren, Physical Review E **77**, 056313 (2008).

[145] J. Kockelkoren, H. Levine, and W.-J. Rappel, Physical Review E **68**, 037702 (2003).

[146] H. Levine and W.-J. Rappel, Physical Review E **72**, 061912 (2005).

[147] V. K. Tolpygo and D. R. Clarke, Acta Materialia **52**, 5129 (2004).